



Fernando Puente León • Klaus Dostert (Editors)

Reports on Industrial Information Technology

Volume 12

Reports on Industrial Information Technology

Volume 12

Institute of Industrial Information Technology
Karlsruhe Institute of Technology

Fernando Puente León • Klaus Dostert (Editors)

Reports on Industrial Information Technology

Volume 12

Impressum

Karlsruher Institut für Technologie (KIT)
KIT Scientific Publishing
Straße am Forum 2
D-76131 Karlsruhe
www.uvka.de

KIT – Universität des Landes Baden-Württemberg und nationales
Forschungszentrum in der Helmholtz-Gemeinschaft



Diese Veröffentlichung ist im Internet unter folgender Creative Commons-Lizenz
publiziert: <http://creativecommons.org/licenses/by-nc-nd/3.0/de/>

KIT Scientific Publishing 2010
Print on Demand

ISSN 1610-9406
ISBN 978-3-86644-490-4

Contents

Preface	v
---------------	---

Signal processing

Comparison of ICA algorithms for underdetermined blind source separation	1
<i>A. Sandmair (Karlsruhe Institute of Technology),</i>	
<i>A. Zaib (Karlsruhe Institute of Technology)</i>	

Extension of Particle Swarm Optimization for detection of local minima	19
<i>A. Sandmair (Karlsruhe Institute of Technology),</i>	
<i>N. Linzenkirchner (Karlsruhe Institute of Technology)</i>	

Image processing

Independent component analysis of image series for defect detection in textured surfaces	35
<i>L. Nachtigall (Karlsruhe Institute of Technology),</i>	
<i>A. Pérez Grassi (Technische Universität München),</i>	
<i>F. Puente León (Karlsruhe Institute of Technology)</i>	

Segmentation of defect edges on grooved surfaces using anisotropic diffusion	57
<i>L. Wang (Karlsruhe Institute of Technology)</i>	

Powerline communications

Impulsive noise on the low voltage mains grid — detection method, parameter analysis and mitigation of its effects	75
<i>M. Bauer (Karlsruhe Institute of Technology)</i>	

Countering impulsive noise without channel coding 95
M. Bauer (Karlsruhe Institute of Technology),
M. Kruse (Karlsruhe Institute of Technology)

Robustness testing of an FSK PLC physical layer implementation
by means of a channel emulator 113
M. Bauer (Karlsruhe Institute of Technology),
W. Liu (Karlsruhe Institute of Technology)

Least-squares-estimation based zero-crossing prediction for an
automated PLC channel measurement system 129
W. Liu (Karlsruhe Institute of Technology),
Y. Bao (Karlsruhe Institute of Technology)

Robotics and autonomous systems

Information fusion for environment exploration 147
M. Heizmann (Fraunhofer IOSB, Karlsruhe),
I. Gheța (Karlsruhe Institute of Technology),
F. Puente León (Karlsruhe Institute of Technology),
J. Beyerer (KIT and Fraunhofer IOSB, Karlsruhe)

Classification of partly occluded pedestrians 167
V. Frolov (Karlsruhe Institute of Technology)

Automotive

Cost-efficient environment perception using multiple sensors for
driver assistance systems in commercial vehicles 181
C. Otto (Daimler AG),
U. Wiesel (Daimler AG),
J. Wirnitzer (Daimler AG),
A. Schwarzhaupt (Daimler AG),
F. Puente León (Karlsruhe Institute of Technology)

Highly efficient load distribution of parallel DC-DC converters 193
A. Suchanek (Karlsruhe Institute of Technology),
F. Puente León (Karlsruhe Institute of Technology),
A. Jost (Daimler AG)

Wavelet packet analysis of knock sensor signals for diagnosis of
the gasoline direct injection process 203
 K. Christ (Karlsruhe Institute of Technology),
 T. Kieweler (Karlsruhe Institute of Technology),
 E. Serbetci (Karlsruhe Institute of Technology),
 U. Kiencke (Karlsruhe Institute of Technology)

Preface

The Institute of Industrial Information Technology (IIIT) at the Karlsruhe Institute of Technology (KIT) has been established in 1992. During its almost two decades of existence, the IIIT has become an active partner of many academic and industrial organizations. Despite the important changes which occurred during the last two years—more than half of our scientific staff was renewed, and KIT was founded by a merger of Forschungszentrum Karlsruhe and Universität Karlsruhe—we have maintained continuity in both research and teaching. Our research interests are currently in signal and image processing, pattern recognition, distributed systems, powerline communications, automotive applications, and robotics.

The present volume addresses some of the main topics of our research activities and presents selected results achieved during the last two years. These results have contributed to many cooperative projects with partners from academia and industry.

Without doubt, the most important factor that has contributed to our success has been the highly motivated team of scientists and students who decided to join the IIIT. We would like to thank all of them for the excellent working atmosphere as well as for their fruitful and intensive collaboration, learning from and helping each other. Deep thanks deserves our esteemed former Institute Director, Professor Uwe Kiencke, for his valuable and unconditional support.

Karlsruhe, March 2010

Fernando Puente León
Klaus Dostert

Mailing address:

Institute of Industrial Information Technology (IIIT)
Karlsruhe Institute of Technology (KIT)
Hertzstraße 16, Bldg. 06.35
D-76187 Karlsruhe
E-mail: {puente, dostert}@kit.edu

Comparison of ICA algorithms for underdetermined blind source separation

Andreas Sandmair and Alam Zaib

Karlsruhe Institute of Technology (KIT),
Institute of Industrial Information Technology (IIIT),
Hertzstr. 16, D-76187 Karlsruhe

Abstract Independent Component Analysis (ICA) is a powerful statistical signal processing technique having newly emerging application areas such as blind separation of mixed signals, analysis of data or feature extraction. Blind source separation (BSS) for example involves extracting the source signals from sensor observations which are unknown (linear) mixtures of unobserved source signals. The standard ICA is restricted to determined cases (no. of signals equal to no. of sensors). Within the following paper we compare two different methods for underdetermined blind source separation and evaluate these methods with respect to accuracy and usability.

1 Introduction

Many real world problems tend to be inherently blind in a sense that both the input and the system states are unknown. They have to be estimated, observing only the output signals. Hence, blind signal processing (BSP) techniques [1] are becoming a predominant and active area of research in signal processing. Independent component analysis is one of the most recently developed BSP techniques to solve blind source separation. Considering determined or overdetermined cases, where the number of sensors is equal to or greater than the number of sources, multiple solutions have been presented.

A very famous example of BSS is the cocktail party phenomenon, describing the human ability to focus on a desired speech embedded in a mixture of other sources and background noise. Under special conditions, the problem can technically be solved. In a real world environment, the

assumption of a determined case is normally not valid and an adequate solution is much more difficult to obtain. Nevertheless, there are some algorithms for the underdetermined cases that can be used.

Within this paper, two different algorithms for underdetermined ICA are presented and evaluated with respect to blind source separation. The organization of the paper is as follows: In Section 2 basic principles for independent component analysis are introduced and two different approaches for underdetermined ICA are described. These approaches are evaluated in Section 3 with respect to the applicability for BSS in speech signal processing. Finally, a conclusion and an outlook are presented.

2 Overcomplete or underdetermined ICA

2.1 ICA model

The aim of independent component analysis is the decomposition of mixed signals into their original components, whereas little information about the mixture is available. Regarding a superposition of N sources, the signal at the j -th sensor is

$$x_j(t) = a_{j1} s_1(t) + \dots + a_{jN} s_N(t). \quad (1.1)$$

Recording the signals using M sensors, the dataset can be written in matrix notation

$$\mathbf{x}(t) = A \mathbf{s}(t) = \sum_{i=1}^N \mathbf{a}_i s_i(t), \quad (1.2)$$

where A is an unknown mixing matrix with components a_{ji} , $\mathbf{s}(t) = [s_1(t), \dots, s_N(t)]^T$ is the N -dimensional source data and $\mathbf{x}(t) = [x_1(t), \dots, x_M(t)]^T$ is the observed data. The columns \mathbf{a}_i of the matrix can be interpreted as basis vectors/functions and s_i as coefficients. The previous equation is referred to as ICA model. Under certain conditions, the signals can be reconstructed.

Basically, the model above is valid for an arbitrary number of sources. If the number of sources is equal to the number of sensors, an exact reconstruction of the source signals is possible by estimating a matrix W as the inverse of the mixing matrix A , using basic ICA methods [2, 3], so that $\mathbf{s}(t) = W \mathbf{x}(t)$. If there are less sensors than sources, the

problem is referred to as overcomplete or underdetermined, which is more difficult to handle than the ordinary ‘square matrix’ mixing problem. Overcomplete representations have been advocated because they have a greater robustness in the presence of perturbations in the signal or noise, can be sparser and offer greater flexibility in matching the structure of the data. This can be used to solve BSS problems with fewer sensors than sources. The benefit of an overcomplete representation is illustrated in Figure 1.1, where three sparse sources have been mixed to produce a two dimensional mixture data space. We can see that the complete ICA cannot model the data distribution adequately with three sources, while the overcomplete representation finds three basis vectors that fit the underlying data distribution. Thus, using overcomplete bases, which allow a greater number of basis functions (vectors) than in the complete case, is potentially a more general method of signal representation.

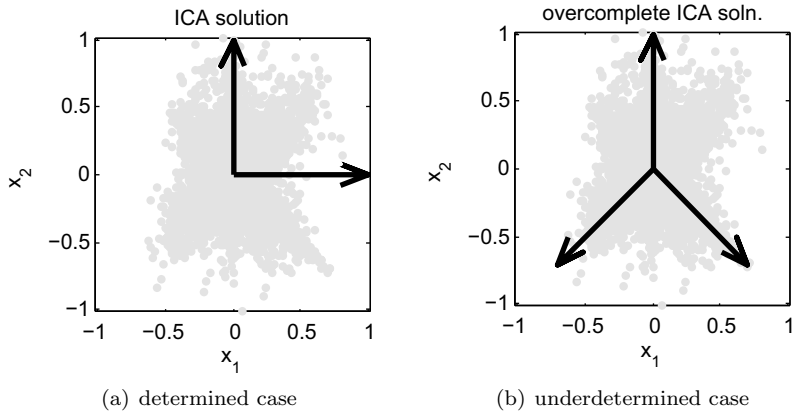


Figure 1.1: Possible solutions for BSS.

Unlike in the case of a complete basis, where signal decomposition is well defined and unique (because of a square mixing matrix), finding the ‘best’ representation in terms of an overcomplete basis is a challenging problem because the signal representation is not a unique combination of the basis functions (vectors). In the context of BSS, the problem of estimating original sources from sensor observations involves now two

separate problems. One is to estimate the mixing matrix, referred to as matrix recovery step, and the other is to estimate the original sources, also called source inference step. This is in sheer contrast with standard mixing problems, where source inference is trivially done by inverting the mixing matrix. It is also worth mentioning that even if the mixing matrix is perfectly estimated, the original sources cannot be recovered perfectly because some information is permanently lost in the representation. Two approaches to tackle underdetermined BSS problems will now be discussed, namely classical and geometric BSS.

2.2 Classical approach

In the classical approach the decomposition problem is solved by regarding Equation (1.2) as a probabilistic model of the observed data. The redundancy in the data representation can be removed by a proper choice of the prior probability of the basis coefficients $P(\mathbf{s})$. The prior probability affects the modeling of the underlying statistical structure and the nature of the representation. First, we discuss the source inference step assuming that the mixing matrix has already been estimated.

Source inference

Assuming that an estimate of the original mixing matrix has been found, we are left with the problem of reconstructing the original sources using the mixtures $\{\mathbf{x}(1), \dots, \mathbf{x}(T)\}$ ($M \times T$) and the estimated matrix A ($M \times N$). Because $N > M$, the source recovery problem is ill-posed without further assumptions. An often used assumption [4] can be derived using a maximum likelihood approach as is shown next [5].

The problem of source inference can be formulated as follows: Given a random vector $\mathbf{x} \in \mathcal{R}^M$ and a matrix A as above, find an independent vectors satisfying an assumption (to be defined) such that $\mathbf{x} = A\mathbf{s}$. Since \mathbf{x} can be determined by A and \mathbf{s} , the probability of observing \mathbf{x} given A and \mathbf{s} can be written as $P(\mathbf{x}|\mathbf{s}, A)$. Using the Bayes rule, the posterior probability of \mathbf{s} is defined as

$$P(\mathbf{s}|\mathbf{x}, A) = \frac{P(\mathbf{x}|\mathbf{s}, A) \cdot P(\mathbf{s})}{P(\mathbf{x})}, \quad (1.3)$$

which is the probability of an event of \mathbf{s} after knowing \mathbf{x} and A . Given some samples of \mathbf{x} , a standard approach for reconstructing \mathbf{s} is the

maximum-likelihood algorithm, which means maximizing this posterior probability after knowing the prior probability $P(\mathbf{s})$. Using the observed samples one can find the most probable \mathbf{s} so that $\mathbf{x} = A\mathbf{s}$. This can be regarded as a decomposition of \mathbf{x} into the most probable coefficients s_i with respect to the corresponding overcomplete basis $\{\mathbf{a}_i\}$.

Thus, unknown sources are estimated by solving the problem:

$$\hat{\mathbf{s}} = \underset{\mathbf{x}=A\mathbf{s}}{\operatorname{argmax}} (P(\mathbf{s}|\mathbf{x}, A)) = \underset{\mathbf{x}=A\mathbf{s}}{\operatorname{argmax}} (P(\mathbf{x}|\mathbf{s}, A) \cdot P(\mathbf{s})). \quad (1.4)$$

Since \mathbf{x} is fully determined after knowing \mathbf{s} and A , $P(\mathbf{x}|\mathbf{s}, A)$ can be calculated. $P(\mathbf{x}|\mathbf{s}, A)$ only depends on the proper choice of $P(\mathbf{s})$, so Equation (1.4) can be simplified:

$$\hat{\mathbf{s}} = \underset{\mathbf{x}=A\mathbf{s}}{\operatorname{argmax}} (P(\mathbf{s})). \quad (1.5)$$

Gaussian Prior

If we assume $P(\mathbf{s})$ to be Gaussian distributed, then Equation (1.5) leads to

$$\begin{aligned} \hat{\mathbf{s}} &= \underset{\mathbf{x}=A\mathbf{s}}{\operatorname{argmax}} (e^{-|s_1|^2 - \dots - |s_n|^2}) \\ &= \underset{\mathbf{x}=A\mathbf{s}}{\operatorname{argmin}} (|s_1|^2 + \dots + |s_n|^2) = \underset{\mathbf{x}=A\mathbf{s}}{\operatorname{argmin}} \|\mathbf{s}\|_2 = A^+ \mathbf{x}. \end{aligned} \quad (1.6)$$

In this case, the solution is unique and the source estimation is achieved by the Moore-Penrose or pseudo inverse A^+ . However, in ICA we are not much interested in Gaussian distributed sources [1].

Laplacian Prior

This is the case we are more interested in (speech signals are Laplacian distributed). Thus, assuming $P(\mathbf{s})$ to be Laplacian, i.e., $P(s_i) = e^{-|s_i|}$, Equation (1.5) gives

$$\begin{aligned} \hat{\mathbf{s}} &= \underset{\mathbf{x}=A\mathbf{s}}{\operatorname{argmax}} (e^{-|s_1| - \dots - |s_n|}) \\ &= \underset{\mathbf{x}=A\mathbf{s}}{\operatorname{argmin}} (|s_1| + \dots + |s_n|) = \underset{\mathbf{x}=A\mathbf{s}}{\operatorname{argmin}} \|\mathbf{s}\|_1, \end{aligned} \quad (1.7)$$

where $\|\mathbf{s}\|_1$ denotes the 1-norm.

Linear Programming

The minimization problem mentioned above can be reformulated as

$$\hat{\mathbf{s}} = \underset{\mathbf{s}}{\operatorname{argmin}} (\mathbf{c}^T \mathbf{s}) \quad \text{subject to } \mathbf{x} = A \mathbf{s}, \quad (1.8)$$

where \mathbf{c} is a vector with coefficients equal to 1. This is not a linear programming (LP) problem because of the non-linear absolute value function. The problem can be transformed into a standard LP problem (with only positive coefficients) by separating the positive and negative coefficients [6]. Making the substitutions

$$\mathbf{s} \leftarrow [\mathbf{u}; \mathbf{v}] \quad \mathbf{c} \leftarrow [1; 1] \quad A' \leftarrow [A; -A],$$

Equation (1.8) becomes

$$\hat{\mathbf{s}} = \underset{\mathbf{s}}{\operatorname{argmin}} (\mathbf{c}^T [\mathbf{u}; \mathbf{v}]) \quad \text{subject to } \mathbf{x} = A' \mathbf{s}. \quad (1.9)$$

This separates the positive and negative coefficients of the solution \mathbf{s} into the positive variables \mathbf{u} and \mathbf{v} . The problem can now be solved efficiently and exactly with interior point linear programming methods.

Gradient Ascent

The gradient ascent rule for maximizing the posterior distribution in Eq. (1.4) can be easily derived [7] by assuming that T independent data samples $\{\mathbf{x}(1), \dots, \mathbf{x}(T)\}$ are observed, generated according to the extended ICA model $\mathbf{x} = A\mathbf{s} + \mathbf{n}$, where \mathbf{n} is the noise vector with zero mean and the covariance matrix Σ . Under such assumptions, the posterior probability is

$$P(\mathbf{s}|\mathbf{x}, A) = \prod_{t=1}^T P(\mathbf{s}(t)|\mathbf{x}(t), A). \quad (1.10)$$

For each data sample, the Bayes rule implies

$$\begin{aligned} P(\mathbf{s}(t)|\mathbf{x}(t), A) &= \frac{P(\mathbf{x}(t)|\mathbf{s}(t), A) \cdot P(\mathbf{s}(t))}{\int P(\mathbf{x}(t)|\mathbf{s}(t), A) \cdot P(\mathbf{s}(t)) \, d\mathbf{s}} \\ &= \frac{P(\mathbf{x}(t)|\mathbf{s}(t), A) \cdot P(\mathbf{s}(t))}{P(\mathbf{x}(t))}. \end{aligned} \quad (1.11)$$

According to the ICA model, we have

$$P(\mathbf{x}(t)|\mathbf{s}(t), A) = |\det(2\pi\Sigma)|^{-1/2} \exp\left(-\frac{1}{2}(\mathbf{x}(t) - A\mathbf{s}(t))^T \Sigma^{-1} (\mathbf{x}(t) - A\mathbf{s}(t))\right). \quad (1.12)$$

Inserting the previous equations into Eq. (1.10) the log-likelihood (LLH) is obtained by taking the logarithm of Eq. (1.10) as

$$L(\mathbf{s}) = \left(-\frac{1}{2}(\mathbf{x}(t) - A\mathbf{s}(t))^T \Sigma^{-1} (\mathbf{x}(t) - A\mathbf{s}(t)) + \varphi(\mathbf{s}(t))\right) + C, \quad (1.13)$$

where $\varphi(\mathbf{s}(t)) = \log(P(\mathbf{s}(t)))$ is a certain non-linear function and C is a constant independent of $\mathbf{s}(t)$. To infer the most probable source signals, one can maximize Eq. (1.13) by the gradient ascent rule. Taking the gradient of this LLH function w.r.t. $\mathbf{s}(t)$ yields

$$\Delta_{\mathbf{s}(t)} L(\mathbf{s}(t)) = A^T \Sigma^{-1} (\mathbf{x}(t) - A\mathbf{s}(t)) + \Delta_{\mathbf{s}(t)} \varphi(\mathbf{s}(t)). \quad (1.14)$$

Thus, the following gradient learning rule is obtained:

$$\mathbf{s}^j(t) = \mathbf{s}^{j-1}(t) + \eta \Delta_{\mathbf{s}(t)} L(\mathbf{s}(t)), \quad (1.15)$$

where η refers to a certain learning rate and $\mathbf{s}^{j-1}(t)$ is the vector computed in the previous iteration. The initial value is chosen randomly.

Although the LP method is superior for finding exact solutions in the case of zero noise, it is much slower than the gradient method. The gradient method is faster in obtaining an approximate solution and can be adapted to more general models of different prior distributions.

Matrix recovery

Different methods have been proposed to estimate the mixing matrix A in underdetermined problems [4, 8]. First, the classical method is considered, which deals with the problem in a probabilistic framework.

Following [8], the problem can be stated as finding a set of basis functions (vectors) \mathbf{a}_i describing the structure of the data best in terms of a linear superposition of sparse, statistically independent sources. In terms of probability theory language, we can say that we wish to match the

distribution of data arising from our linear model (Eq. (1.2)) $P(\mathbf{x}|A)$ to the actual distribution of observed data \mathbf{x} , i.e., $P^*(\mathbf{x})$. In other words, if we generate data stochastically by drawing each s_i in Equation (1.2) independently from a distribution (e.g., Laplacian), how would the probability distribution of the generated data \mathbf{x} look like and how could we adapt A to resemble the distribution of the observed data? In order to calculate the probability of data arising from the model, we need to specify the prior probability distribution over the coefficients $P(\mathbf{s})$ as well as the probability of a data point arising from a certain state of coefficients in the model, $P(\mathbf{x}(t)|\mathbf{s}(t), A)$. Once we have these two probabilistic aspects, the probability of a sample arising from the model is given by

$$P(\mathbf{x}(t)|A) = \int P(\mathbf{x}(t)|\mathbf{s}(t), A) P(\mathbf{s}) d\mathbf{s}. \quad (1.16)$$

The probability $P(\mathbf{x}(t)|\mathbf{s}(t), A)$ essentially describes our model of the level of noise or uncertainty. If we assume additive white Gaussian noise (AWGN), the ICA model becomes $\mathbf{x} = A\mathbf{s}$ and the probability is given by Eq. (1.12). Now, assuming the observed T data samples $\mathbf{x}(1), \dots, \mathbf{x}(T)$ to be independent of each other, we get the probability of data arising from the model as

$$P(\mathbf{x}|A) = \prod_{t=1}^T P(\mathbf{x}(t)|A), \quad (1.17)$$

where the factor in the product is defined in Eq. (1.16). A natural choice of assessing how well the distribution in the previous equation matches the actual distribution of the observed data $P^*(\mathbf{x})$ is to take the Kullback-Leibler (KL) divergence between the two distributions given by

$$\begin{aligned} \text{KL} &= \int P^*(\mathbf{x}) \log \frac{P^*(\mathbf{x})}{P(\mathbf{x}|A)} d\mathbf{x} \\ &= \int P^*(\mathbf{x}) \log P^*(\mathbf{x}) d\mathbf{x} - \int P^*(\mathbf{x}) \log P(\mathbf{x}|A) d\mathbf{x}. \end{aligned} \quad (1.18)$$

The greater the difference between the two distributions, the greater will be KL. It is zero if and only if the two distributions are equal. So our objective is to minimize KL by a proper choice of A . Because

$P^*(\mathbf{x})$ is fixed, minimizing KL is equivalent to maximizing $\log P(\mathbf{x}|A)$. Summarizing the whole idea, the goal of learning is to solve the following problem:

$$\text{Maximize: } \log(P(\mathbf{x}|A)) = \sum_{t=1}^T \log(P(\mathbf{x}(t)|A)). \quad (1.19)$$

Taking the gradient of Eq. (1.19) w.r.t. A and using the approximation of Eq. (1.16) with a Gaussian around the posterior mode $\hat{\mathbf{s}}$, a learning rule has been derived in [4] and is given by:

$$\Delta A = A A^T \frac{\partial}{\partial A} \log P(\mathbf{x}|A) \approx A (\Phi(\hat{\mathbf{s}})\hat{\mathbf{s}}^T + I), \quad (1.20)$$

where $\Phi(\hat{\mathbf{s}}_i) = \frac{\partial \log P(\hat{\mathbf{s}}_i)}{\partial \hat{\mathbf{s}}_i}$ is called the score function. If the mixing matrix A is square, the previous equation is equal to the natural gradient ICA learning rule for the basis matrix [9].

Note that each iteration step requires the computation of $\hat{\mathbf{s}}$ as given in the source inference step. Thus, both the estimation and the source reconstruction steps are fused together, which makes the problem more complicated and computationally more expensive. However, this is numerically stable as no matrix inversions are required. It also works for square mixing matrices, thus generalizing the methods of standard ICA.

2.3 Geometrical approach

Geometric approaches have gained some attention due to their pictorial description, low computational cost and relative ease of implementation. Further, they do not require the estimation of higher order statistics. The geometric approach to ICA was first proposed by Puntonet [10] and successfully used for separating real world data. The basic idea of the geometric approaches is to use the concept of independence from a geometrical point of view. The mixing effect is similar to a geometrical transformation of a rectangle to a parallelogram during the whitening step. In this case, we can find the angle of rotation to recover the original sources either in the mixture or in the whitened space using ordinary geometric algorithms [11, 12]. The theoretical background for geometric ICA has been studied in detail and a convergence condition has been derived, which then resulted in a faster geometric algorithm called FastGeo [13].

The ideas of geometric algorithms have been successfully generalized to overcomplete and higher-dimensional systems [5].

Source inference

The reconstruction of sources can be done using the methods presented in Section 2.2.

Matrix recovery

In the geometric approach, the goal is to identify directions where maxima of the data distributions are located. These directions are assumed to correspond to the original basis vectors. Therefore, the algorithm depicted in Figure 1.2 [5] was developed.

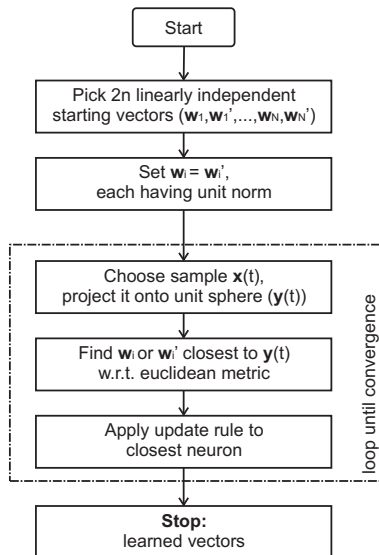


Figure 1.2: Flowchart for the geometrical algorithm.

The idea of identifying the axis of maximum distributions is implemented as an unsupervised neural net with competitive learning, con-

taining $2N$ elements (neurons).

The key elements of the algorithm (Figure 1.2) are

- initializing $2N$ elements (randomly),
- projecting the samples onto the unit sphere,
- calculating the proximity of the projection of the input data sample $\mathbf{y}(t) = \frac{\mathbf{x}(t)}{|\mathbf{x}(t)|}$ to each element with respect to the Euclidean metric,
- applying the update rule (Equation (1.21)) to the closest or winning neuron.

The update rule is defined as

$$\begin{aligned}\mathbf{w}_i(t) &= \text{Pr} [\mathbf{w}_i(t) + \eta(t) \text{sgn}(\mathbf{y}(t) - \mathbf{w}_i(t))] \\ \mathbf{w}'_i(t) &= -\mathbf{w}_i(t),\end{aligned}\tag{1.21}$$

where Pr denotes the projection onto a unit sphere. All other neurons are not moved within this iteration. Note that the step size $\eta(t)$ does not depend on the Euclidean distance.

A frequency f_i is assigned to each element (neuron), which counts the number of times each neuron w_i has won. The step size is then modified according to

$$\eta(t+1) = \eta_0 e^{-f_i(t)/\tau}.\tag{1.22}$$

To prevent the network from becoming stuck in a meta-stable state, the learning rate is maintained at a certain low level η .

Modifications of the geometric approach

To improve the convergence and the accuracy, the geometrical algorithm can be modified. An extended algorithm was designed, considering the following enhancements:

- Adaptive Initialization

Our approach to improve the performance of the geometric algorithm is based on an adaptive initialization of the basis vectors instead of random initialization. By adaptive we mean that the algorithm must be able to adapt the initial basis vectors approximately to the true basis vectors of the underlying distribution of

the data. The main idea is to first start with a large number of independent basis vectors, say N^* ($> N$) instead of the true number N , which span the whole data space. Then, after a predefined interval length, only those N independent vectors that have the highest frequencies are retained, because the vectors with higher frequency ranks correspond approximately to the directions of the maximum data distributions. This approach can also be analogously described in the language of neural networks as follows: We first set up a large neural network driven by observed data, which sequentially arrives at the input. Neurons activity is generated according to the received data samples. After a fixed interval length the large network is trimmed, leaving only the most active neurons in the network.

- Weighting of data samples

Due to the fact that data samples close to the origin do not contribute much to the directions in the data, appropriate weighting of the samples according to their norm, can help to improve the performance. Data samples farther from the origin are weighted higher than the ones close to the origin, by adding a weighting factor to the update rule of Eq. (1.21). The weighting factor is considered in all simulations of the geometric algorithm presented in this paper.

3 Evaluation of ICA

Having discussed both the classical and the geometric approaches for estimating an overcomplete basis for BSS, we now present some source separation examples in order to ascertain salient features of both approaches. At the end, they will be compared in terms of accuracy, reliability and computational cost.

3.1 Simulation setup

The speech signals and mixing matrices from [14] were used. The number of sensors is chosen to be two, whereas the number of sources is varying between two and four.

3.2 Performance indices

To compare the mixing matrix A with the estimated mixing matrix B , a generalized crosstalking error $E(A, B)$ of A and B given in [5], defined as

$$E_1 = E(A, B) = \min \|A - BM\| \quad \forall M \in \pi, \quad (1.23)$$

is calculated. π is a group of all invertible real $N \times N$ matrices of which only one entry in each column differs from zero which have a fixed matrix norm (i.e., π contains all possible permutations of the identity matrix). Note that E_1 is zero if and only if A is equivalent to B , which is the case when the mixing matrix has been recovered perfectly (of course up to scaling and permutation) and is always positive otherwise. Thus, E_1 gives a measure of quality of the estimation. A higher E_1 indicates a lower quality or accuracy of the algorithm.

3.3 Comparison

Comparing basic approaches for overcomplete independent component analysis, the accuracy of the classical (LS) algorithm is distinctly better than that of the geometric (Geo) approach. Besides lower mean values (Table 1.1), there are few outliers as can be seen in Figure 1.3. However the computation time (Table 1.2) is much higher. Therefore a good overall performance cannot be guaranteed.

No. of sources	2	3	4
LS	0.0099	0.0205	0.0535
Geo	0.0898	0.1024	0.0900

Table 1.1: Median error for 100 independent trials.

No. of sources	2	3	4
LS	80.095	92.7935	98.9290
Geo	1.1039	3.4250	8.2560

Table 1.2: Average computation time [s] for 100 independent trials.

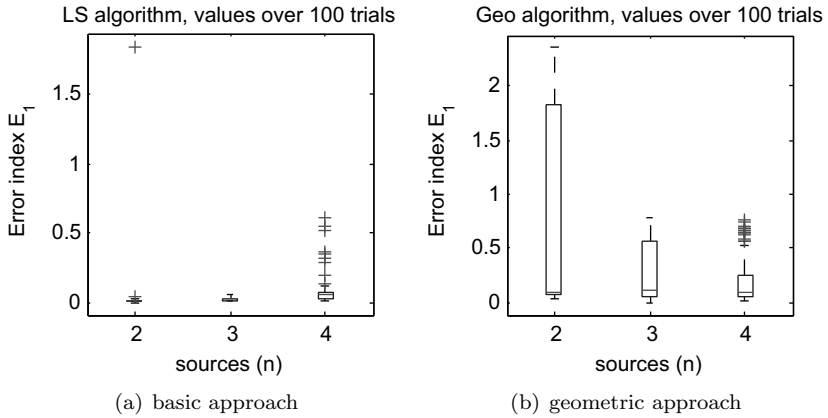


Figure 1.3: Comparison of the classical and the basic geometrical approach. Results are plotted using Box Whisker Plot, where the bottom and top of the box are always the 25th and 75th percentile and the band is the median. Whisker length is 1.5.

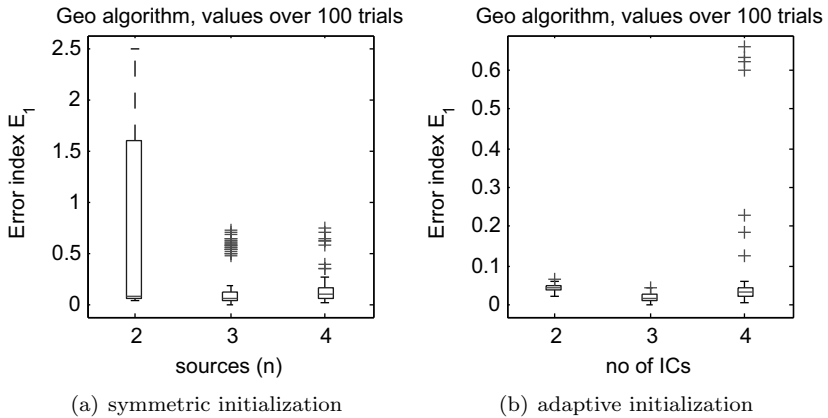


Figure 1.4: Improving the geometrical approach using symmetric [5] and adaptive initialization.

No. of sources	2	3	4
symmetric	0.0767	0.0653	0.0955
adaptive	0.0708	0.0188	0.0367

Table 1.3: Median error for improved geometrical algorithms.

No. of sources	2	3	4
symmetric	1.0830	3.4665	8.420
adaptive	2.259	6.4760	12.7270

Table 1.4: Average computation time [s] for 100 improved geometrical algorithms.

Due to the complexity of the classical algorithms, improvements of the geometrical algorithm have been done. By initializing starting vectors symmetrically [5], the accuracy can be improved, as can be seen in Figure 1.4(a) and Table 1.3. Using adaptive initialization, the error can be reduced further. In addition, the number of outliers could be reduced significantly. The computation time of the adaptive algorithms is greater than the computation time of the other geometrical algorithms, due to the adaptive initialization (Table 1.4). Learning more vectors is more time consuming.

4 Conclusion

In a real environment, blind source separation is very difficult due to multiple reasons. Beyond problems like scattering or reflections, an unknown number of sources is a challenging problem. Assuming that the number of sources can be estimated, it seems unlikely that the number of sources is equal to the number of sensors. Especially if the problem is underdetermined (more sources than sensors), the principal ICA approach cannot be used. Therefore, two different approaches to handle the described scenario have been presented: a classical and a geometrical approach. Additionally, an adaptive method for initialization has been developed for the geometric approach. Evaluating both approaches, it has been shown that the applicability of the classical approach is limited due to high computational costs. By improving the geometrical approach

using methods for intelligent initialization, an accuracy comparable to that of the classical approach can be achieved.

For further work, methods for handling an unknown number of sources should be developed. For applicability in real world scenarios, an improvement of the computation time is desirable.

References

1. P. O’Grady, B. Pearlmutter, and S. Rickard, “Survey of sparse and non-sparse methods in source separation,” *International Journal of Imaging Systems and Technology*, vol. 15, no. 1, pp. 18–33, 2005.
2. P. Comon *et al.*, “Independent component analysis, a new concept?” *Signal processing*, vol. 36, no. 3, pp. 287–314, 1994.
3. A. Hyvärinen, J. Karhunen, and E. Oja, “Independent component analysis,” 2001.
4. M. Lewicki and T. Sejnowski, “Learning overcomplete representations,” *Neural computation*, vol. 12, no. 2, pp. 337–365, 2000.
5. F. Theis, E. Lang, and C. Puntonet, “A geometric algorithm for overcomplete linear ICA,” *Neurocomputing*, vol. 56, pp. 381–398, 2004.
6. H. Sawada, S. Winter, R. Mukai, S. Araki, and S. Makino, “Estimating the number of sources for frequency-domain blind source separation,” *Lecture notes in computer science*, pp. 610–617, 2004.
7. Z. Shi, H. Tang, W. Liu, and Y. Tang, “Blind source separation of more sources than mixtures using generalized exponential mixture models,” *Neurocomputing*, vol. 61, pp. 461–469, 2004.
8. B. Olshausen and D. Fteld, “Sparse coding with an overcomplete basis set: A strategy employed by V1?” *Vision research*, vol. 37, no. 23, pp. 3311–3325, 1997.
9. S. Amari, A. Cichocki, and H. Yang, “A new learning algorithm for blind signal separation,” *Advances in neural information processing systems*, 1996.
10. C. Puntonet and A. Prieto, “An adaptive geometrical procedure for blind separation of sources,” *Neural Processing Letters*, vol. 2, no. 5, pp. 23–27, 1995.
11. A. Mansour, C. Puntonet, and N. Ohnishi, “A simple ICA algorithm based on geometrical approach,” in *Sixth International Symposium on Signal Processing and its Applications (ISSPA 2001)*. Citeseer, 2001, pp. 9–12.

12. B. Prieto, C. Puntonet, P. Martín-Smith, and A. Prieto, “Demixing of linear mixtures of unimodal supergaussian signals based on geometric properties,” Workshop on Independent Component Analysis and Signal Separation, June 2000.
13. F. Theis, A. Jung, C. Puntonet, and E. Lang, “Linear geometric ICA: Fundamentals and algorithms,” *Neural Computation*, vol. 15, no. 2, pp. 419–439, 2003.
14. T. Lee, M. Lewicki, M. Girolami, T. Sejnowski *et al.*, “Blind source separation of more sources than mixtures using overcomplete representations,” *IEEE Signal Processing Letters*, vol. 6, no. 4, pp. 87–90, 1999.

Extension of Particle Swarm Optimization for detection of local minima

Andreas Sandmair and Norbert Linzenkirchner

Karlsruhe Institute of Technology (KIT),
Institute of Industrial Information Technology (IIT),
Hertzstr. 16, D-76187 Karlsruhe

Abstract The objective of any optimization algorithm is finding the global best (minimum or maximum) of an arbitrary function. Depending on the complexity of the function, deterministic methods do not always lead to success. Therefore, the application of ‘intelligent’ algorithms for solving optimization problems has increased during the last few decades. Due to an included randomness, these kinds of algorithms produce good results. Particle Swarm Optimization (PSO) is a well-known representative of this group of methods. Within this paper we present an extension of PSO for detecting local minima and an underlying structure by adding some migratory behaviour. This algorithm is used for detection of a disturbed linear structure defined by multiple minima.

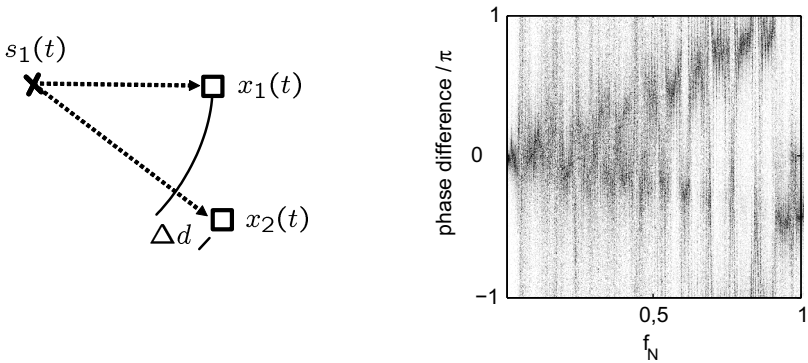
1 Introduction

The cocktail party effect describes the human ability to focus on the discussion partners, also in presence of ambient noise (music, further conversations, etc.) [1]. By evaluating the inter-aural time difference (ITD) and the inter-aural level difference (ILD) between the left and the right ear, human beings are able to detect the directions of sound and amplify relevant signals adaptively. Regarding the performance, neuronal information processing is far superior to existing technical systems for the separation of speech signals. Unfortunately, neuronal information processing is not completely investigated and an adequate implementation is not possible. Separation of mixed speech signals in technical systems can

only be done by statistical processing of time delay of arrival. Considering one source signal $s_1(t)$ and two spatial separated sensor signals $x_i(t)$ (Fourier transform of the signal: $X_i(f) = A_i(f)e^{j\varphi_i(f)}$) as presented in Figure 2.1(a), a characteristic, frequency-dependent phase $\Delta\varphi$, depending on the different distances between the source and the sensors, can be calculated:

$$\Delta\varphi(f) = \varphi_2(f) - \varphi_1(f) = 2\pi f \frac{\Delta d}{c_s}, \quad (2.1)$$

c_s is the velocity of sound and $\Delta\varphi(f)$ is a linear function of frequency, representative for one source. The spatial dependence of different sources could be used for separation in technical system. After applying a short-time Fourier transform to the sensor signals, the phase differences can be calculated between corresponding coefficients. Computing a histogram in every frequency bin over a defined time interval, the phase difference can be identified by inspection (Figure 2.1(b)). Due to acoustic effects like reflections and scattering, the linear structure is disturbed.



(a) Delay of arrival depending on different sensor positions

(b) Histograms of phase differences for two spatially separated sources

Figure 2.1: Blind Source Separation based on spatial position of sources.

There exist several techniques for the separation of mixed signals (the described problem is also known as Blind Source Separation) [2, 3]. Most of the approaches are based on a separate reconstruction of the signals in

every frequency bin, using well-known methods like Independent Component Analysis [4, 5]. Thereby, independent phase differences are estimated in every frequency bin, followed by an adaptive combination of the related components. Unfortunately, information about correlation between adjacent frequencies is omitted.

We present a new approach for the detection of the phase differences by analysing a map, based on the histograms for every frequency bin (similar to Figure 2.1(b)). The linear structure and maximum values in the map can be identified using a modification of particle swarm optimization (PSO). To introduce the algorithm we concentrate on one active source as presented above. The paper is organized as follows. In Section 2, basic PSO for detecting global extrema is presented. Extensions to the optimization algorithm are described in Section 3. Within Section 4, the performance of the new algorithm is evaluated before usability and further work is discussed in the last chapter.

2 Particle Swarm Optimization

Particle Swarm Optimization was developed by James Kennedy and Russel Eberhart in 1995 [6]. PSO is a population based algorithm describing mathematically the behaviour of swarms (e.g., foraging) that appear in different areas of nature. Famous examples are swarms of birds or fishes. The fundamental idea is, that the decision making of an individual is influenced by the own decision and the behaviour of the swarm. The major purposes beneath the easy way of implementation, is that there is no need of any gradient information. Opposed to many other population based algorithms, the PSO is a stochastic algorithm. Due to the fact that PSO does not need any gradient information of the error function, it is often used when the calculation of the gradient is very difficult or impossible [7–9].

For solving an optimization problem, the swarm intelligence is described by a mathematical model presented as follows. A swarm consists of N individuals, called particles, and each of these particles can be interpreted as a solution to the optimization problem.

Every particle i contains the following information

\mathbf{x}_i : position of particle i

\mathbf{v}_i : velocity of particle i
 \mathbf{y}_i : best position of particle i so far
 $\hat{\mathbf{y}}$: best position of all/group of particles so far

There are two different possibilities defining $\hat{\mathbf{y}}$. Therefore, two different versions of the PSO algorithm exist, the *gbest* and the *lbest* version. The *gbest* version uses the positions of all the particles to calculate $\hat{\mathbf{y}}$, the *lbest* version uses only a subset of particles to calculate $\hat{\mathbf{y}}$, instead.

The process of optimization is explained based on the single steps illustrated in the following flowchart (Figure 2.2). The single steps are presented for the *gbest* version of PSO algorithm, whereas the modifications for the *lbest* version are defined in Section 2.2.

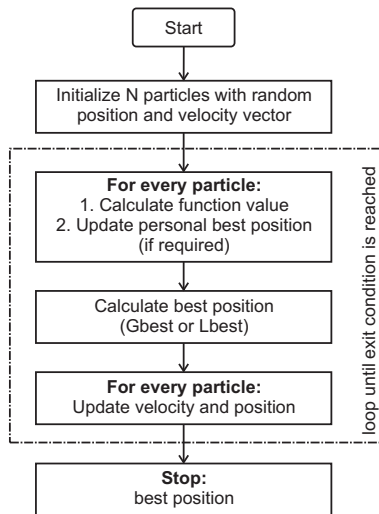


Figure 2.2: General description of the PSO algorithm.

First, N particles are initialized with random position and velocity vectors within a defined environment (limitations of error function). Basic conditions (e.g., restrictions for maximum velocity) can be set and an exit condition (convergence criteria) has to be defined.

The following steps are repeated until a convergence criterion is fulfilled:

- For every particle:
 - Calculate the function value $f(\mathbf{x}_i(t))$ based on the information of step t .
 - Update the personal best position (smallest value passed by particle so far)

$$\mathbf{y}_i(t) = \begin{cases} \mathbf{y}_i(t-1), & \text{for } f(\mathbf{x}_i(t)) \geq f(\mathbf{y}_i(t-1)) \\ \mathbf{x}_i(t), & \text{for } f(\mathbf{x}_i(t)) < f(\mathbf{y}_i(t-1)) \end{cases} \quad (2.2)$$

- Calculate the global best position

$$\hat{\mathbf{y}}(t) = \underset{\mathbf{y}_i(t)}{\operatorname{argmin}} f(\mathbf{y}_i(t)) \quad i \in [1, \dots, N] \quad (2.3)$$

- For every particle
 - Update the velocity:

$$\begin{aligned} \mathbf{v}_i(t) = & \mathbf{v}_i(t-1) + c_1 r_1 [\mathbf{y}_i(t) - \mathbf{x}_i(t)] \\ & + c_2 r_2 [\hat{\mathbf{y}}(t) - \mathbf{x}_i(t)] \end{aligned} \quad (2.4)$$

The two independent random variables r_1 and r_2 are drawn from a uniform distribution on the interval $[0, 1]$ and are the reason for the stochastic nature of the algorithm. The constant factors c_1 and c_2 are called self confidence and swarm confidence and influence the behaviour of the particles.

- Update the position:

$$\mathbf{x}_i(t+1) = \mathbf{x}_i(t) + \mathbf{v}_i(t) \quad (2.5)$$

After updating the velocity, the position can be updated. The strategy for updating is also presented in Figure 2.3.

2.1 gbest version

The relevant equations for the model have been presented in the previous section. In this variation of the PSO algorithm, the global best particle is computed among all particles that belong to the swarm. This leads to a fast convergence, but may end up in a local minimum.

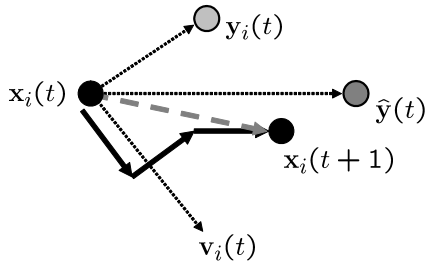


Figure 2.3: Principle approach for PSO; The new position of a particle depends on current velocity $\mathbf{v}_i(t)$, the global best position $\hat{\mathbf{y}}(t)$ and the personal best position $\mathbf{y}_i(t)$.

2.2 lbest version

The *lbest* version computes more than one global best particle through building clusters within the swarm. If a swarm consists for example of N particles, the swarm is divided into K clusters, with $N_{cl} = \frac{N}{K}$ particles per cluster. Assignment to a cluster can depend on the order of the particles (i.e., first cluster contains particles $i \in [1, \dots, N_{cl}]$). To use this, replace Equation (2.3) with

$$\hat{\mathbf{y}}_k(t+1) = \underset{\mathbf{y}_i(t)}{\operatorname{argmin}} f(\mathbf{y}_i(t)) \quad \begin{array}{l} k \in [0, \dots, K-1] \\ i \in [k \cdot N_{cl} + 1, \dots, (k+1) \cdot N_{cl}] \end{array} \quad (2.6)$$

and Equation (2.4) with

$$\mathbf{v}_i(t) = \mathbf{v}_{i-1}(t) + c_1 r_1 [\mathbf{y}_i(t) - \mathbf{x}_i(t)] + c_2 r_2 [\hat{\mathbf{y}}_k(t) - \mathbf{x}_i(t)]. \quad (2.7)$$

The *lbest* variation of the PSO algorithm needs more computation time but it is more likely to avoid the aforementioned case of ending up in a local minimum.

3 Adding migratory behaviour to Particle Swarm Optimization

As described in the introduction, our basic problem is not an optimization problem. We want to find multiple local minima, arranged around

an underlying linear structure. Extending the principle of particle swarm optimization, an algorithm could be designed to solve our task. The principle idea for extension is based on the natural behaviour of some species (e.g., migratory birds). On their way to winter quarters, they stop at resting places for sleeping and food intake. Therefore, interpreting local extrema as sleeping places can be an interesting approach for an algorithm. Based on the presented assumption, the procedure is presented in a flowchart, extending basic PSO.

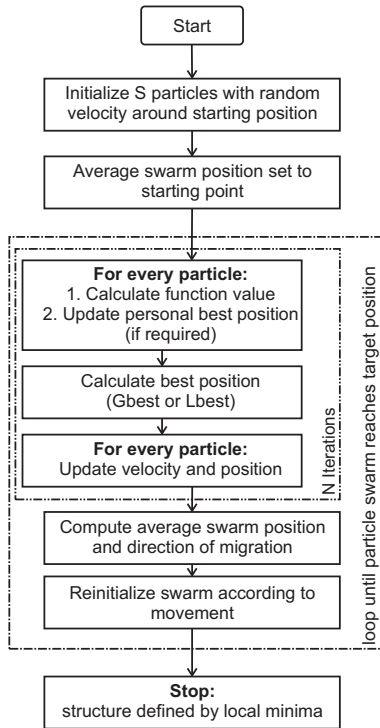


Figure 2.4: General description of the modified PSO algorithm.

The principle steps of the extended algorithm are explained in detail, with regard to our basic problem. Within the presented map (Figure

2.1(b)) a defined starting point can be set ($\Delta\varphi = 0$, $f = 0$). Reaching of f_N by a particle could be defined as exit condition. The cost function is defined by the magnitudes of the histograms.

A swarm with S particles is initialized around the starting point with random velocity. The average swarm position is set to the starting point. Therefore, the initial flight direction (Section 3.1) is defined by the origin of the structure and the first local extremum.

The following steps are repeated until the exit condition is fulfilled:

- Basic PSO (as presented in Section 2) is done, limited by a defined number of iterations. The aim of this optimization is to find some local extrema in a restricted environment around the average swarm position. This step is similar to finding a sleeping place in nature.
- After local optimization a new average swarm position is calculated as the centroid of all particles. A flight direction based on the current average position and the former average values is calculated. The estimation of the flight direction is described in Equation (2.12).
- Reinitialize the swarm according to motion. To avoid a change of direction, a lower bound is defined above the old resting place. Particles cannot fall below. So a principal moving direction is guaranteed. Definition of the boundary is illustrated in Figure 2.5.

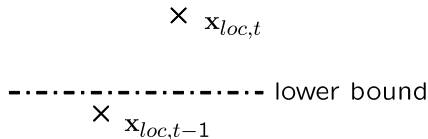


Figure 2.5: Definition of a lower bound. After detection of a local extremum $\mathbf{x}_{loc,t-1}$, the swarm is moved to the next starting point. To avoid multiple detections of this extremum, a boundary is defined that cannot be passed by the particles so that the next extremum $\mathbf{x}_{loc,t}$ is found.

3.1 Determination of flight direction and reinitialization of swarms

In nature there is less knowledge about the route of migratory birds. Within our special problem, the flight direction could be calculated according to the following equations, assuming that the underlying structure is linear.

At first, a variable describing the motion between two optimization steps can be calculate according to

$$\Delta \mathbf{x}_{mov} = \mathbf{x}_{avr}(t) - \mathbf{x}_{avr}(t - 1), \quad (2.8)$$

where $\mathbf{x}_{avr}(t)$ describes the average position of the swarm during step t within a 2-dimensional map. $\Delta \mathbf{x}_{mov} = [x_{mov,1}, x_{mov,2}]^T$ is the temporary direction of motion and can be used to calculate the current flight direction $V(t)$ and the current flight distance $S(t)$.

$$V(t) = \text{atan} \left(\frac{x_{mov,2}}{x_{mov,1}} \right) \quad (2.9)$$

$$S(t) = \sqrt{x_{mov,1}^2 + x_{mov,2}^2} \quad (2.10)$$

Based on the previous results and the basic assumptions, a resulting flight direction V_{res} and flight distance S_{res} can be calculated:

$$\begin{aligned} V_{res}(t) &= \frac{tV(1)+V(t)}{t+1} \\ S_{res}(t) &= \frac{tS(1)+S(t)}{t+1} \end{aligned} \quad (2.11)$$

The choice of the direction and the distance depends mainly on the flight direction and distance calculated at the first step. Using these values, the algorithm delivers good results as presented in following section because a nearly linear movement is guaranteed. Additionally, modeling the flight direction and the distance as a Markov process would be a further possibility.

After calculating the resulting values, every particle i is reinitialized according to

$$\mathbf{x}_i(t+1) = \mathbf{x}_i(t) + S_{res}(t) \cdot [\cos(V_{res}(t)) \quad \sin(V_{res}(t))]^T + \mathbf{R}_{fac} \quad (2.12)$$

where \mathbf{R}_{fac} is a 2-dimensional random vector with components uniformly distributed between 0 and R_{max} . This factor is added to guarantee some stochastic behaviour. The velocity of the particles is chosen randomly.

4 Simulation and results

Within the following section, we focus on the simulation of the extended algorithm. Therefor some test scenarios are defined and repeatable results of PSO evaluation are presented before the algorithm is tested for a nearly realistic scenario.

4.1 Test scenario

Regarding the basic map in Figure 2.1(b), a meaningful evaluation is quite difficult. Just the underlying linear structures are visible but local extrema must be extracted manually before a reliable evaluation can be done. Therefore, a test scenario is defined (size 1000×1000). For local optimization, 25 extrema (called foxholes, according to [10]) are placed symmetrically around a linear structure (25°), as can be seen in Figure 2.6(b). Knowing the exact positions of the structure points, the quality of the algorithm can be evaluated. For a more problem-specific evaluation of our algorithm, a second scenario (Figure 2.6(a)) is defined by smoothing a real map with a 2-dimensional Gaussian kernel. The

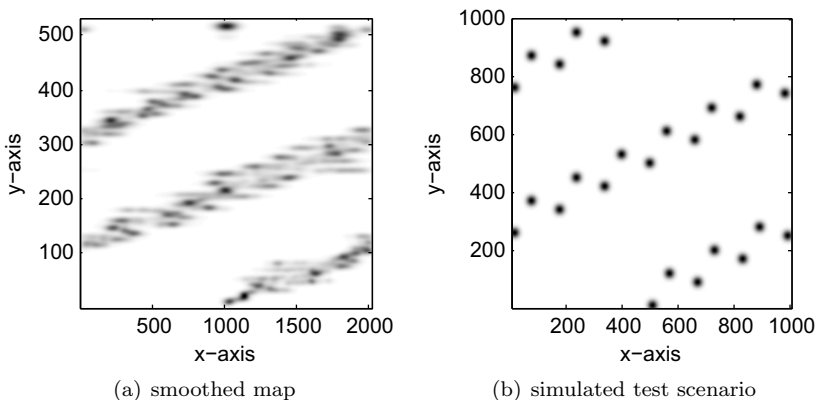


Figure 2.6: Test maps for evaluation of the extended PSO algorithm.

cost function is defined by the test scenario and the starting point for the algorithm is set to $\mathbf{x} = [\frac{\max(x)}{2}, 0]^T$. Comparing the test maps with

the histograms in Figure 2.1, the phase difference corresponds with the x-axis and f_N with the y-axis. More general notations are chosen to emphasize generality of the algorithm.

4.2 Evaluation of modified PSO

For the evaluation of the algorithm, the test scenario described above is used. Within the simulation R_{max} , as defined in Section 3.1, is varied between 0 and 100 and the simulation is repeated 100 times for every R_{max} . At first, the results for three different values of R_{max} are presented in detail (Figures 2.7, 2.8 and 2.9) before the evaluation is discussed in general. For every separate random vector all found positions are plotted within the according figure in the left plot. The nearest distance Δd (average over 100 iterations) to every foxhole is plotted in the right picture. The distance is calculated according to

$$\Delta d = \frac{1}{N} \sum_1^N |\mathbf{x}_{foxhole} - \mathbf{x}_{loc,t}| \quad (2.13)$$

where N is the number of iterations, $\mathbf{x}_{loc,t}$ is the result of the optimization procedure (step t) and $\mathbf{x}_{foxhole}$ is the position of the nearest foxhole.

$R_{max} = 10$

For a small R_{max} , the swarm is reinitialized in a small area around the proposed average position. As can be seen in Figure 2.7(a) nearly all particles are located around a local extremum after the optimization step. Due to a low random value and the predefined lower bound, several particles are arranged near the border. Nevertheless, the minimum distance to the foxholes is very small.

$R_{max} = 40$

For a medium R_{max} , accumulation of particles near the boarder is less dominant. The values are distributed regular along the underlying linear structure. As can be seen in Figure 2.8(b), minimum distance to foxholes is decreasing due to enhanced reinitialization after an optimization step.

$R_{max} = 100$

For large values of R_{max} , the minimum distance to local extrema is growing. The first optimization delivers good results, but after reinitialization

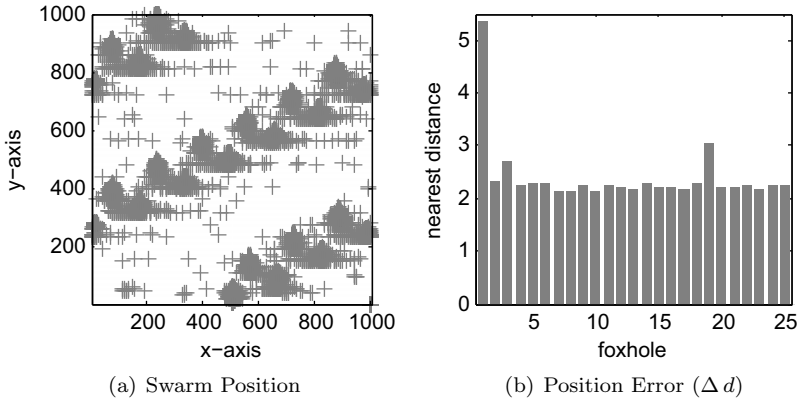


Figure 2.7: Evaluation of extended algorithm for PSO ($R_{max} = 10$); Results after 100 runs.

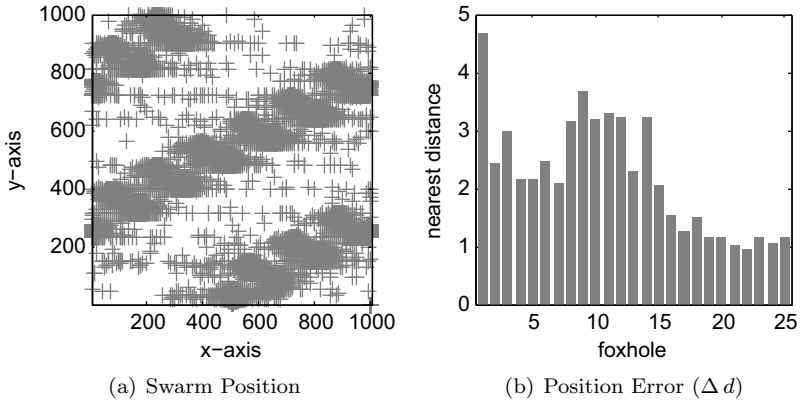


Figure 2.8: Evaluation of extended algorithm for PSO ($R_{max} = 40$); Results after 100 runs.

particles are scattered over a wide area and the algorithm does not reach convergence within N steps. So extrema are mostly not found. The error

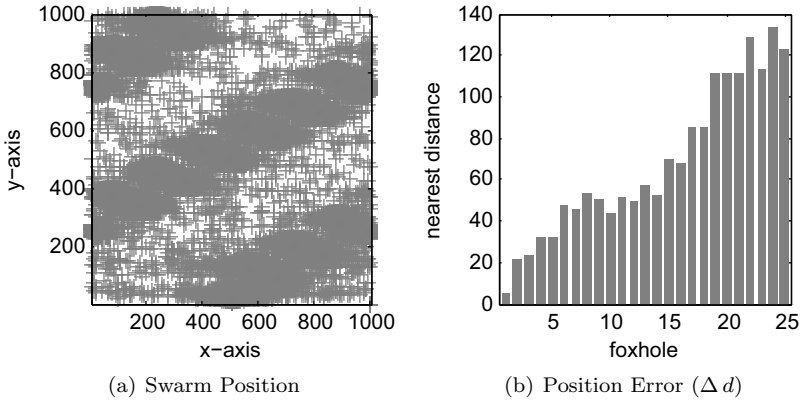


Figure 2.9: Evaluation of extended algorithm for PSO ($R_{max} = 100$); Results after 100 runs.

is growing after every reinitialization step.

Regarding Figure 2.10, the results of the evaluation for every random vector are presented. Average detected points are a measure for global optimization, indicating the ability to find all structure points. In contrast, the average position error is a measure for the quality of local optimization.

Within the presented scenario, R_{max} has to be chosen between 10 and 50 for practical application. With $R_{max} = 0$, the swarm is concentrated after reinitialization around some fixed point. After optimization, all particles are concentrated in a small area around local best and all elements are updated the same way. For high values, predefined iterations are not sufficient for convergence and extrema can be overleaped. For small values of R_{max} , single extrema could be detected multiple times and therefore the number of detected points is higher than the number of existing foxholes.

4.3 Simulating a realistic scenario

For a more application-oriented evaluation of the algorithm, the smoothed map is considered. A maximum random vector of 40 is used.

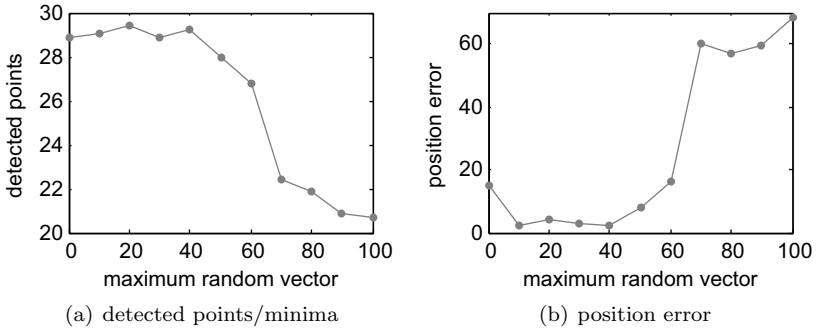


Figure 2.10: Graphical interpretation; detected points indicated global accuracy, position error characterizes local accuracy.

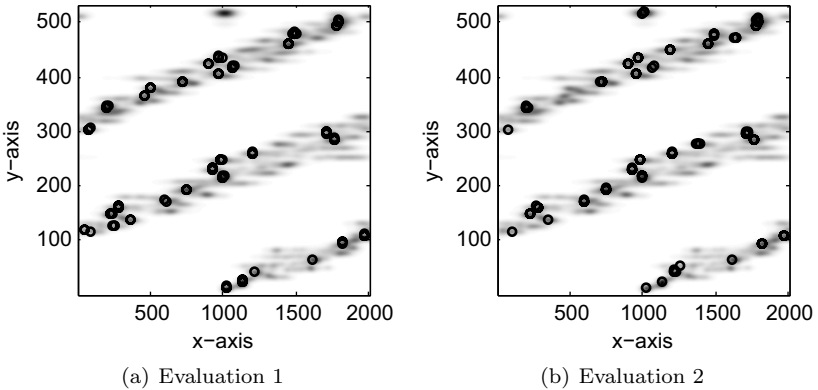


Figure 2.11: Two evaluations of PSO in an almost realistic scenario under equal conditions.

Within Figure 2.11, results of two evaluations are presented. As can be seen, the dominant structure points are found. Due to the stochastic nature of the algorithm, different structure points are found.

5 Summary and outlook

An extension to the basic particle swarm optimization has been presented. After describing PSO and its extension, the modified algorithm was evaluated. The usability of the modified PSO algorithm for the detection of local extrema has been shown.

To improve the presented algorithm, different actions can be taken. The random vector should not be predefined, but calculated from given variables. The estimation of flight direction and distance should be more dynamical and adaptive to the underlying structure.

Under certain conditions, the algorithm could be also used in context of Blind Source Separation. For practical applications, it has to be extended to multiple swarms that follow different sources (linear structures) as shown in Figure 2.1(b). Therefore it is necessary to implement some repulsion between different swarms.

References

1. B. Arons, "A review of the cocktail party effect," *MIT Media Lab*, 1992.
2. P. O'Grady, B. Pearlmutter, and S. Rickard, "Survey of sparse and non-sparse methods in source separation," *International Journal of Imaging Systems and Technology*, vol. 15, no. 1, pp. 18–33, 2005.
3. L. Parra and C. Spence, "Convolutional blind separation of non-stationary sources," *IEEE Trans. Speech and Audio Processing*, vol. 8, no. 3, pp. 320–327, May 2000.
4. A. Bell and T. Sejnowski, "An Information-Maximization Approach to Blind Separation and Blind Deconvolution," *Neural Computation*, vol. 7, no. 6, pp. 1129–1159, 1995.
5. J. Stone, *Independent component analysis*. Cambridge, Mass.: MIT Press, 2004.
6. R. Eberhart and J. Kennedy, "A new optimizer using particle swarm theory," *Sixth International Symposium on Micro Machine and Human Science, IEEE*, 1995.
7. F. van den Bergh, "An analysis of particle swarm optimizers," Ph.D. dissertation, Faculty of Natural and Agricultural Science, University of Pretoria, 2001.
8. J. Kennedy, R. C. Eberhart, and Y. Shi, *Swarm Intelligence*. Morgan Kaufman, 2001.

9. D. Beasley, D. R. Bull, and R. R. Martin, "A sequential niche technique for multimodal function optimization," *In Evolutionary Computation, volume 2, pages 101-125 MIT*, 1993.
10. D. B. Fogel, "An introduction to simulated evolutionary optimization," *IEEE Trans. Neural Networks*, vol. 5, 1994.

Independent component analysis of image series for defect detection in textured surfaces

Luis Nachtigall,¹ Ana Pérez Grassi,² and Fernando Puente León¹

¹ Karlsruhe Institute of Technology (KIT),
Institute of Industrial Information Technology (IIIT),
Hertzstr. 16, D-76187 Karlsruhe

² Technische Universität München,
Lehrstuhl für Messsystem- und Sensortechnik,
Theresienstr. 90/N5, D-80333 München

Abstract The appearance of varnished wood is of crucial importance in the furniture industry. A finishing defect can make a piece inadequate for commercialization. In this sense, the earlier a defect is detected during the manufacturing, the lesser the economical losses it will cause. Therefore, quality control plays a fundamental role in the wood manufacturing process. The introduction of a visual inspection system in a varnishing line would yield significant benefits, due to its repeatability and fast execution time, as opposed to manual-visual inspection. In this paper, a method for detection of topographical defects, based on image series with variable illumination, is presented. The method separates the texture from defects making use of a stochastic generative model that considers features learned by the Independent Component Analysis (ICA) from a training set of surfaces. The output of the algorithm consists of a segmented binary image that highlights the defective areas.

1 Introduction

In the last decades, automated visual inspection has gained relevant importance in the quality control stage of several industrial processes. However, the furniture sector remains to date an exception, where this task is

usually performed by specialized workers, who can identify defects making use of their know-how learned over the years. Due to the subjectivity of the evaluation of the inspectors, the transfer of the know-how into algorithms does not present an easy or straightforward task. Additionally, varnished wood surfaces represent a challenging problem for automated inspection systems, due to several reasons. On the one hand, texture exhibits a great variability between different pieces and types of wood. This means that texture acts as a noisy background, which complicates the defect detection process. On the other hand, defects on varnished or painted surfaces can hardly be distinguished under some specific directions of illumination and observation. This sort of surfaces are called ‘non-collaborative’ [1]. Despite all these difficulties, automated visual inspection is highly desirable, mainly due to the economic benefits that an online system would introduce and the more objective and repeatable results it can yield.

As for every visual system, the success of the results depends strongly on the quality of the images obtained in the acquisition step. The fact that defects are only partially visible under certain illumination and observation conditions suggests that the information contained in one image may be incomplete for inspection purposes. Thus, the use of image series would be beneficial, in the sense that it provides complementary information of a scene. In [1] and [2] the principles of an image series acquisition system with variable illumination are presented. The challenge arising with the use of image series is how to fuse the distributed information. Previous work done in this area includes model-based and statistical methods. For example, some methods belonging to the first group are described in [1] and [2]. In the first case, the models of the defects consist of mathematical functions parametrized by the defect shape and the illumination direction. These functions are correlated with the corresponding images of the series. The correlation results are finally fused and thresholded. The second method takes into account a reflective model of a surface. The reflection properties and parameters, which are used to identify defective areas in a surface, are pixel-wise estimated from the intensity information distributed in the images of a series. In [3] a statistical method is presented. Statistical features based on a modified Local Binary Pattern (LBP) are extracted from the image series, and then integrated over the Euclidean group in order to obtain invariant features against rotation and translation. Then, based on these invariant

features, the defects are classified by a Support Vector Machine (SVM).

A different approach to the problem of defect detection in textured surfaces are the filter-based methods [4]. These methods share a common characteristic, which is that they use filter banks to extract features from the images. Different types of filters are commonly used for this task, for example, wavelets [5] and Gabor functions [6]. The main drawback of these methods is that appropriate filter parameters, which should yield optimal results, have to be chosen manually. A way to overcome this issue is to use the ICA (Independent Component Analysis) as a mean for learning filters from the data [7]. This has the advantage that the ICA filters are adapted to the image characteristics to be inspected, which implies no manual selection of parameters. An extension of ICA for feature extraction from image series was described in [8].

In this work an ICA approach for defect detection based on image series is presented. The method makes use of the ICA generative model to separate the texture from defects. The presented algorithm gives as output a segmented defects image.

2 Image acquisition

It is important to choose an appropriate illumination setting to acquire images with good quality for the further processing. Different known illumination techniques could be used for this purpose, for example, diffuse light, directed light or structured illumination. In the diffuse case, the surface to be observed is homogeneously illuminated from all directions, while in the directed case, the light source is ideally spatially located at one point and the rays reach the surface in a parallel manner. Structured illumination implies the projection of different light patterns, e. g. grids, onto the surface. In this work, the directed light illumination technique is chosen, because it increases the local contrast of the defective areas in the images.

2.1 Topographical defects

The defects that will be considered in this work are of topographical nature. In Fig. 3.1 a scheme of this type of defect and how a defect affects the reflection direction of an incident light ray is shown.

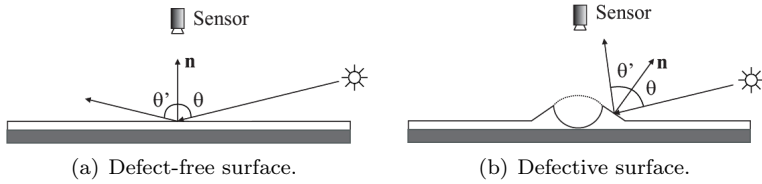


Figure 3.1: Scheme of a topographical defect.

Due to the partially reflecting properties of varnished surfaces, it can be assumed that the light rays hitting on a surface will be reflected as a superposition of a diffuse and a forescatter lobe [9]. As shown in Fig. 3.1, a defect causes a local change of the surface normal. As a varnished surface behaves partially like a mirror, the light reflected in a topographical defect will have a different direction than when hitting on a non-defective area. This property makes the use of directed light better suited than diffuse illumination, because a better contrast in the defective areas is achieved. In Fig. 3.2 an example of a varnishing defect (crater) under directional light with a varying illumination azimuth φ (see Fig. 3.3) is shown.

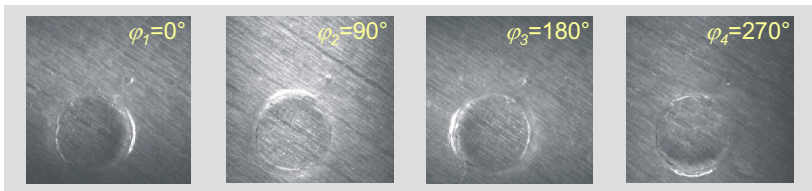


Figure 3.2: Defective surface under varying directional illumination.

2.2 Image series

In the previous figure, it can be noticed that good contrast is only partially achieved in each image. The complete defect cannot be easily identified in only one image. This suggests the need of using image series, in order to obtain sufficient information of the surface.

In Fig. 3.3 a scheme of an image series acquisition setup is shown. The

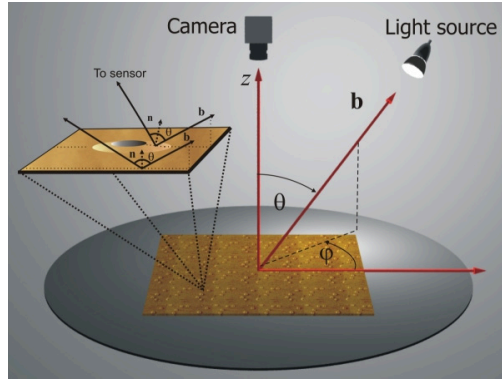


Figure 3.3: Scheme of a setup for acquisition of image series.

camera is fixed, viewing the surface perpendicularly from the setup's top. In this work, the image series are generated with fixed elevation angle θ and varying azimuth φ . The number of images included in each series considered in this work is $B = 4$, with $\varphi = 0^\circ, 90^\circ, 180^\circ, 270^\circ$ (see Fig. 3.4).

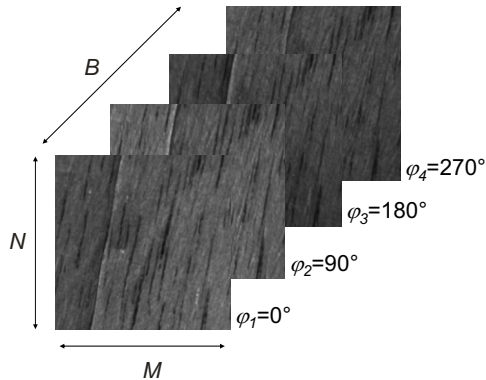


Figure 3.4: Graphical illustration of an image series. M : width, N : height, B : number of images.

From a mathematical point of view, an image series can be viewed as a vectorial function $\tilde{\mathbf{i}}(x, y)$ ³:

$$\tilde{\mathbf{i}}(x, y) = \begin{pmatrix} i^{(1)}(x, y) \\ i^{(2)}(x, y) \\ \vdots \\ i^{(B)}(x, y) \end{pmatrix}, \quad (3.1)$$

where B is the number of images of the series, (x, y) the spatial coordinates and $i^{(1)}(x, y)$, $i^{(2)}(x, y)$, \dots , $i^{(B)}(x, y)$ the individual images of the defined series.

3 Independent Component Analysis

Generally speaking, Independent Component Analysis (ICA) is a method that allows the separation of one or many multivariate signals into statistically independent components. A stochastic generative model serves as the starting point for the further analysis.

3.1 Generative model

The following generative model states that a number m of observed random variables can be expressed as a linear combination of n statistically independent stochastic variables:

$$\mathbf{x} = \mathbf{A} \cdot \mathbf{s} = \sum_i \mathbf{a}_i \cdot s_i, \quad (3.2)$$

where

- \mathbf{x} : observed vector ($m \times 1$),
- \mathbf{A} : mixing matrix ($m \times n$),
- \mathbf{s} : independent components vector ($n \times 1$),
- \mathbf{a}_i : basis vector ($m \times 1$),
- s_i : independent component ($s_i \in \mathbb{R}$).

³ In this contribution, an overscripted tilde, e. g. $\tilde{\mathbf{i}}(x, y)$, will denote an image vector (or image series).

The goal of the ICA is to find the independent components s_i of an observed vector:

$$\mathbf{s} = \mathbf{W} \cdot \mathbf{x}. \quad (3.3)$$

In the case that $m = n$, the transformation matrix $\mathbf{W} = \mathbf{A}^{-1}$. Note that the mixing matrix \mathbf{A} is not known a priori. Thus, \mathbf{A} and \mathbf{W} have to be estimated through the ICA of the observed data, too.

There is an ambiguity in the solution of the ICA problem, which is that the variance of the independent components cannot be unambiguously determined. To overcome this issue, it is simply assumed that the covariance matrix equals unity, i.e. $E\{\mathbf{s}\mathbf{s}^T\} = \mathbf{I}$ (it was assumed here that \mathbf{s} is zero-mean). An overview and description of different approaches and implementations of ICA algorithms can be found in [10].

3.2 Feature extraction

The calculation of an independent component s_i is achieved by means of the inner product of a row vector \mathbf{w}_i^T of the ICA matrix \mathbf{W} and an observed vector \mathbf{x} :

$$s_i = \langle \mathbf{w}_i, \mathbf{x} \rangle = \sum_{k=1}^m w_i^{(k)} \cdot x^{(k)}, \quad (3.4)$$

where $w_i^{(k)}$ and $x^{(k)}$ are the k -components of the vectors \mathbf{w}_i and \mathbf{x} respectively.

\mathbf{w}_i is usually called feature detector. In this sense, s_i can be understood as a feature of \mathbf{x} . However, in the literature, the concept of feature is not uniquely defined, and usually \mathbf{a}_i is denoted as feature, while s_i corresponds to the amplitude of the feature in \mathbf{x} . In this contribution, the concept of feature will be used for s_i and \mathbf{a}_i interchangeably.

3.3 Preprocessing

In this section, some preprocessing techniques usually associated with ICA algorithms that are also applied in our method are presented.

Removing of the DC component

It is usually assumed that the mean value of each realisation of the observed vector, also called the DC component, doesn't contain interesting information [11]. This applies to our problem, where the mean illumination level (or DC component) of an image does not give any useful information about a defect. Therefore, the DC component is removed (or subtracted) from the data.

Centering

A basic preprocessing step is to center the observed data \mathbf{x} , i.e. to subtract the mean vector $E\{\mathbf{x}\}$ from it, in order to obtain a zero-mean vector $\check{\mathbf{x}}$:

$$\check{\mathbf{x}} = \mathbf{x} - E\{\mathbf{x}\}. \quad (3.5)$$

For the sake of simplicity in the notation, in the following sections the observed vector \mathbf{x} is assumed to be zero-mean.

Note that the centering and the removing of the DC component don't are equivalent. The former implies the subtraction of the mean value of the vector \mathbf{x} from itself, considering each component as a random variable. Otherwise, the latter is performed by removing the mean value of each realisation of \mathbf{x} , so that $\sum_k x^{(k)} = 0$.

Whitening

Usually, ICA algorithms require 'whitened' or 'sphered' data as input. Whitening or sphering of data means to linearly transform a zero-mean vector \mathbf{x} :

$$\mathbf{v} = \mathbf{Q}\mathbf{x}, \quad (3.6)$$

in order to obtain a transformed observation vector \mathbf{v} , so that its covariance matrix equals unity:

$$E\{\mathbf{v}\mathbf{v}^T\} = \mathbf{I}. \quad (3.7)$$

After sphering, using Eq. (3.2), we can write:

$$\mathbf{v} = \mathbf{B}\mathbf{s}, \quad (3.8)$$

where $\mathbf{B} = \mathbf{Q}\mathbf{A}$ is an orthogonal matrix, because:

$$E\{\mathbf{v}\mathbf{v}^T\} = \mathbf{B}E\{\mathbf{s}\mathbf{s}^T\}\mathbf{B}^T = \mathbf{B}\mathbf{B}^T = \mathbf{I}. \quad (3.9)$$

In this way, the problem of finding an arbitrary matrix \mathbf{A} was simplified to the less demanding task of finding an orthogonal matrix \mathbf{B} . Many ICA algorithms make use of this simplification to solve the problem more efficiently. It is worth to mention that whitening of data is always possible. A standard method to perform sphering is the well-known Principal Component Analysis (PCA).

Dimension reduction

Additionally, the PCA can be used for dimension reduction of data, which in our case means to select a number n of independent components less than the number m of observed variables. This is achieved by retaining the n first principal components obtained from the PCA and discarding the rest. Normally, the most relevant information of the data \mathbf{x} is concentrated in the subspace spanned by the first principal components (those with the highest variance or energy). Thus, by reducing the dimension of the data space, irrelevant information can be neglected.

4 Extension of the ICA for image series

The generative model described in Eq. (3.2) can be extended and rewritten for image series as follows:

$$\tilde{\mathbf{i}}(x, y) = \begin{pmatrix} i^{(1)}(x, y) \\ i^{(2)}(x, y) \\ \vdots \\ i^{(B)}(x, y) \end{pmatrix} = \sum_{i=1}^n \begin{pmatrix} a_i^{(1)}(x, y) \\ a_i^{(2)}(x, y) \\ \vdots \\ a_i^{(B)}(x, y) \end{pmatrix} s_i = \sum_{i=1}^n \tilde{\mathbf{a}}_i(x, y) \cdot s_i. \quad (3.10)$$

The image series $\tilde{\mathbf{a}}_i(x, y)$, with $i = 1, \dots, n$, form an image series basis. With this basis an arbitrary $\tilde{\mathbf{i}}(x, y)$ can be generated if the appropriate weights s_i are used.

To perform the ICA, the data has to be presented in form of a column vector (see Eq. (3.2)). This is simply achieved by stacking all the pixels

of the image series in a vector \mathbf{i} . The specific order in which the pixels are arranged in the vector \mathbf{i} is irrelevant. So, we obtain:

$$\mathbf{i} = \sum_{i=1}^n \mathbf{a}_i \cdot s_i = \mathbf{A} \cdot \mathbf{s}. \quad (3.11)$$

Once the ICA was performed, the image series of the basis $\tilde{\mathbf{a}}_i(x, y)$ are formed from the column vectors \mathbf{a}_i of the mixing matrix \mathbf{A} rearranging the components of the vector in the corresponding position of the image series vector, i.e. the inverse procedure of the previously used vector stacking.

4.1 Feature extraction from image series

The feature detectors $\tilde{\mathbf{w}}_i(x, y)$ are also formed via the inverse stacking procedure of the row vectors \mathbf{w}_i^T of the ICA matrix \mathbf{W} . As shown in Eq. (3.4), the feature extraction is performed by means of the inner product of a feature detector and an observed vector. For the case of image series, the inner product is calculated through the summation of all pairwise multiplied pixels that have the same position in the image series:

$$s_i = \langle \tilde{\mathbf{w}}_i(x, y), \tilde{\mathbf{i}}(x, y) \rangle = \sum_{k=1}^B \sum_{x=1}^M \sum_{y=1}^N w_i^{(k)}(x, y) \cdot i^{(k)}(x, y). \quad (3.12)$$

4.2 Practical considerations

In order that the ICA estimation problem can be solved practically, the number of independent components n shouldn't be too large. n is normally chosen to be not greater than 256. For example, let us suppose that $m = n = 256$. For an image series, this means that the total number of pixels in the series is 256. If the number of images $B = 4$, then the size of each image has to be 8×8 pixels (because $4 \times 8 \times 8 = 256$). Images are usually much bigger than this, e.g. 512×512 pixels. However, this is not really a problem, because the ICA can be applied to small patches, instead of to the whole image. In this work, the number of images in the series and the image patches size will be $B = 4$ and 8×8 pixels respectively.

For purposes of visualisation, the image patches of a series are plotted contiguously in a rectangular arrangement. For example, the generative model described in Eq. (3.10) would take the schematic form shown in Fig. 3.5.

$$\begin{array}{|c|c|} \hline i^{(1)}(x,y) & i^{(3)}(x,y) \\ \hline i^{(2)}(x,y) & i^{(4)}(x,y) \\ \hline \end{array} = \begin{array}{|c|c|} \hline a_1^{(1)}(x,y) & a_1^{(3)}(x,y) \\ \hline a_1^{(2)}(x,y) & a_1^{(4)}(x,y) \\ \hline \end{array} \cdot s_1 + \dots + \begin{array}{|c|c|} \hline a_n^{(1)}(x,y) & a_n^{(3)}(x,y) \\ \hline a_n^{(2)}(x,y) & a_n^{(4)}(x,y) \\ \hline \end{array} \cdot s_n$$

$\bar{i}(x,y) \qquad \qquad \bar{a}_1(x,y) \qquad \qquad \bar{a}_n(x,y)$

Figure 3.5: Graphical representation of an image series patch generation.

5 Defect detection approach

In Fig. 3.6 a scheme of the proposed approach for defect detection in textured surfaces is shown.

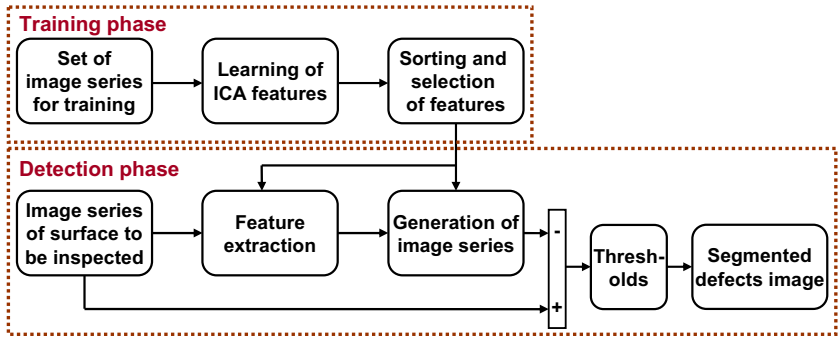


Figure 3.6: Scheme of the proposed defect detection approach.

The idea behind this approach is to separate the texture or background from the defects. This is achieved through the generation of an image series using only features that represent better the texture than the defects. These features are learned via the ICA from a set of training surfaces.

Then, the generated image series is subtracted from the original one. Finally, thresholds are applied in order to obtain a segmented defects image. In the following sections the method is explained in detail.

5.1 Learning of ICA features

The features (or basis vectors) are obtained from a set of selected image series that serve as training data. It is convenient that the set's surfaces include the types of defects wanted to be detected, because this yields a better characterization and separability of the features corresponding to the background and the defects. Image series patches are extracted from these training surfaces and then processed via an ICA algorithm, which gives as output the image series basis $\tilde{\mathbf{a}}_i(x, y)$, with $i = 1, \dots, n$, and the corresponding feature detectors $\tilde{\mathbf{w}}_i(x, y)$. Usually, for image data, a dimension reduction of 75% can be performed without a relevant loss of information [11]. In our case, this means that from the 256 pixels or components of the observed vector (image series patch), only the first 64 principal components are considered. As input for the ICA algorithm, 50000 image series patches taken from random positions of the training images set are used. As mentioned previously, the DC component is considered to contain irrelevant information, so it is removed from the input data, i.e. from each image series patch.

5.2 Sorting of features

Each feature learned by the ICA remarks different aspects of an image series. In particular, some of them will characterize better the texture or background than the defects. So, it is important to find a way to identify and quantify which of the features are better suited to describe the background. The following proposed function $m_i(\tilde{\mathbf{a}}_i)$ can be used as a measure for this purpose:

$$m_i(\tilde{\mathbf{a}}_i) = \sum_{x,y} |a_i^{(1)}(x, y) - a_i^{(2)}(x, y)| + |a_i^{(1)}(x, y) - a_i^{(3)}(x, y)| + \\ |a_i^{(1)}(x, y) - a_i^{(4)}(x, y)| + |a_i^{(2)}(x, y) - a_i^{(3)}(x, y)| + \\ |a_i^{(2)}(x, y) - a_i^{(4)}(x, y)| + |a_i^{(3)}(x, y) - a_i^{(4)}(x, y)|. \quad (3.13)$$

Basically, Eq. (3.13) gives a measure of the pixel intensity distribution similarity between the individual images $a_i^{(1, \dots, 4)}(x, y)$ of an image vector

$\tilde{\mathbf{a}}_i(x, y)$. A low value of $m_i(\tilde{\mathbf{a}}_i)$ denotes a high similarity. It is important to note that the DC component of the individual patches has to be also removed in this case, so that only the distribution of the intensities affects the measure. The image series of the basis $\tilde{\mathbf{a}}_i(x, y)$ are then sorted by this measure. The lower the value of $m_i(\tilde{\mathbf{a}}_i)$, the better describes $\tilde{\mathbf{a}}_i$ the background. That is because defects introduce local variations of the intensity distribution between the images of a series.

5.3 Defect segmentation

Once the features are sorted, the next step is to generate the image series of the surface to be inspected $\tilde{\mathbf{i}}_{\text{gen}}(x, y)$ by only using the first k sorted features ($k < n$). So, the generated images will reproduce principally the background, while the defects will be attenuated. k can be usually set to the half of the total number n of vectors that form the basis.

$$\tilde{\mathbf{i}}_{\text{gen}}(x, y) = \begin{pmatrix} i_{\text{gen}}^{(1)}(x, y) \\ i_{\text{gen}}^{(2)}(x, y) \\ i_{\text{gen}}^{(3)}(x, y) \\ i_{\text{gen}}^{(4)}(x, y) \end{pmatrix} = \sum_{i=1}^k \begin{pmatrix} a_i^{(1)}(x, y) \\ a_i^{(2)}(x, y) \\ a_i^{(3)}(x, y) \\ a_i^{(4)}(x, y) \end{pmatrix} s_i = \sum_{i=1}^k \tilde{\mathbf{a}}_i(x, y) \cdot s_i. \quad (3.14)$$

Whole images are simply obtained by generating contiguous image patches and then joining them together.

The segmented defects image is obtained following the thresholding scheme shown in Fig. 3.7. All the operations shown in this figure are performed in a pixel-wise manner. When the absolute value of the difference between an original image $i^{(1, \dots, 4)}(x, y)$ and the generated one $i_{\text{gen}}^{(1, \dots, 4)}(x, y)$ trespasses a threshold Thresh_a , then these areas are considered as possible defects. If these possible defective zones occur in the same position in at least Thresh_b different individual images of the series, then this area is considered as defective. Note that if $\text{Thresh}_b = 1$, then all possible defects would be actually considered as defects.

5.4 Example with a simulated image series

In order to show exemplarily how to carry out the different steps of the described method, the complete procedure, from the training phase to

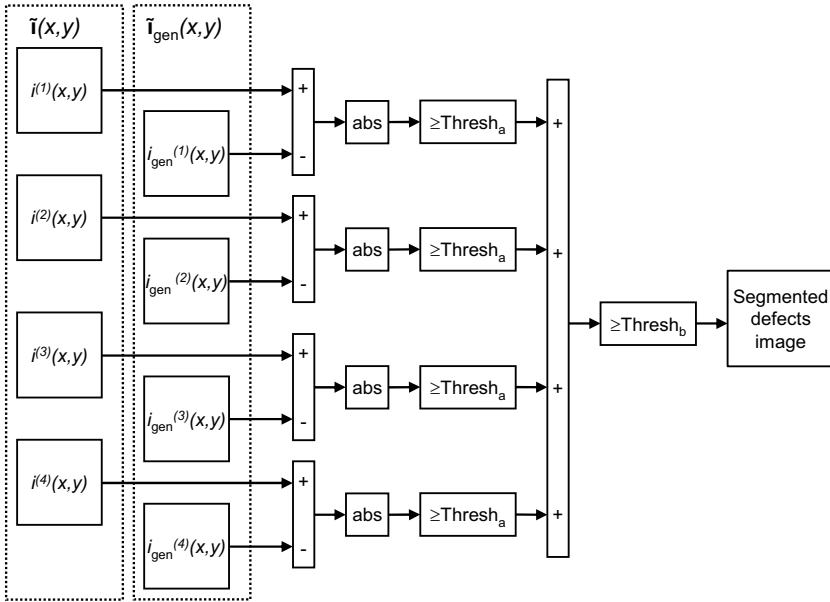
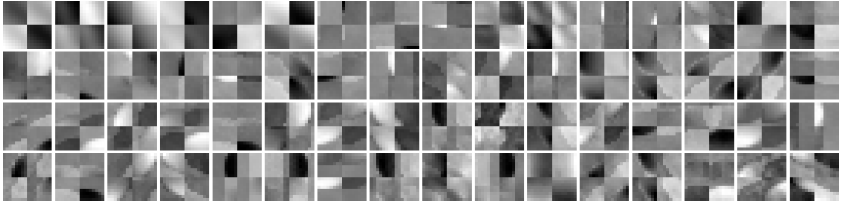


Figure 3.7: Scheme of the segmentation method.

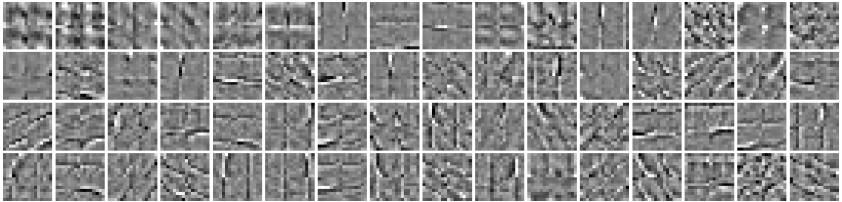
the defect segmentation, is applied to a simulated image series, which was generated using the POV-Ray ray tracing program. The simulated wood surface includes a crater as defect (see Fig. 3.9 (a)-(d)).

Training phase

The feature detectors are learned by applying an ICA algorithm (in particular, the FastICA algorithm [12] was used) to a set of 50000 image series patches taken from random positions of the simulated surface. Via the PCA, a dimension reduction of 75% is performed. Thus, the number of basis vectors to be estimated is $n = 64$. In Fig. 3.8 the learned image series basis and the feature detectors, sorted ascendingly by the measure described in Eq. 3.13, are shown.



(a) Image basis.



(b) Feature detectors.

Figure 3.8: Learned ICA features from a simulated surface.

Image series generation

For the image generation step, the first half of the sorted features is used, i.e. $k = n/2 = 32$. First, the independent components s_i of contiguous patches in the whole image are calculated through Eq. (3.12). Then, image series of the surface are generated using the generative model (Eq. (3.14)) with the calculated components s_i .

As shown in Fig. 3.9, the generated and the original images are practically identical in the non-defective areas, while the defect (crater) was not well reproduced in the generated image. This is because the features that better describe the defects ($k > n/2$) were not taken into account for the image generation. The DC component of the generated image patches was included in the plotted images just for purposes of visualisation.

Fig. 3.10 shows the absolute value of the difference between the original images and the generated ones. It can be seen that the difference is only significant in the defective zone. This means that the first half of the sorted features is able to describe well the texture, but not the defect.

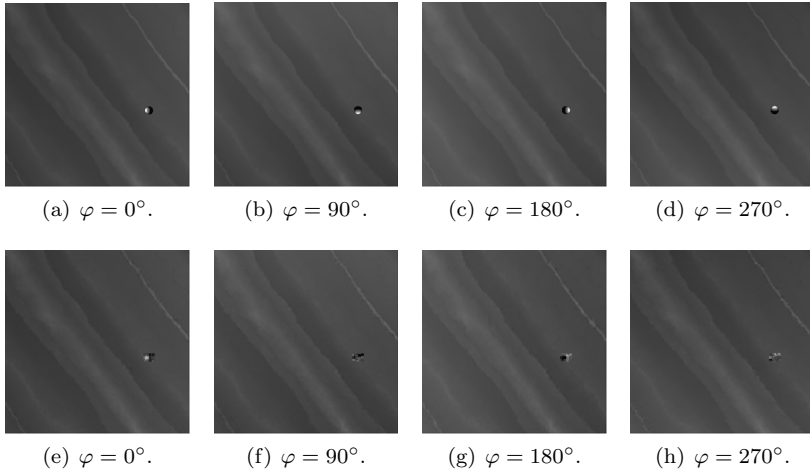


Figure 3.9: Image series of a simulated surface. (a)–(d): Original images. (e)–(h): Generated images.

Image segmentation

The defect segmentation results are shown in Fig. 3.11. First, each difference image are thresholded by Thresh_a (in this example $\text{Thresh}_a = 30$). Each pixel, where the difference exceeds the threshold, is considered as a possible defect. Fig. 3.11(a) shows the sum of the thresholded images. Finally, the summed image is thresholded again, in this example $\text{Thresh}_b = 2$, i.e. that a pixel needs to have at least two coincidences of possible defects to be considered as part of a defect.

The segmented defects image of the example with a simulated surface is shown in Fig. 3.11(b). In the next section, the same method is applied to an image series of a real wood piece.

6 Experimental results

The proposed defect detection method was also tested with varnished wood surfaces. The results are discussed in the following sections.

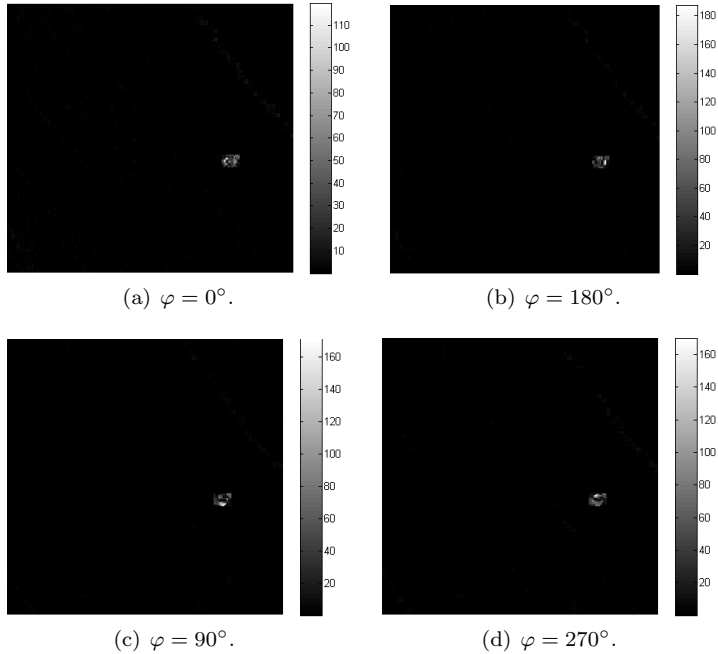


Figure 3.10: Absolute value of the difference between $\tilde{\mathbf{i}}(x, y)$ and $\tilde{\mathbf{i}}_{\text{gen}}(x, y)$.

6.1 Image basis and feature detectors

The results of the ICA algorithm applied to a set of training image series are shown in Fig. 3.12. Again, the dimension of the data space was reduced 75% through PCA, so that the number of feature detectors and basis vectors is $n = 64$.

The image series of the tested surface and the corresponding generated image series, using only the first half of the sorted features ($k = n/2$), are shown in Fig. 3.13. As in the previous example, the DC component of the image patches was included in the generated images, just for visualisation purposes.

The tested surface contains two fissures, in the upper and in the lower part respectively. The generated images reproduce very well the original

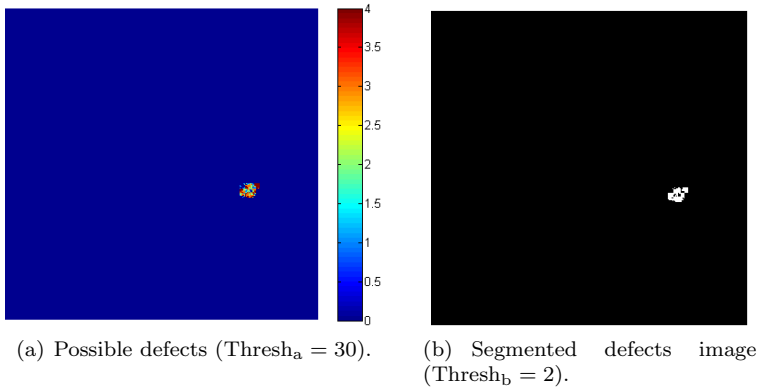


Figure 3.11: Possible defective areas and segmented defects image of a simulated surface.

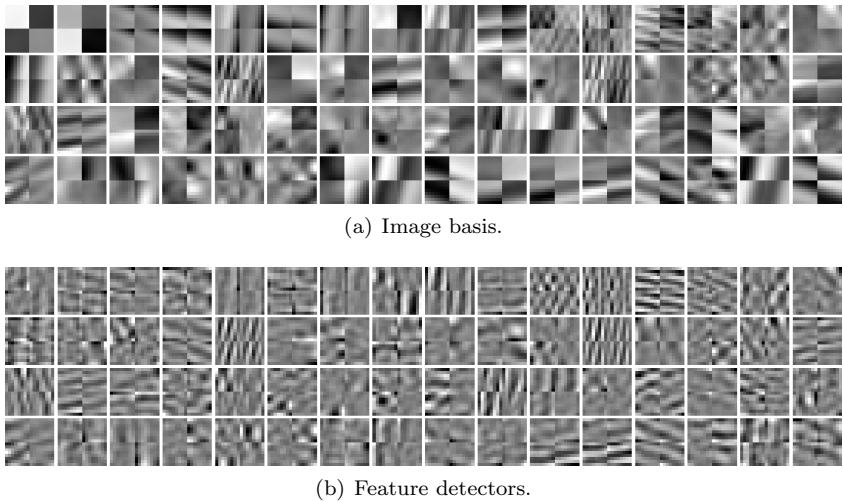


Figure 3.12: Learned ICA features from textured wood.

surface in the zones with no defects. On the contrary, the defective areas are attenuated and not clearly identifiable in these images. As noted

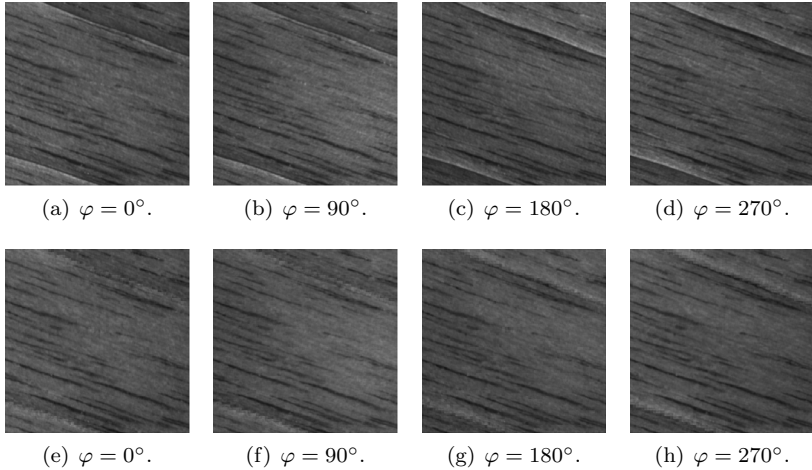


Figure 3.13: Image series of a tested surface. (a)-(d): Original images. (e)-(h): Generated images.

before, this is because the features, which better describe the defects, were not taken into account in the generation process.

6.2 Defect segmentation

The image indicating the possible defects and the final segmented defects image, obtained following the thresholding scheme of Fig. 3.7, are shown in Fig. 3.14.

7 Summary

A method for defect detection in textured surfaces was presented. The method relies on the analysis and fusion of image series with variable illumination. This image acquisition and illumination technique provides a better visualisation of topographical defects than a single image of a surface. The proposed method can be considered as filter-based, where the filters (or feature detectors) are learned by the ICA from a set of training surfaces. The learning of features has the advantage that no parameters

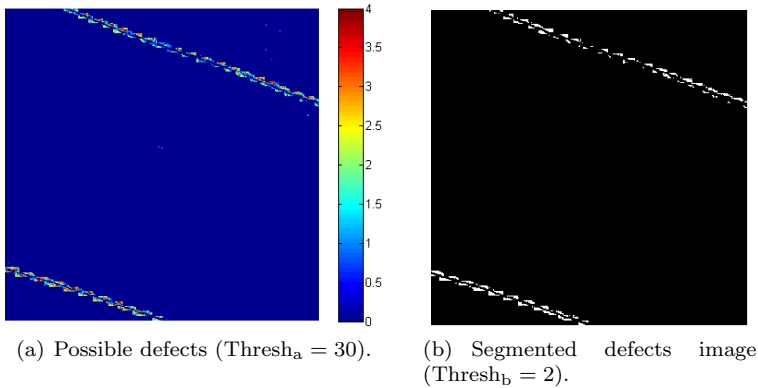


Figure 3.14: Possible defective areas and segmented defects image of a varnished wood surface.

have to be selected or tuned manually. Through a stochastic generative model, on which the ICA model relies, ‘filtered’ images are generated. In these images the defect’s information is attenuated, while the background or texture is well reproduced. Then, the differences between the original images of a series and the generated ones are calculated. By use of a thresholding scheme, a segmented defects image is extracted. It is important to note, that the defect detection in textured surfaces presents a difficult task, due to the noisy background that introduces the texture itself. The method was tested on a defective varnished wood surface, showing good results.

Acknowledgment

The authors would like to thank AIDIMA, Spain, for the provision of wood specimens. This work was partially financed by the Government of Spain in the context of the VAMAD project.

References

1. A. Pérez Grassi, M. Abián Pérez, and F. Puente León, "Illumination and model-based detection of finishing defects," in *Reports on Distributed Measurement Systems*, F. Puente, Ed. Shaker Verlag, 2008, pp. 31–51.
2. C. Lindner and F. Puente León, "Segmentierung strukturierter Oberflächen mittels variabler Beleuchtung," *Technisches Messen*, vol. 73, no. 4, pp. 200–207, 2006.
3. A. Pérez Grassi and F. Puente León, "Invariant features from series of images to detect and classify varnish defects," in *Reports on Distributed Measurement Systems*, F. Puente, Ed. Shaker Verlag, 2008, pp. 53–67.
4. X. Xie, "A review of recent advances in surface defect detection using texture analysis techniques," *Electronic Letters on Computer Vision and Image Analysis*, vol. 7, no. 3, pp. 1–22, 2008.
5. G. Lambert and F. Bock, "Wavelet methods for texture defect detection," in *ICIP '97: Proceedings of the 1997 International Conference on Image Processing (ICIP '97) 3-Volume Set-Volume 3*. Washington, DC, USA: IEEE Computer Society, 1997, p. 201.
6. D. M. Tsai and S. K. Wu, "Automated Surface Inspection Using Gabor Filters," *The International Journal of Advanced Manufacturing Technology*, vol. 16, no. 7, pp. 474–482, June 2000. [Online]. Available: <http://dx.doi.org/10.1007/s001700070055>
7. D.-M. Tsai, Y.-H. Tseng, S.-M. Chao, and C.-H. Yen, "Independent component analysis based filter design for defect detection in low-contrast textured images," in *ICPR '06: Proceedings of the 18th International Conference on Pattern Recognition*. Washington, DC, USA: IEEE Computer Society, 2006, pp. 231–234.
8. L. Nachtigall and F. Puente León, "Merkmalsextraktion aus Bildserien mittels der Independent Component Analyse," in *XXIII. Messtechnisches Symposium des Arbeitskreises der Hochschullehrer für Messtechnik e.V. (AHMT)*, G. Goch, Ed. Aachen: Shaker Verlag, 2009.
9. C. Lindner and F. Puente León, "Model-based segmentation of structured surfaces using illumination series," *IEEE Transactions on Instrumentation and Measurement*, vol. 56, no. 4, pp. 1340–1346, 2007.
10. A. Hyvärinen and E. Oja, "Independent component analysis: algorithms and applications," *Neural Netw.*, vol. 13, no. 4-5, pp. 411–430, 2000.
11. A. Hyvärinen, J. Hurri, and P. Hoyer, *Natural Image Statistics: A Probabilistic Approach to Early Computational Vision*. Springer, 2009.

12. A. Hyvärinen and E. Oja, "A Fast Fixed-Point Algorithm for Independent Component Analysis," *Neural Computation*, vol. 9, pp. 1483–1492, 1997.

Segmentation of defect edges on grooved surfaces using anisotropic diffusion

Limeng Wang

Karlsruhe Institute of Technology (KIT),
Institute of Industrial Information Technology (IIIT),
Hertzstr. 16, D-76187 Karlsruhe

Abstract Metal surface manufacturing is an important work stage for precise shape finishing and texture generation. Some regular tool marks, such as evenly distributed grooves with neat edges, concern the surface roughness and functionalities. In this paper we provide an explorative study to inspect defect edges on the groove texture. The grooves are modelled by a modified straight-translation-generated shape (MSTGS). Considering the difference from ideal model, adaptive anisotropic diffusion is used to suppress orientation fluctuations on the grooves. As a result grooves can be piecewise represented with consecutively consistent orientation whereas variable orientations are preserved on the defect edges. The diffusion coefficients are adaptively computed according to the location of the straight line segments. By shape analysis the collinear and parallel conditions are verified in orientation space for straight line detection. Iteratively performing diffusion filtering the curved defect edges can be segmented in the image. Our approach is tested for real honed textures. The segmentation results provide important benefits for the classification of defects and quality evaluation of grooves.

1 Introduction

Image analysis based approaches for quality control are extensively applied in the field of industrial production. Metal surface manufacturing is an important work stage for precise shape finishing and texture generation. Some regular tool marks, such as evenly distributed grooves with neat edges, concern the surface roughness and functionalities. The properties of grooved surfaces can be conveniently controlled by adjusting

the groove angles, groove distribution and the balance of groove sets. Inevitably the abrasive procedure gives rise to some undesired flaws, which incorporate cracks, small holes, sharp edges, smeared metal and so forth. They have to be corrected before the metal materials are worn off to the limit of the size tolerance. Thereby some reliable methodology for on-line measurement and inspection tends to be a solution for automating modern machines.

The related works for this task can be found in the literatures. The success of these methods attributes to the effective segmentation of the grooves from defected background under certain constraints. A spectral analysis based method is presented in [1]. Groove sets are characterized as several radial lines in the Fourier spectrum. Such signals can then be separated from spectrum to reconstruct groove texture. A progress is achieved in [2] with ridgelet transform. Grooves can be extracted with a compact representation in wavelet domain. Unfortunately these two methods suffer from the global view of image signals, so that they are not sensitive to the groove segments. For this reason the validation of the above mentioned methods is restricted to intact grooves. Other methods employing the local orientation features were introduced in [3]. A set of rotated windows compose a filter bank to detect the local maxima of orientation coherence, which can be derived from local variance, local gradients or local spectra. The shortcoming of this method is that the window size is fixed and thus can not adaptively match the random spatial scales of grooves. Nevertheless, we still follow the well-known model for groove texture and depict it intuitively as straight-translation generated shape (STGS), i.e. a one dimensional signal moves according to a straight trajectory. The generalization to some nonintact STGT is named as the modified STGS (MSTGS) in this context (see Fig. 4.1).

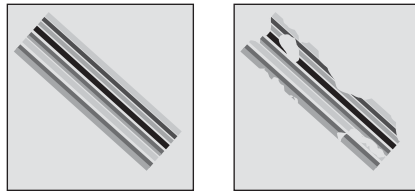


Figure 4.1: From left to right: (a) STGS (b) modified STGS.

Straightforwardly we assume the MSTGS as featured with irregular boundaries and consecutively consistent orientation in its inner parts. We have also noted that real manufactured grooves have random but similar local orientations, although visually they are regarded as straight lines. The disparities between human sense and computational analysis are invoked by the following facts:

1. Tiny fluctuations on the grooves can not be ignored. Typically they appear on the groove edges.
2. The imaging system digitalizes the scene in grids so that no ideal smooth lines exist any more.
3. Computational errors are introduced by the estimation of local orientation.
4. Noise from imaging equipment leads to some angle aberration.

In this case defects and grooves are obviously confused in feature space. Our work aims at searching grooves from complex image structures. It corresponds to determining the boundaries of MSTGS. Simultaneously the inner structural fluctuations of grooves should be suppressed in the digital picture to avoid false detections. Some means are exploited to stepwise realize image segmentation. To address point 4 the edge enhanced nonlinear diffusion is firstly used for denoising and preserving image structures. Afterwards the image is divided into oriented and nonoriented regions by edge detection. The oriented regions incorporate the boundaries and the inside straight edges of MSTGS. The nonoriented regions are flat surfaces and weak textures. We estimate local orientations in gradient field and merge them into several orientation bins. With that the angle errors of points 2 and 3 can be partially neglected. Anisotropic diffusion filtering is then performed to suppress orientation fluctuations mentioned in point 1. In this phase an eigenvalue analysis based method for straight line detection is used to assign the diffusion coefficients adaptively. The diffusion procedure is equivalent to repeatedly Gaussian low-pass filtering along a designated direction. Here we point out that MSTG boundaries show as macrostructure whereas the fluctuations inside MSTGS have large frequencies. By iterations the straight lines will be smoothed in gray levels and enhanced in orientation space with reduced angle difference. MSTGS boundaries will be preserved before the image structure is completely lost by smoothing. We organize

this paper as follows to detail our approach. Section 2 formally describes the MSTGS model and indicates the properties of grooves in orientation space. Section 3 reviews anisotropic diffusion briefly. Section 4 applies edge-enhanced diffusion to image denoising. In Section 5 we implement the algorithms for geometric-selective filtering. Section 6 presents some experimental results to verify the validation of our approach. Some conclusions are brought forward in Section 7.

2 The model of grooves

2.1 Representation in gradient vector field

The STGS model describes grooves as the spatial translation of a 1D function which is the profile of a groove set. The collinear points in STGS have constant luminosity intensity. The variation of luminosity intensity occurs perpendicularly to the direction in which the line stretches. Hence, grooves are modeled as a set of lines with various luminosity intensities. The grooves extend infinitely and are truncated by the image borders. Whether one point belongs to a straight line, is not only dependent on the relative position of the points, but relates to their local orientation. As defined in [4] the local orientation indicates the direction of maximal variation of luminosity intensity, i.e. the direction of the gradient vector of image intensity. Mathematically the MSTGS model is represented with vector geometry in polar coordinates. Fig. 4.2 illustrates the gauge coordinates (ξ, η) and the relationship of the gradient vector $\vec{I}(\vec{s})$, the coordinate vector \vec{s} and the vector of reference direction \vec{u}_k .

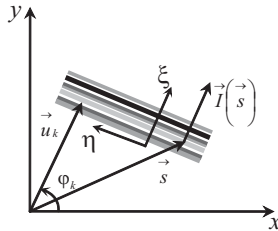


Figure 4.2: MSTGS model with vector geometry.

Two conditions are fulfilled in our model. They are written as the *collinear condition*,

$$\vec{s} \cdot \frac{\vec{u}_k}{|\vec{u}_k|} = |\vec{u}_k| \quad (4.1)$$

and the *parallel condition*,

$$\left| \frac{\vec{I}(\vec{s}) \cdot \vec{u}_k}{|\vec{u}_k| \cdot |\vec{I}(\vec{s})|} \right| = 1 \quad (4.2)$$

where $\vec{s} = x\vec{i} + y\vec{j}$ including the unit vectors of Cartesian coordinates, \vec{i} and \vec{j} , $\vec{u}_k = r_k e^{j\varphi_k}$ with its polar coordinates (r_k, φ_k) and $\vec{I}(\vec{s}) = \frac{\partial I}{\partial x}\vec{i} + \frac{\partial I}{\partial y}\vec{j} = |\vec{I}(\vec{s})| e^{j\theta(\vec{I}(\vec{s}))}$ for the input image I . $\varphi_k \in (-\pi/2, \pi/2]$, $\theta \in (-\pi/2, \pi/2]$, so that the vectors with opposite direction have a same orientation angle. We combine the collinear condition and the parallel condition to define a groove formally:

$$G_{m,k} = P_m \left(\vec{s} \cdot \frac{\vec{u}_k}{|\vec{u}_k|} - r_m \right) \cdot \delta \left(1 - \left| \frac{\vec{I}(\vec{s}) \cdot \vec{u}_k}{|\vec{u}_k| \cdot |\vec{I}(\vec{s})|} \right| \right) \quad (4.3)$$

$P_m(\cdot)$ denotes the profile of a groove. r_m is the translation of $P_m(\cdot)$ in 1D case. $\delta(\cdot)$ is the Dirac impulse function. The suffixes m and k denote the m -th groove in the k -th set of parallel grooves. In the next sections some strategies will be presented to apply this model in practice.

2.2 Decomposition in orientation space

The orientation space transform (OST) provides a method for multi-orientation analysis. The original definition of the orientation space (OS) in [5, 6] is a 3D space weighted by the responses of tuned Gabor filters. A simplified style of OS is applied here. In addition to the 2D Cartesian coordinates we set up the third dimension and define it as the angle of local orientation. We scatter the points into OS according to their orientation angles. Formally we give the orientation space:

$$OS(\vec{s}, \varphi) = \delta \left(1 - \left| \frac{\vec{I}(\vec{s}) \cdot \vec{u}(\varphi)}{|\vec{u}(\varphi)| \cdot |\vec{I}(\vec{s})|} \right| \right), \quad (4.4)$$

where $\vec{u}(\varphi)$ denotes a reference vector. Fig. 4.3 shows that the overlapping objects are separated on respective levels in OS. A straight line, regardless of its continuity, keeps on a single level. A planar curve is shattered on several levels. The components on each level fulfill the parallel condition.

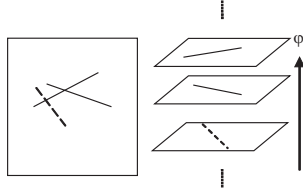


Figure 4.3: Separation of intersection lines in OS.

3 Anisotropic nonlinear diffusion

Anisotropic nonlinear diffusion (ANLD) can be understood as inhomogeneous blurring [7–9]. Consider the smooth filtering along the edges and across the edges. Since gradients are sensitive to noise, we estimate the local orientation with the structure tensor [4], which is the least-squares estimation of the gradient vector field in a pixel neighborhood:

$$\mathbf{S} = \begin{pmatrix} J_{11} & J_{12} \\ J_{21} & J_{22} \end{pmatrix}, \quad (4.5)$$

where $J_{11} = I_x^2 * W_\rho$, $J_{12} = (I_x \cdot I_y) * W_\rho$, $J_{22} = I_y^2 * W_\rho$. I_x and I_y are the image derivatives in x and y direction, W_ρ is a Gaussian window with the standard deviation ρ , and $*$ is the convolution operator. v_1 is the principal eigenvector of \mathbf{S} and is perpendicular to the edge, $v_2 \perp v_1$:

$$v_1 = (\cos \varphi \ \sin \varphi)^T, \quad (4.6)$$

$$v_2 = (-\sin \varphi \ \cos \varphi)^T, \quad (4.7)$$

where φ is the local orientation angle in $(-\pi/2, \pi/2]$:

$$\varphi = \frac{1}{2} \arctan \left(\frac{2J_{12}}{J_{22} - J_{11}} \right). \quad (4.8)$$

The diffusion equation is expressed as

$$\frac{\partial I}{\partial t} = \operatorname{div}(\mathbf{D} \bullet \nabla I), \quad (4.9)$$

where div is the divergence operator, ∇I is the image gradient vector and \mathbf{D} is the diffusion tensor:

$$\mathbf{D} = (v_1 \ v_2)^T \begin{pmatrix} u_1 & 0 \\ 0 & u_2 \end{pmatrix} (v_1 \ v_2) \quad (4.10)$$

with u_1 denoting the diffusion coefficient for v_1 and u_2 for v_2 .

4 Image preprocessing

As mentioned in Section 3, the image gradients are critically influenced by image noise. Therefore, the denoising method using ANLD is necessary for image preprocessing. The coefficients for edge-enhanced diffusion are given as follows:

$$u_1 = 1 - \exp\left(\frac{-C_m}{(|\nabla I|/K)^m}\right), \quad (4.11)$$

$$u_2 = 0.2. \quad (4.12)$$

As suggested in [9], $m = 8$ and $C_m = 3.31488$ are chosen. K is the diffusivity threshold. In this paper anisotropic nonlinear diffusion is implemented numerically with the standard AOS theme [9]. The decorrelation method described in [10] is utilized to select the stopping time. A test image of the texture H_0 and its denoising result are shown in Fig. 4.4. Throughout this paper all the test images are digitized with 512×512 pixels.

5 Algorithm for geometry-selective filtering

Practically there are flexible choices of the diffusion coefficients for applications [11]. Anisotropic diffusion in fact preserves desired edges during image smoothing. By edge-enhanced diffusion high contrasted edge can be blurred more slowly than low contrasted edges. The criterion is formulated with gradient magnitude for anisotropic blurring. Similarly

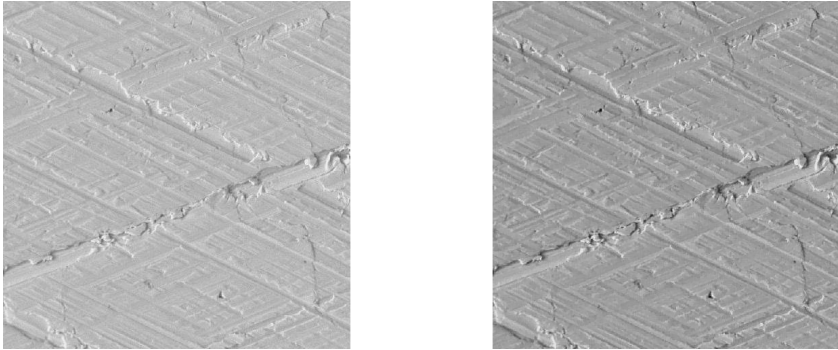


Figure 4.4: (a) Left: a test image of the honed surface H_0 (b) Right: edge-enhanced diffusion of H_0 .

we modify the diffusion coefficients on the basis of geometric features. Structural fluctuations on grooves arise from the microstructure of metal material and show larger frequency than curved defect edges. We accelerate blurring the straight edges once they satisfy collinear and parallel conditions. Otherwise edge-preserved diffusion is performed to restore the disturbed edges until their fragments acquire enough smoothness and evolve into consecutively consistent orientation. We implement this process by a diffusion procedure with adaptive diffusion coefficients, which rely on the locally detected segments of straight lines. An overview of our algorithm is depicted in Fig. 4.5.

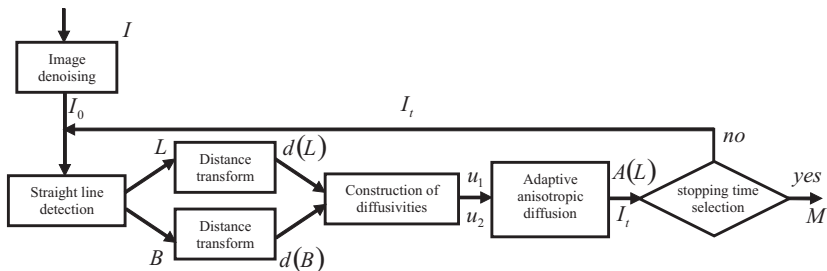


Figure 4.5: The work flow for the segmentation of defect edges.

5.1 Straight line detection

The operations for straight line detection are explained step by step as follows:

Step 1: Calculate the gradients by

$$I_x = I * g'_x, \quad (4.13)$$

$$I_y = I * g'_y, \quad (4.14)$$

where g'_x and g'_y are the derivatives of the Gaussian. Then the structure tensor \mathbf{S} is constructed in terms of Eq. (4.5) with the integration scale ρ . The eigenvectors v_1 and v_2 of \mathbf{S} are available in Eq. (4.6) and Eq. (4.7). The local orientation φ is the angle of the principle eigenvector v_1 .

Step 2: Threshold operation with T_e on gradient magnitude to determine a mask M of oriented and non-oriented regions,

$$M(x, y) = \begin{cases} 1 & (x, y) \in \{(x, y) \mid |\nabla I| > T_e\} \\ 0 & (x, y) \in \{(x, y) \mid |\nabla I| \leq T_e\} \end{cases} \quad (4.15)$$

Then the angles of oriented regions can be extracted from φ ,

$$\varphi_T = \varphi \cdot M \quad (4.16)$$

Step 3: For the numeric implementation of OST, φ_T must be quantified into finite bins. A linear uniform quantizer is constructed in (4.17).

$$Level(x, y) = \text{round} \left[\frac{N}{\pi} \left(\varphi_T(x, y) + \frac{\pi}{2} \right) + \frac{1}{2} \right] \quad (4.17)$$

The quantization interval $\Delta\varphi$ is π/N for N levels. Note that the angles are mapped to the integers from 1 to N , but the integer 0 is reserved to represent non-oriented regions. It is convenient to interpret the quantization result as level indices of the OS. Each pixel is labeled with its level index.

Step 4: On each level of OS the connectivity is analyzed with 8 neighbors [12]. The edges are separated in many connected components. The curved objects cross through many levels, but line-structured objects are concentrated on individual levels.

Step 5: It is reasonable to state that the small components on a single level likely belong to curved edges. So the area of each component is a measure for the consecutively consistent orientations. Only the large components are the candidates for straight line detection. Owing to the quantization some pixels with similar orientation are connected together on a single level and increase the component area. More complicated shape analysis should be involved to prevent the mixing of the curved components caused by rough angle resolution. Covariance matrix is exploited to compute similarity to a line-like shape [12,13]. In fact this step checks the collinear condition presented in Section 2. The binary component is understood as a function of two random variables, the coordinates x and y . Then the elements of covariance matrix $\mathbf{Cov} = \begin{pmatrix} C_{xx} & C_{xy} \\ C_{yx} & C_{yy} \end{pmatrix}$ can be calculated in (4.18) to (4.20)

$$C_{xx} = \frac{1}{n} \sum_{i=1}^n x_i^2 - m_x^2 \quad (4.18)$$

$$C_{yy} = \frac{1}{n} \sum_{i=1}^n y_i^2 - m_y^2 \quad (4.19)$$

$$C_{xy} = C_{yx} = \frac{1}{n} \sum_{i=1}^n x_i \cdot y_i - m_x \cdot m_y \quad (4.20)$$

A normalized measure of the linearity is formed in (4.21)

$$linearity = \left(\frac{(C_{yy} - C_{xx})^2 + 4C_{xy}^2}{C_{xx} + C_{yy}} \right)^2 \quad (4.21)$$

Only if linearity is large enough, the component can be detected as a straight line.

Step 6: Repeat the steps (4) and (5) for all the levels of the OS and combine the detected straight lines. The entire map of line structures is achieved by (4.22)

$$L = \bigcup_{i=1}^N L_i. \quad (4.22)$$

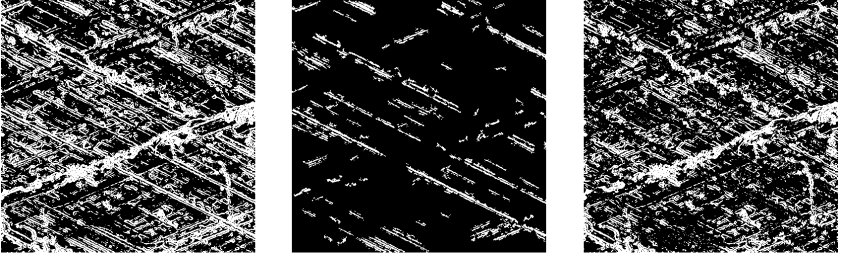


Figure 4.6: From left to right: (a) oriented regions (b) straight lines (c) defect edges. The results are achieved at the first iteration. The input image is H_0 .

Here L_i denotes the straight lines on a single level. The map of defects is $B = M - L$ (see Fig. 4.6).

5.2 Construction of diffusion coefficients

Our goal is to blur the edges of grooves but retain the edges of defects. If a pixel is close to grooves, it should be smoothed along v_1 . On the contrary, if a pixel is placed in the vicinity of defects, we smooth the image along v_2 . Therefore, u_1 and u_2 are assigned according to the distance transform [12] in L and B . The distance to the nearest point of straight edges is recorded for each pixel in d_L . In the same way the distance map d_B is derived from B (see Fig. 4.7). Consequently, u_1 and u_2 are defined as follows:

$$u_1 = \alpha + \beta \cdot \exp\left(\frac{-C_m}{(|\nabla I|/K)^m}\right), \quad (4.23)$$

$$u_2 = \beta, \quad (4.24)$$

where $\alpha = \frac{d_B}{d_L + d_B} \cdot \bar{M} + L$, $\beta = 1 - \alpha$ (see Fig. 4.8) This choice of u_1 and u_2 has the advantage to weaken blurring on the defect edges and simultaneously strengthen blurring on the groove edges.

5.3 Adaptive anisotropic diffusion

By iterations, u_1 and u_2 are updated in the filtered image I_t . The stopping time of the diffusion process is the moment, when the area of the

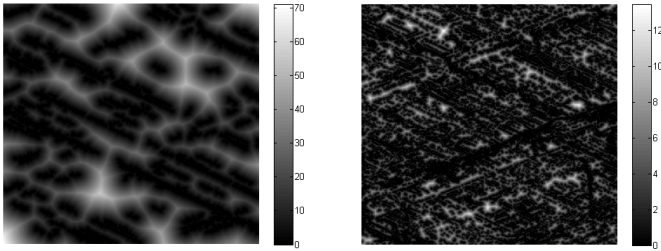


Figure 4.7: (a) Left: distance transform of L (b) Right: distance transform of B . The results are achieved at the first iteration. The input image is H_0 .

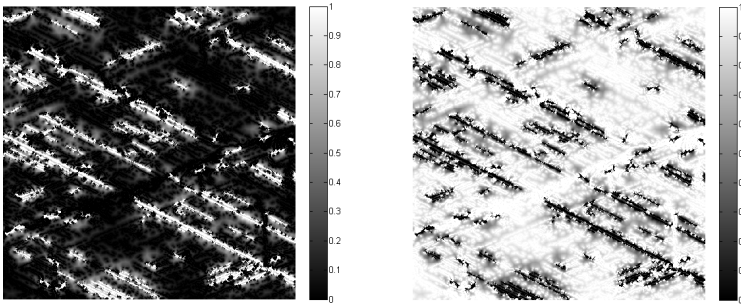


Figure 4.8: (a) Left: α (b) Right: β . The results are achieved at the first iteration. The input image is H_0 .

detected straight lines A_L turns very small. This time the residual components in L have also great uncertainty to be straight line. Thus, we choose M as the final result of the segmentation. The defect edges are extracted by $E = I \cdot M$. The segmentation results provide important benefits for the further classification of defects and quality evaluation of grooves.

6 Experimental results

Honing is a mechanical procedure to manufacture precision bores. The typical application is the finishing of cylinders for internal combustion

engines. Honed surfaces are featured with two cross-hatches in a certain angle. The microscopic images of honed surfaces and some important processing results are displayed in Figs. 4.12, 4.13 and 4.14 . Various disturbances can be found, such as flakes (H_1, H_2), cracks (H_1, H_2, H_3), holes (H_3), material defects (H_1, H_2, H_3), groove interrupts (H_1, H_2, H_3) and chatter marks (H_1, H_2).

Table 4.1: Parameter settings.

Parameters for image denoising	
K	$mean(\nabla I_t)$
τ_1	1
ϵ_1	0.05
Parameters for straight line detection	
T_e	$mean(\nabla I_t)$
W_ρ	$W_0 = \frac{1}{9} \begin{pmatrix} 1 & 1 & 1 \\ 1 & 1 & 1 \\ 1 & 1 & 1 \end{pmatrix}$
σ	1
N	10
T_a	50
T_s	0.8
Parameters for geometry-selective filtering	
τ_2	1
ϵ_2	0.1

In our tests we adjust the parameters to constant values according to Table 4.1. The evolution of edges will be automatically terminated according to some stopping criteria. Stopping time for image denoising is determined by decorrelation method [10]. Suppose the number of the current iteration i and step size τ_1 , compare the signal-noise correlation with each other. If $corr(I_t(0) - I_t((i-1) \cdot \tau_1), I_t((i-1) \cdot \tau_1)) - corr(I_t(0) - I_t(i \cdot \tau_1), I_t(i \cdot \tau_1)) < \epsilon_1$, the filtered image $I_t(i)$ is found with the stopping time $t_1 = i \cdot \tau_1$. Notice that signal-noise correlation doesn't reach the minimum in our approach, but only decreases nearly to the minimum in order to avoid excessive smoothing of relevant textures. Stopping time for geometric-selective filtering is one of the moments, when A_L reaches local minima. A_L is normalized with the entire image area. Practically A_L doesn't decrease monotonically but trends to

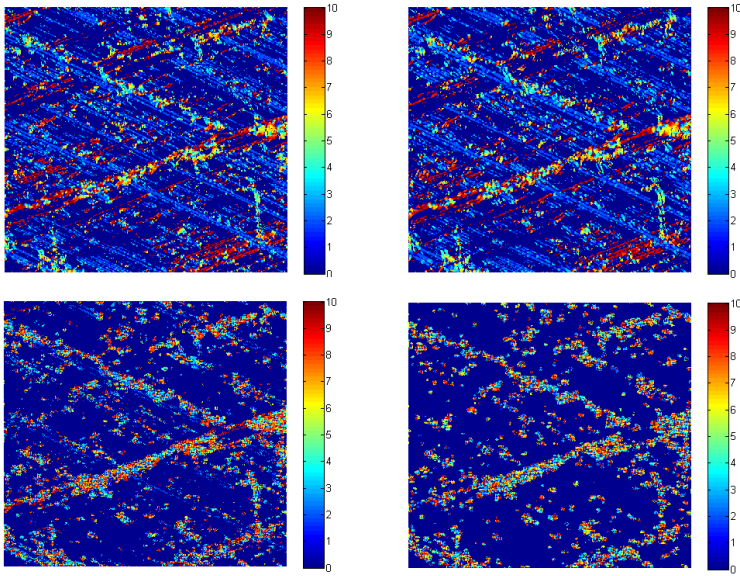


Figure 4.9: From upper left to lower right: diffusion results at iteration 0, 2, 4, 10. The parameters are set in Table 1. Jet color map is used to display the orientation level indices. The input image is H_0 .

fluctuate around a stable level. The stopping time should be selected at one of the local minima in the phase of the stable fluctuation. A question concerns how to know the stable fluctuation is arrived on the filtering procedure. A simple and effective trick is used, given the current and previous local minima of A_L ($A_{Lmin}(j)$ and $A_{Lmin}(j-1)$, respectively). If $|A_{Lmin}(j) - A_{Lmin}(j-1)| < \epsilon_2$, the filtering is terminated at $t_2 = (i+1) \cdot \tau_2$, where i is the iteration when the local minimum $A_{Lmin}(j)$ occurs. A plot of A_L for the texture H_0 illustrates the evolution procedure in Fig. 4.11. After 10 iterations the straight lines gradually disappear from the oriented region M . The segmentation is stabilized on defect edges. See also Figs. 4.9 and 4.10.

By the further test on H_1 the defects are dominant in the image so that only fine grooves are available. Since the residual metal piece and material smearing have irregular shapes, their curved edges are always

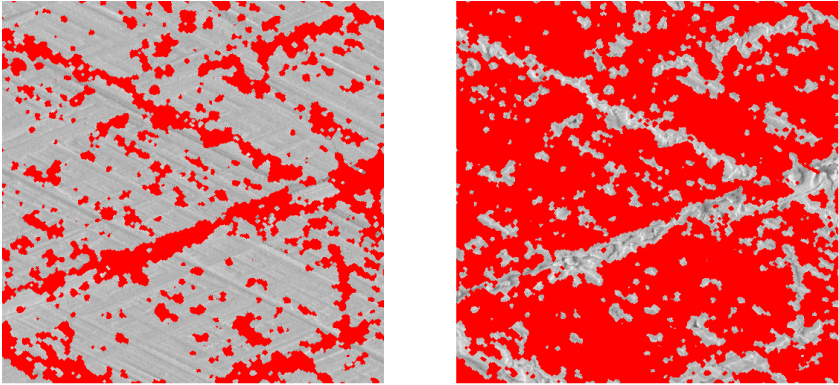


Figure 4.10: (a) Left: grooves and flat regions (b) Right: defect edges. The input image is H_0 .

smoothed weakly and still retained to the end . We cover the defect mask on the original image like Fig. 4.12(b), which contains the flat regions, inner parts of the residual metal piece and the grooved tool marks. Fig. 4.12(c) shows the defect edges.

Another test is performed on H_2 and shown in Fig. 4.13. Some closely neighbored thin lines are mixed with cracks and material defects. Moreover, the grooves with large width distribute somewhere on the surface. Since our algorithm concerns only the geometric properties of edges, the width of grooves has no effect on the result. From this point of view our method is robust regarding object scales. The flat regions inside the large defect will still be not segmented from input image.

The last test is accomplished with a weakly grooved surface in H_3 . Although the grooves can be recognized visually, the line structure is seriously interrupted so that there are seldom consistent local orientations on the grooves. Therefore, most part of the grooves is inspected as defects. The results are given in Fig. 4.14. The rest image contains only the flat regions and thus makes no sense. Nevertheless, the important tool marks can successfully be recognized and segmented in our tests.

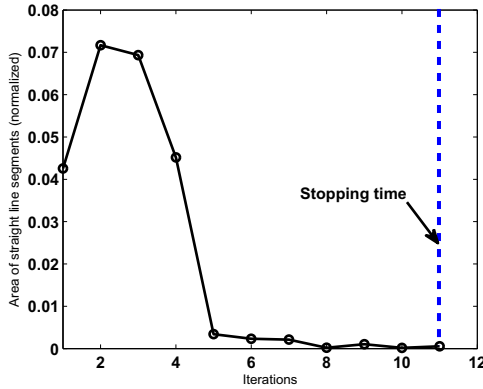


Figure 4.11: Automatic selection of stopping time. The input image is H_0 .

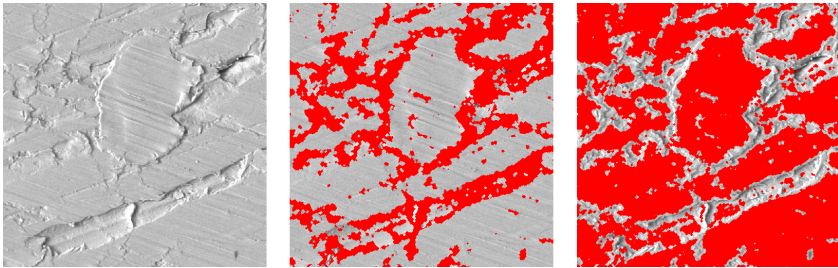


Figure 4.12: (a) H_1 ; (b) flat surface with fine texture; (c) defect edges.

7 Conclusion and outlook

Our method overcomes the drawbacks of the previous methods and shows feasible to inspect complicated engineering surfaces. For the computing efficiency it spends 0.5 to 1.6 s to process an image of 256×256 pixels in Matlab. The iterations for the geometry-selective filtering are 6 to 18 dependent on the amount of the straight lines in the image. To process a larger image it is possible to split it and do the operation in blocks. This way is more economical since each block demands different processing time and can be handled independently by parallel computing. Our

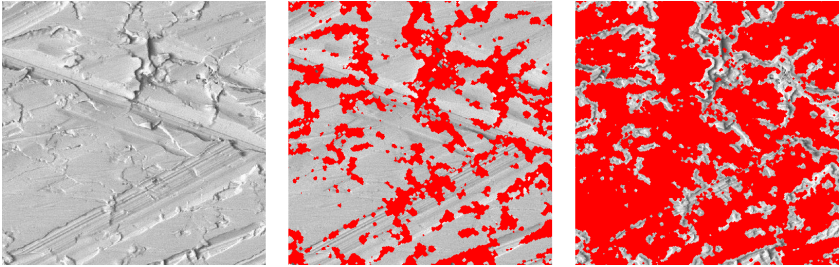


Figure 4.13: (a) H_2 ; (b) grooves and flat regions; (c) defect edges.

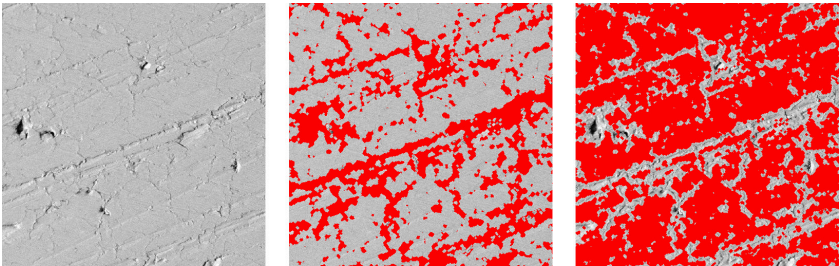


Figure 4.14: (a) H_3 ; (b) flat surface with fine texture; (c) defect edges and interrupted fine grooves.

future work will focus on improving the performance of this method and evaluating the properties of the groove texture.

References

1. J. Beyerer, “Analyse von Riefentexturen,” Ph.D. dissertation, Universität Karlsruhe, Karlsruhe, 1994.
2. B. Xin, “Auswertung und Charakterisierung dreidimensionaler Messdaten technischer Oberflächen mit Riefentexturen,” Ph.D. dissertation, Universität Karlsruhe, Karlsruhe, 2008.
3. M. Heizmann, “Auswertung von forensischen Riefenspuren mittels automatischer Sichtprüfung,” Ph.D. dissertation, Universität Karlsruhe, Karlsruhe, 2004.
4. B. Jähne, *Digitale Bildverarbeitung*. Springer, 2005.

5. M. V. Ginkel, "Image Analysis using Orientation Space," Ph.D. dissertation, Technische Universiteit Delft, Delft, 2002.
6. G. H. Granlund and H. Knutsson, *Signal processing for computer vision*. Dordrecht: Kluwer Acad. Publ., 2002.
7. B. M. ter Haar Romeny, "Introduction to scale-space Theory: Multiscale Geometric Image Analysis," in *4th. International Conference on Visualization in Biomedical Computing*, 1996.
8. —, *Geometry driven diffusion in computer vision*. Dordrecht: Kluwer Acad. Publ., 1994.
9. J. Weickert, *Anisotropic diffusion in image processing*. Stuttgart: B.G. Teubner, 1998.
10. P. Mrazek, "Nonlinear Diffusion for Image Filtering and Monotonicity Enhancement," Ph.D. dissertation, Czech Technical University, 2001.
11. M. Black, G. Sapiro, D. Marimont, and D. Heeger, "Robust Anisotropic Diffusion," *IEEE Transactions on image processing*, vol. 7, no. 3, 1998.
12. W. E. Snyder and Q. H., *Machine Vision*. Cambridge University Press, 2004.
13. D. S. Guru, B. H. Shekar, and P. Nagabhushan, "A simple and robust line detection algorithm based on small eigenvalue analysis," *Pattern Recognition Letters*, vol. 25, pp. 1–13, 2004.

Impulsive noise on the low voltage mains grid — detection method, parameter analysis and mitigation of its effects

Michael Bauer

Karlsruhe Institute of Technology (KIT),
Institute of Industrial Information Technology (IIIT),
Hertzstr. 16, D-76187 Karlsruhe

Abstract Impulsive noise constitutes the type of noise on the transmission channel for power line communication signals that is most difficult to analyze. Not only capturing impulsive noise during measurements is difficult, it is also very difficult to determine the effects different impulses might have on communication signals. In this paper, a method for extracting single pulses from measurement vectors is presented. The method is based on an analytically derived criterion. Furthermore, the method is validated and applied to a collection of measurements taken from several different locations. The impulses extracted by means of this method are then evaluated. Hypotheses explaining the origin of impulsive noise are given. Furthermore, it is shown that impulsive noise has more impact on some parts of the frequency bands of the A-band specified in CENELEC EN 50065 than on other parts.

1 Introduction

The fact that arbitrary equipment may be connected to the mains grid leads to a great variety of signals that are unintentionally injected into the mains grid. Commonly these kinds of noises do not affect the correct operation of electrical and electronic devices connected to the mains grid.

If the mains grid is to be utilized for carrying communication signals, however, such signals interfere with the actual communication signals, possibly resulting in bit errors.

Significant work has been conducted to analyze the properties of impulsive noise and to identify measurable parameters. Most prominent and exhaustive is the analysis provided e.g. in [1]. So far, the focus of the analysis of impulsive noise has been laid on its time-related parameters, i.e. the distribution of the interarrival times of impulsive noise, the time duration of single impulses, etc. However, when transmit signals are modulated by OFDM or other multi-carrier modulation schemes, the spectral properties of the impulses play a significant role. In particular, the questions to which extent the impulsive noise jam the communication signal and to which extent errors may actually be caused can only be answered by considering the impulses in the time/frequency plane [2].

It is worth to note here that the properties of impulsive noise strongly depend on the filter characteristics of the components it passes on its way from the coupling circuit to the demodulation and decision unit of an OFDM modem.

An extensive research on the characteristics of impulsive noise is provided in [1], where the parameters amplitude A , impulse time duration t_w and impulse arrival time t_{arr} have been identified. While [1] focuses on the time behavior of the impulses and develops a corresponding Markov model, this work focuses much more on the spectral properties of impulsive noise. Different coupling methods, a substantially different frequency range and thus a sampling frequency deviating to great extent from that used in [1] result in different findings concerning the parameters. Furthermore, the intention of this work is to provide a suitable definition of the term ‘impulsive noise’ that allows to differentiate it clearly from the other kinds of additive noise, i.e. background noise and narrowband noise. In addition to providing a clear definition, this will help to formulate a criterion for detecting the start and end of an impulsive noise waveform.

2 Field measurement setup and procedure

The measurement setup for capturing noise impulses is described in Figure 5.1. A digital storage oscilloscope (Tektronix TDS 3054B) is connected to the mains grid by means of a coupling circuit. Noise impulses are captured by utilizing the single shot function of the DSO. Capturing starts as soon as the voltage $u_M(t)$ exceeds a predefined trigger level, and

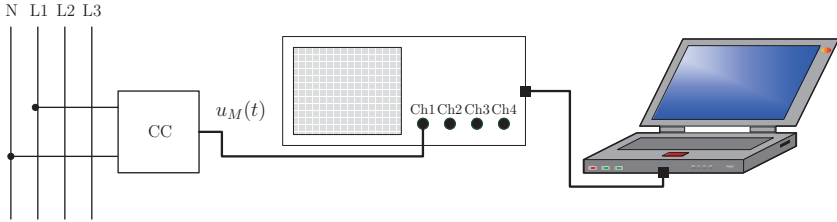


Figure 5.1: Setup for capturing impulsive noise.

stops as soon as the internal memory of the DSO is full. The captured signal is buffered to ensure that the waveform that caused the trigger event is placed inside the observation window, and the internal memory defines the length of the observation window. It is important to note that the memory depth of the DSO is only 10000 samples. Since the time resolution may be selected by the user, the sampling frequency has to be adjusted automatically to fulfill this limitation. During the measurement campaign a trade-off had to be found. On the one hand, the observation interval must be long enough to capture individual impulsive noise signals, on the other hand the sampling rate must be high enough so that the Nyquist frequency allows to analyze the spectral properties of the signals properly.

Since this measurement setup does not allow to observe the channel continuously for longer than a few milliseconds, it is impossible to provide a numerical value for the inter-arrival time of the observed impulsive noise waveforms. However, the inter-arrival times of impulses with large amplitudes have been observed qualitatively to be rather in the order of minutes than seconds for the measurement database considered in this paper.

Measurements have been conducted at the bus bar in different transformer substations and at house connection points in various locations in Karlsruhe, Germany, at various times of day. The locations included residential areas as well as industrial areas with medium-sized production facilities. All three phases L1, L2, and L3 have been included pairwise. Two phases have been observed simultaneously during a measurement session. In most cases, impulses occurred on both of the observed phases, whereas the impulse amplitude was considerably higher on one

Sampling rate (MSPS)	0.25	1	2.5	5
Recordings	8	9	20	26

Table 5.1: Recorded signal vectors and sampling rates.

of the phases compared to the other. Only the signal waveform of the impulse with the larger amplitude is considered for the further course of this study.

Measurements have been taken at different sampling rates, see Table 5.1.

3 Method for detecting impulsive noise

Prior to analyzing the properties of impulsive noise it is mandatory to identify impulsive noise waveforms in the measured sample vectors. It is necessary to devise a method that extracts reliably impulsive noise signals from measurement vectors containing background noise and possibly narrowband noise in addition to impulsive noise. The following section gives a brief overview of the properties of impulsive noise that will serve as a basis for the further analysis.

Impulsive noise properties

As derived in [3], the bit error probability depends on the signal power per bit (E_b) and the noise power (N_0) in the case of an AWGN channel model. In this case, the noise power spectral density is constant over time and frequency. The PLC transmission channel, however, cannot be modeled by such a model, because the noise power varies over time and frequency.

Aiming at a more detailed model for the noise power which would provide the basis for devising a precise statement of the channel capacity, it would be necessary to consider the noise power distribution in the time-frequency plane. Due to the uncertainty of time and frequency resolution, however, segmenting the different kinds of noise in the time-frequency plane would require sophisticated algorithms. This problem aggravates, if no a priori knowledge about the signal properties, i.e. information about the location along time and/or location along frequency dimension,

is available.

The parameters impulse amplitude A , impulse time duration t_w and impulse arrival time t_{arr} have been considered for an extended analysis in [1]. They are without any doubt important, because they provide information about the distribution of noise power in the time domain. Yet, this set of parameters does not allow to model the noise power distribution in the frequency domain, which would be equally important.

Therefore, a different approach is chosen in this work. In addition to determining the relevant parameters in the time domain, i.e. start and end points yielding the time duration t_w of an impulsive noise waveform and also its maximum amplitude A , the power spectral density (PSD) of impulsive noise waveform is considered for the relevant time interval.

3.1 PLC noise – characteristics in the time/frequency plane

As described e.g. in [4], the properties of the PLC channel are far from that of an AWGN channel. The channel transfer function causes (possibly) frequency-dependent attenuation that may be time-variant, but may be considered to be stationary for time periods that are long compared to commonly used OFDM symbol durations or even physical layer data units.

As described in [5], the noise signals observed on the mains grid can be modeled as a sum of different processes

$$n(t) = n_{BG}(t) + n_{NB}(t) + n_{Imp}(t). \quad (5.1)$$

The different classes of additive noise that affect the transmit signals in sum cause SNR values that vary over time as well as over frequency.

The amplitude of a narrowband interferer $\hat{n}_{NB}(t)$ is thus assumed to be constant in the time domain and its power spectral density (PSD) is localized well in a small region around a constant frequency. Similarly, amplitude values of background noise $\hat{n}_{BG}(t)$ are assumed to be low and distributed over a comparably small, fixed amplitude interval in the time domain. The PSD of background noise is also assumed to be constant, but is known to increase with decreasing frequency. Impulsive noise, however, exhibits highly dynamic amplitude values in the time domain with their modulus ranging from very low to very high values. The PSD is unknown, but assumed to be extended over wide parts of the frequency spectrum.

Noise Class	Noise power density over time	Noise power density over frequency
Background Noise	constant	constant
Narrowband Noise	slowly fluctuating	constant
Impulsive Noise	dynamically fluctuating	dynamically fluctuating

Table 5.2: Properties of the typical noise classes in the time-frequency plane.

Table 5.2 gives a qualitative overview of the power distribution of the noise classes in the time-frequency plane. Assuming that background noise and narrowband noise vary slowly over time, if at all, impulsive noise is to be considered as the main reason for the SNR to be dependent of time as well as frequency.

3.2 Impulsive noise segmentation algorithm

The need for a segmentation method providing a means to separate impulsive noise from other classes of noise has become clear from the previous sections. Considering the measured noise scenario $u_M(t)$ on the mains grid captured by a measurement setup similar to that in Figure 5.1, the previous section suggests that its power

$$P_M = \frac{1}{t_w} \int_0^{t_w} u_M^2(t) dt \quad (5.2)$$

could serve to derive a useful criterion for the segmentation.

For the following derivation, it is assumed that $|n_{BG}(t)|, |n_{NB}(t)| \ll 1$ V and $|n_{Imp}(t)| > |n_{BG}(t)|, |n_{Imp}(t)| > |n_{NB}(t)|$. Furthermore, the noise floor is stated by $|n_{BG}(t) + n_{NB}(t)|$. With these assumptions, it is justified to assume that the average time domain power in the presence of impulsive noise, i.e. if $u_M(t) = n(t)$,

$$P_{Imp,NB,BG} \approx \frac{1}{t_w} \int_0^{t_w} (n_{Imp}^2(t) + 2n_{Imp}(t)n_{BG}(t) + 2n_{Imp}(t)n_{NB}(t)) dt \quad (5.3)$$

is considerably higher than the average time domain power when impulsive noise is absent

$$P_{NB,BG} = \frac{1}{t_w} \int_0^{t_w} (n_{BG}(t) + n_{NB}(t))^2 dt. \quad (5.4)$$

However, since there is no a priori information about the time duration of impulses t_w , it is not advisable to use the average time domain power of the signal for detecting the start of an impulsive noise waveform. Instead, the instantaneous power

$$P^{inst}(t) = u_n(t)^2 \quad (5.5)$$

of the signal $s(t)$, assuming a 1Ω load, will be used in the further discussion.

Similar to the relation between the average powers in Equation 5.3 and Equation 5.4, respectively, the instantaneous power is low as long as no impulses are present, and high in the presence of impulsive noise, thus

$$P_{Imp,NB,BG}^{inst}(t) \gg P_{NB,BG}^{inst}(t). \quad (5.6)$$

Yet, there is no a priori knowledge of the impulse amplitude A , and it is thus impossible to introduce a limit for detecting the presence of an impulsive noise waveform. Assuming the noise floor stated by background and narrowband noise is constant within the observation period, $|n_{BG}(t) + n_{NB}(t)| < c$ and thus $P_{NB,BG}^{inst}(t) < c^2$, it is possible to use the first derivative of the instantaneous power

$$\frac{d}{dt} P_M^{inst}(t) = \frac{d}{dt} (u_M^2(t)),$$

since it is obvious that the instantaneous power of the observed signal will increase steeply as soon as an impulse occurs. The final decision criterion for detecting the start of an impulsive noise waveform can be obtained by introducing a constant limit k satisfying

$$\frac{d}{dt} P_M^{inst}(t) \begin{cases} \geq k & \text{if impulse waveform present} \\ < k & \text{if no impulse waveform present} \end{cases} \quad (5.7)$$

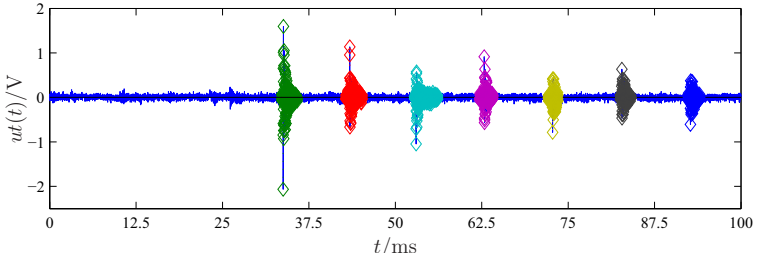
The start of an impulsive noise waveform t_S is thus marked by the point in time where $\frac{d}{dt}P_M^{inst}(t) \geq k$ and the end t_E by the point in time when $\frac{d}{dt}P_M^{inst}(t) < k$ after the threshold had been exceeded. Note that $t_S < t_E$ and $t_w = t_E - t_S$.

3.3 Evaluation of the segmentation method

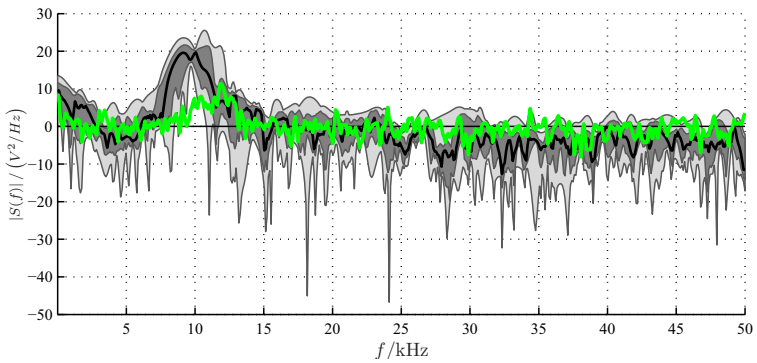
In this section, the validity of the segmentation method described in the previous section is demonstrated. All the figures are structured in the same way: the recorded time signal with highlighted impulsive noise waveform is shown as determined by the algorithm described in the above. The corresponding logarithmic PSDs are displayed in an extra figure, together with the mean PSD of the background noise. In case multiple impulsive noise waveforms are detected, the light gray areas represent the PSD values between the first up to 39th 40-quantile (i.e. the values between 2.5 and 97.5 per cent of the cumulative density function), the dark gray areas represent the PSD values between the first up to the 4th quartile (i.e. the values between 25 and 75 per cent of the cumulative density function). In addition, the median of the PSDs is represented by a solid black line.

Figure 5.2 illustrates the result of the segmentation algorithm in the time domain as well as in the frequency domain for a. Figure 5.2(a) shows the measured signals in the time domain with highlighted impulse segments, sampled at 100 kS. The remaining signal parts are considered to be background noise. Note that the impulse signal waveforms are segmented perfectly from the background noise. In this case, multiple impulse waveforms are detected. In order to obtain a good idea of the individual spectral components of the segmented signals, Figure 5.2(b) displays the PSD of the background noise and the PSDs of the impulsive noise waveform in a boxplot. The filled circles represent the median value of the PSDs of the individual waveforms for each of the frequency bins, the lower end of each vertical bar represents the 25th percentile, the upper end the 75th percentile.

Figure 5.3 shows a similar example. It differs from the signal in Figure 5.2 obviously regarding the waveform, but also in the sampling rate being considerably higher. The PSD is normalized so that it can be compared to the plot in Figure 5.2(b). For comparison, a third example is provided in Figure 5.4. The examples serve well to document two things that are



(a) Segmented impulse time signal with multiple impulses.

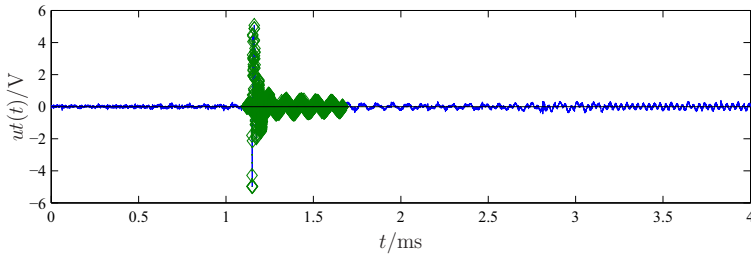


(b) Impulse signal PSD statistics and median background noise PSD over frequency.

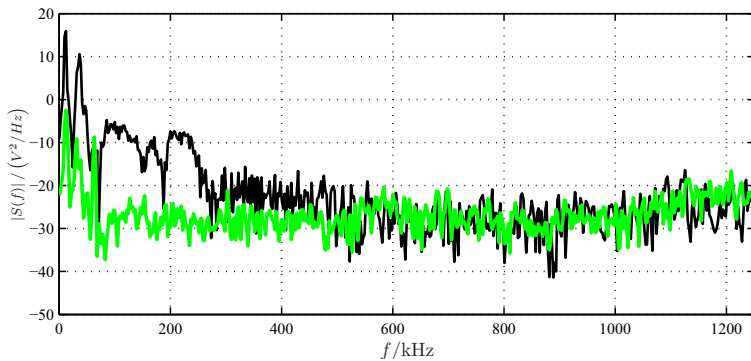
Figure 5.2: Segmented example impulse waveform recorded at 100 kS/s and corresponding spectra.

common to the vast majority of the recorded waveforms:

1. The PSD of the background noise increases towards lower frequency bands.
2. The PSDs of different impulsive noise signals have a maximum at approximately 12 kHz in common.
3. The PSD of the impulsive noise signals is concentrated in frequency bands below 600 kHz, even though there are steep gradients in the noise waveforms.
4. The PSD of the impulsive noise signals is considerably higher than



(a) Segmented impulse signal of a single impulse over time.



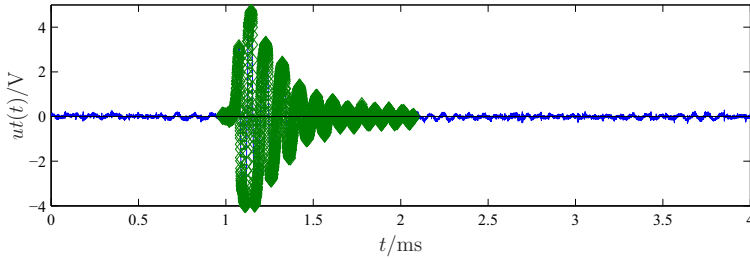
(b) Impulse signal PSD (black) and background noise PSD (green) over frequency.

Figure 5.3: Segmented example impulse waveform captured at 2.5 MS/s and corresponding spectra.

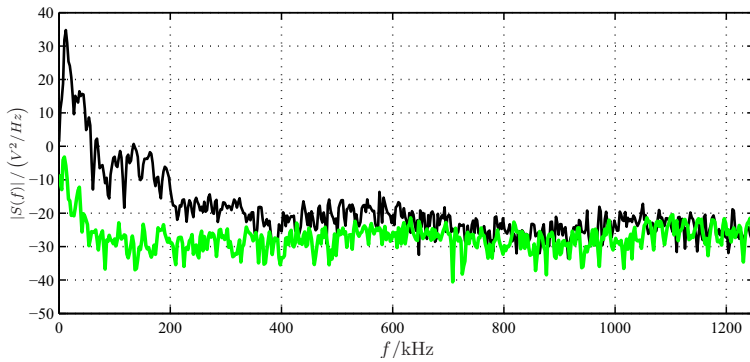
the PSD of the background noise in the frequency bands where it is located.

4 Analysis of the measured parameters of impulsive noise

In order to ensure the comparability of results, all captured waveforms have been re-sampled to a sampling rate of 333.3 kHz which is the same sampling rate as has been used in an OFDM-based communication system reference design described in [6]. Upon re-sampling, the signals are treated by the same method as described in subsection 3.2. As for the



(a) Segmented impulse signal over time.



(b) Impulse signal PSD (black) and background noise PSD (green) over frequency.)

Figure 5.4: Segmented example impulse waveform recorded at 2.5 MS/s and corresponding spectra.

communication system in [6], a 1024-point FFT is used in order to estimate the PSDs of the various signals. The resulting distribution of the PSDs of all impulsive noise signal waveforms and background noise fragments extracted from the measurement database are displayed in Figure 5.5. In principle, the representation is the same as described in subsection 3.3, but with outliers (PSD values outside the 3σ interval around the median value) marked by triangles. Note that all outliers are caused by higher PSD values.

In addition to the distribution of the PSDs of impulsive noise signals and background noise, the distributions of the durations of impul-

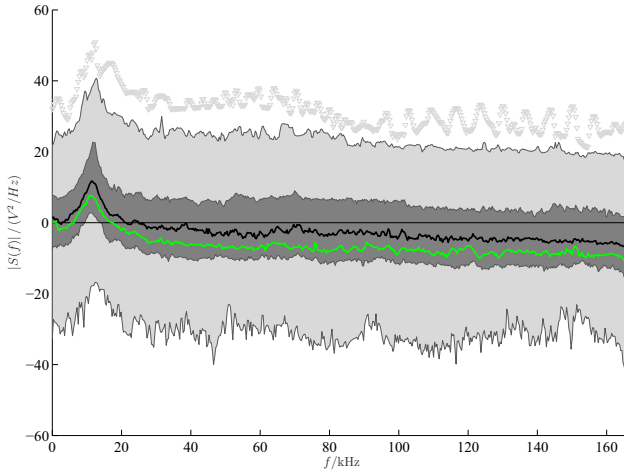


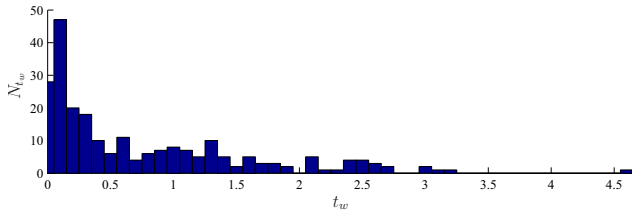
Figure 5.5: PSDs of impulsive noise waveforms and background noise.

sive noise waveforms $\hat{P}(t_w)$ is an interesting parameter that can be derived from the measurements, as well as the distribution of the maximum amplitude values for both, positive and negative signal voltage $\hat{P}(\max\{|n_{Imp}(t)|\})$. Both parameters are depicted in Figure 5.6.

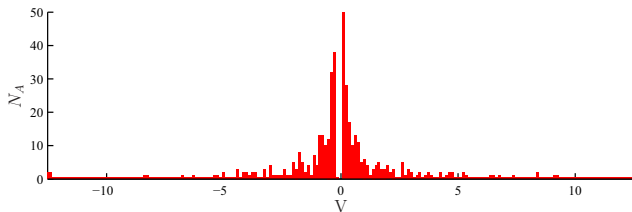
Figure 5.5 suggests that the PSD of impulsive noise can on average be characterized by a function that shows a maximum around 12 kHz, and is otherwise constant. This, however, may be due to the fact that the database for this statistical visualization consists of measurements that have been taken at different locations. The examples in subsection 3.3 suggest that the PSD of impulsive noise may at least in some cases depend on the location where they have been captured.

Figures 5.7 and 5.8 show that PSDs exhibit similarities even if measured at points that are spatially separated but belong to the same electrical network. The overall measurement results allow drawing the following conclusions:

1. **The PSDs of individual impulsive noise waveforms are clustered in different frequency bands, i.e. not all frequencies are affected by one impulsive noise waveform to the same amount.**



(a) Distribution of the duration of impulsive noise waveforms



(b) Maximum voltage peaks of impulsive noise waveforms (bipolar)

Figure 5.6: Distributions of relevant parameters of impulsive noise in the time domain.

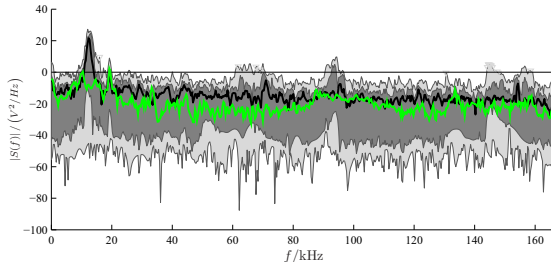
This is shown in figures 5.7(a) and 5.7(b).

If an impulsive noise waveform is short, it affects many frequency bins, but the noise power per frequency bin is comparably low and may be even below the noise power of the background noise.

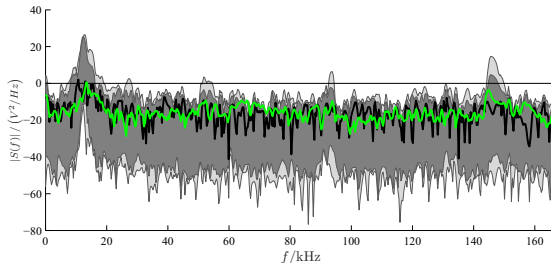
- The frequencies where impulsive noise power is clustered may depend on the electrical/physical properties of the network.**

To state a first hypothesis, the access impedance may play a role in combination with the properties of the coupling circuit.

- The duration of impulsive noise waveforms t_w is below 2 ms in most of the cases,** see Figure 5.6(a).
- Maximum amplitudes caused by impulsive noise may reach up to more than ± 10 V in extreme cases, ± 5 V are very likely to occur,**



(a) Inner city transformer substation busbar.



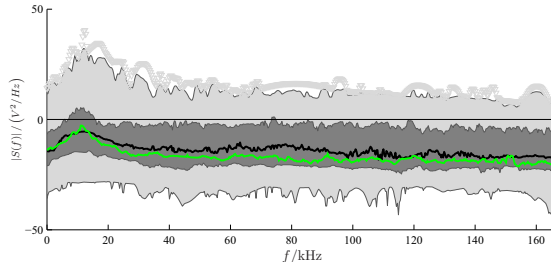
(b) House connection box connected to the same substation as in Figure 5.7(a).

Figure 5.7: PSDs of multiple impulsive noise waveforms captured at inner city transformer substation and house connection box .

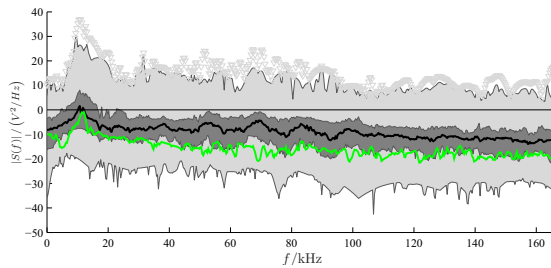
as can be seen from Figure 5.6(b).

Note that these conclusions can only be considered to be valid for the measurement setup depicted in Figure 5.1.

It is obvious that the PSDs of impulsive noise as well as of background noise show a large cluster of signal power around 12 kHz. The transfer function of the coupling circuit displayed in Figure 5.9 shows a resonance frequency at approximately 9 kHz, which obviously seems to cause this effect on the spectral properties of impulsive noise. Figure 5.9 yields that the resonant frequency of the coupling circuit is at 9 kHz, if the coupling circuit is terminated with a load of $1\text{ M}\Omega$. Assuming this terminating impedance is justified by the fact that the DSO used for the measurements has the same input impedance. The difference between



(a) Industrial area transformer substation busbar.



(b) Feeder connected to the busbar in Figure 5.8(a).

Figure 5.8: PSDs of multiple impulsive noise waveforms captured at industrial area transformer substation.

the measured resonant frequency of the coupling circuit of 9 kHz and the cluster of the noise PSD at 12 kHz may be caused by the access impedance of the mains grid.

4.1 Impulsive noise mitigation by pre-filtering

The measurement analysis in section 4 has shown that most of the impulsive noise signal power is concentrated in lower frequency bands, in particular around the resonant frequency of the coupler. Furthermore, it can be assumed that high noise signal amplitudes in the time domain represent the spectral components of the signal in higher frequency bands. In order to mitigate the effects of impulsive noise, applying a pre-filter to the receive signal may thus be advisable. In this experiment, a fourth order Butterworth bandpass filter is applied to the captured signals prior

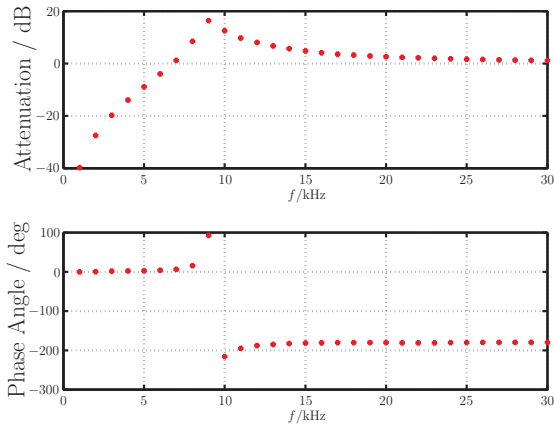


Figure 5.9: Modulus and argument of the transfer function of the coupling circuit.

to applying the detection algorithm to the filtered signals. The passband is equivalent to the frequency band used for transmission of the reference communication system in [6], i.e. the cutoff frequencies are 75 kHz and 100 kHz, respectively.

In fact, the filter attenuates the portions of both background noise and impulsive noise outside the passband, as shown in Figure 5.10. As expected, the distribution of the PSD in the passband does not change, the maximum still remains in the order of $10 \text{ dBV}^2/\text{Hz}$. Yet, the distribution of the time duration and maximum peak voltage in Figure 5.11(a) and Figure 5.11(b), respectively, are affected by the filter. The duration of individual impulses is now approximately 1 ms for most of the waveforms, which is shorter than in the case without pre-filter in Figure 5.6(a). The pre-filter proves to be most effective when the maximum amplitudes of impulsive noise – depicted in Figure 5.11(b) – are considered and compared to those in Figure 5.6. The maximum amplitude is between $\pm 2 \text{ V}$ when a pre-filter is used, compared to a maximum of up to more than $\pm 10 \text{ V}$ without pre-filter. This reduction is a major success, since it reduces the requirements of the analog/digital converter of the receiver, as

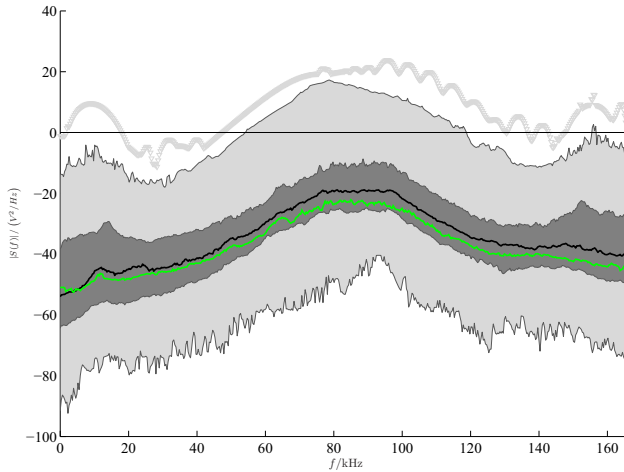
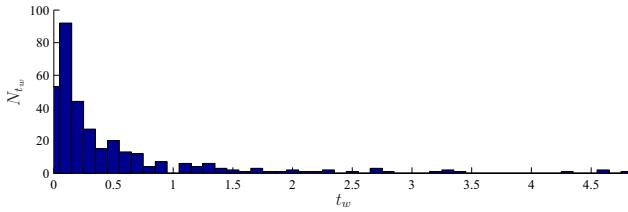


Figure 5.10: PSDs of impulsive noise waveforms and background noise of filtered signal.

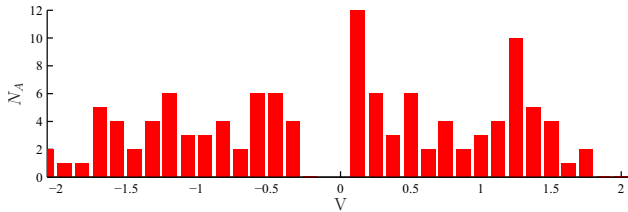
well as those of the automatic gain control.

5 Conclusion

In this study, the properties of impulsive noise in the low voltage grid have been analyzed. The analysis focused on the frequency range covered by CENELEC EN 50065 and thus likely to be used for future advanced metering and smart grid services over power line communication. Although the distribution of the PSD of impulsive noise captured at different locations shows no preferred frequency ranges in addition to a distinctive cluster around the resonant frequency of the coupling circuit, the PSD of an individual impulsive noise waveform may be higher in specific frequency bins than in others. This may possibly be caused by the physical properties of the mains grid, i.e. its access impedance, in combination with the properties of the coupling circuit, as a conjecture. Further research is necessary to clarify the possible interdependencies. As a final conclusion, it can be said that the dramatic impact of impulsive noise at the receiver of a communication system is considerably mitigated by in-



(a) Distribution of the duration of impulsive noise waveforms for filtered impulsive noise.



(b) Maximum voltage peaks of impulsive noise waveforms (bipolar) for filtered impulsive noise.

Figure 5.11: Distributions of parameters of impulsive noise resulting from filtered signals in the time domain.

cluding a pre-filter in the signal processing chain of a receiver by reducing the peak amplitudes caused by impulsive noise.

References

1. M. Zimmermann and K. Dostert, “Analysis and modeling of impulsive noise in broad-band powerline communications,” *IEEE Transactions on Electromagnetic Compatibility*, vol. 44, pp. 249–258, 2002.
2. G. Avril, M. Tlich, F. Moulin, A. Zeddami, and F. Nouvel, *Home Networking: First IFIP WG 6.2 Home Networking Conference (IHN’2007), Paris, France, December 10-12, 2007*, ser. IFIP International Federation for Information Processing. Springer, 2007, vol. 256/2008, ch. Time/Frequency Analysis of Impulsive Noise on Powerline Channels, pp. 143–150.
3. J. G. Proakis, *Digital communications*, 4th ed. Boston: McGraw-Hill, 2001.
4. M. Götz, M. Rapp, and K. Dostert, “Power line channel characteristics

and their effect on communication system design,” *IEEE Communications Magazine*, vol. 42, no. 4, pp. 78–86, Apr 2004.

5. J. Bausch, T. Kistner, A. Moreau, S. Sauvage, and S. Milanini, “Advanced ‘Orphelec’ test equipment and novel test procedures,” in *Int. Symp. on Power Line Communications and Its Applications*, April 2005, pp. 385–389.
6. T. Kistner, “Ein neuartiges mehrträgerbasiertes PLC-System mit störresistenter Synchronisation,” Ph.D. dissertation, Karlsruhe, 2008.

Countering impulsive noise without channel coding

Michael Bauer and Marco Kruse

Karlsruhe Institute of Technology (KIT),
Institute of Industrial Information Technology (IIIT),
Hertzstr. 16, D-76187 Karlsruhe

Abstract In power line communications (PLC), transmit signals are likely to be corrupted by high attenuation and additive noise. Among different kinds of additive noise, impulsive noise can be considered the most difficult to handle. Common approaches that aim at mitigating the effect of impulse noise on PLC transmit signals rely on channel coding techniques. In contrast to this common approach, we propose a new method for reducing the number of bit errors resulting from impulsive noise. The proposed method utilizes redundancy of transmit signals in combination with the properties of the Fourier transform rather than channel coding techniques. Depending on the choice of parameters, this method allows to reduce the number of bit errors even without necessarily increasing the gross bit rate.

1 Introduction

Power line communication (PLC) is often considered to be an economic solution for exchanging digital information. While utilizing the mains grid for data communication seems to be an economic advantage at first sight, the idea provides numerous technological challenges. The noise scenario inherent to the mains grid is known to have adverse effects on the quality of communication links. Numerous publications focusing on the analysis of impulsive noise are available, e.g. [1] and [2] for high-frequency, high-speed (broadband) communication and [3] for the case of low-speed, low-frequency communication. One of the most challenging kinds of additive noise is the class of aperiodic impulsive noise [1]: it appears at random points in time, lasts for a random duration, exhibits

random amplitude values and therefore random signal energy and has random spectral properties. Undoubtedly, the signal energy of aperiodic impulse noise is likely to be high compared to the transmit signal, even more so if the signal has experienced attenuation on its path from transmitter to receiver. Commonly, various methods of channel coding are applied in order to mitigate the effects of impulsive noise on data transmission by reducing the bit error rate, as described in [4] and [5]. Channel coding increases the overhead of binary information that has to be transmitted over an error-prone transmission channel by factors of at least two [4]. Moreover, developing efficient coding schemes is difficult and bit errors can still not be completely avoided by such measures. As long as PLC systems offer data rates in the order of Megabits per second, channel coding techniques provide a means to cope with impulsive noise in general. Despite the fact that code rates need to be rather high, overall latency times are acceptable for moderate applications, but deterministic behavior is still difficult to achieve. Regarding narrow-band PLC transmission, as it is intended to be used for smart grid applications in Europe, the situation is dramatically different. If a narrow-band PLC system complies with norms applicable within Europe [6], only gross data rates in the order of at most a few tens of Kilobit per second can be put into practice. This low gross data rates make it difficult to provide acceptable throughput even if the gross data rate could be used for useful bit information exclusively. Adding redundancy information as it would be necessary for channel coding techniques would aggravate the problem even further.

In this paper, we provide a first step toward solving this problem by extending the signal analysis capabilities of the DFT commonly utilized for OFDM transmit signal modulation and demodulation. The described method does not require redundant binary information, but rather relies on redundant signalling on the physical layer, thereby keeping the energy per bit constant. Signals only have to be repeated once. In special cases, it is even possible to maintain the data rate if improvements achieved by this method allow for increasing the number of bits per carrier.

The structure of the remaining paper is as follows: in Section 2 the basic signal properties used in this paper are introduced. Section 3 describes the properties of the narrow-band PLC transmission channel as well as the properties of an exemplary communication system. OFDM modulation by means of the DFT and the relation between DFT and

STFT are presented in Section 4. Section 5 describes how signal classification based on the signal parameters explained in Section 2 can be conducted. The resulting OFDM symbol reconstruction algorithm along with experiments for its validation are presented in Section 6.

2 General signal properties

In order to obtain objective criteria for differentiating between different signals, it is advantageous to define objective signal properties. The general parameters signal energy, the signal's average frequency and its bandwidth have proven to be useful criteria [7].

2.1 Signal energy

The signal energy E_x of a finite discrete signal x_n of length N is defined as

$$E_x = \|x_n\|^2 = \sum_{n=0}^{N-1} |x_n|^2 \quad (6.1)$$

$$= \|X_k\|^2 = \frac{1}{N-1} \sum_{k=0}^{N-1} |X_k|^2, \quad (6.2)$$

where X_k is the discrete Fourier transform of x_n .

2.2 Average frequency

The average frequency f_x of a signal x_n is given by

$$f_x = \frac{1}{E_x} \cdot \frac{1}{N} \sum_{k=-\frac{N}{2}+1}^{\frac{N}{2}-1} k \cdot |X_k|^2 \quad (6.3)$$

and can be interpreted as the mean of the spectral energy density of the signal. Since real-valued time signals have Hermitian symmetric spectra, it is obvious that their average frequency is always identical to zero. Therefore, the limits of the sum need to be changed taking into account

only positive frequencies, bearing in mind that this is only meaningful for signals that are real-valued in the time domain:

$$\tilde{f}_x = \frac{1}{E_x} \cdot \frac{2}{N} \sum_{k=0}^{\frac{N}{2}-1} k \cdot |X_k|^2. \quad (6.4)$$

With the limits set in this way, the result equals the computation of f_x for the analytic signal of x_n , except for a constant factor of 2.

2.3 Bandwidth

The bandwidth Δ_{f_x} of a signal x_n is defined by

$$\Delta_{f_x}^2 = \frac{1}{E_x} \cdot \frac{1}{N-1} \sum_{k=-\frac{N}{2}+1}^{\frac{N}{2}-1} (k - f_x)^2 \cdot |X_k|^2. \quad (6.5)$$

This can be interpreted as the standard deviation of the power spectral density of the signal. For real-valued time signals the summation limits are again restricted to one half of the spectrum:

$$\tilde{\Delta}_{f_x}^2 = \frac{1}{E_x} \cdot \frac{2}{N} \sum_{k=0}^{\frac{N}{2}-1} (k - \tilde{f}_x)^2 \cdot |X_k|^2 \quad (6.6)$$

2.4 OFDM signal properties for PSK

It is easy to show that the aforementioned signal properties are constants for phase-modulated OFDM symbols, because they only differ in the phase angle of the sub-carriers X_k . However, the phase angle does not influence the computation of the properties E_x , \tilde{f}_x , and $\tilde{\Delta}_{f_x}^2$, since they are all functions of $|X_k|^2$.

2.5 Impulsive noise signal properties – analysis of measurement results

Noise measurements on real power lines and their time-frequency analysis revealed that single noise impulses vary a lot in energy localization in

the time-frequency plane and thus in signal energy E_x , average frequency \tilde{f}_x and bandwidth $\Delta_{\tilde{f}_x}^2$.

Although classes of typical noise envelopes can be identified, a noise cancellation scheme that utilizes parameter estimation for mathematical models derived from these envelopes would not be feasible due to the large number of models and parameters. In addition, not modelled noise envelopes could render the whole scheme useless.

However, to conduct experiments, five parametric signal envelopes typical for impulse noise were constructed from a database of several hundred measurements. A sixth model to cover envelopes that do not fit the other five models has been implemented as colored noise with random energy, average frequency and bandwidth.

It should be pointed out that the durations of impulses were shorter than 1.5 ms in most of the cases.

3 Communications channel and system description

In this section, we provide a general overview of the communication environment provided by the mains grid at frequencies in the kHz range. Based on the knowledge gathered from literature and from measurements, we offer a simplified channel model that serves as a reference for evaluating the method proposed in Section 6. Furthermore, we describe the parameters of an exemplary OFDM-based narrowband PLC system.

3.1 PLC channel model

Numerous publications report the results of measurements for narrowband PLC in the low voltage grid. The measurements in [8] and [9] focus on the access domain between transformer station and residential buildings in the frequency range between 3 kHz and 95 kHz, the so-called A-band specified in [6]. [3] focuses on the in-house domain, extending the frequency range from 3 kHz to 500 kHz.

Channel transfer function

In the case of broadband PLC systems, the channel transfer function generally exhibits low-pass behavior [10]. In addition, it may feature frequency-selective behaviour (notching).

The behavior of the channel transfer function relevant to narrowband PLC systems contrasts the characteristics of broadband channel transfer functions in a sense that it exhibits less predictable characteristics. The amplitude response depends much more on the appliances connected to the grid than on grid topology. Taking into account the relation between the wavelength of the transmit signal and the cable lengths common for low voltage distribution grids, notches are much less likely. High attenuation has been reported to affect the transmit signal in many cases. In addition, low access impedances may cause unintentionally low transmit signal levels. For this study, it is assumed that frequency-selective effects caused by the channel transfer function can be neglected for narrowband PLC.

Narrowband interference

Narrowband interference is considered as additive noise signals with near-stationary power spectral densities that occur for time periods much longer than one OFDM symbol period. Although [8] reports narrowband interference in the access domain, we could find narrowband interference in only one out of eight locations that have been visited during a measurement campaign. This states a reason for assuming that narrowband interference plays only a minor role for narrowband PLC in the access domain. It is therefore not considered in the following parts of this work.

Impulsive noise

Each noise signal with a duration shorter than an OFDM symbol is considered as impulse noise. In addition, the power of impulse noise is supposed to be significantly higher than that of background noise and narrowband noise. Lacking more detailed knowledge, the appearances of single noise impulses are assumed to be statistically independent of each other. With this assumption the arrival times of these impulses can be modeled as a poisson process, which is a special case of a markov chain. The characteristic parameter of this model is the constant average arrival rate λ of the impulses.

Background noise

Noise signals that cannot be categorized in one of the classes described in the previous sections are modeled by a general stochastic process only described by its power spectral density. As described in [3], the power spectral density of the background noise exhibits the properties of colored noise, i.e. it increases with decreasing frequency. For the further parts of this work, we assume that the power spectral density of the background noise drops to power levels where it is possible for transmit signals to achieve agreeable SNRs at the receiver .

Channel model summary

Summarizing the findings laid out in the above sections, most of the admittedly unfavorable channel properties can be overcome by proper system design (see Section 3.2). The remaining issue is that it may be difficult to achieve optimum SNR levels at the receiver because of high channel attenuation. This aggravates the impact of impulsive noise on OFDM signals, even more so, as the signal energy of impulsive noise may be considerably higher than the actual OFDM signal level at the receiver.

3.2 Communication system parameters

Based on the knowledge outlined in Section 3.1, a communication system has been devised in [11]. Table 6.1 summarizes the parameters of this system. Note that the system is implemented as a baseband system, i.e. the transmitter generates the transmit signal from the output of the IFFT. At the receiver, the FFT operation is performed directly on the receive signal without any mixing stages.

Modulation scheme	D-2-PSK
Sampling rate	333.3 kHz
FFT size	1024
Number of used carriers	48
Frequency range	79.427 . . . 94.726 kHz
Symbol duration	3.072 ms

Table 6.1: Relevant parameters of the communication system.

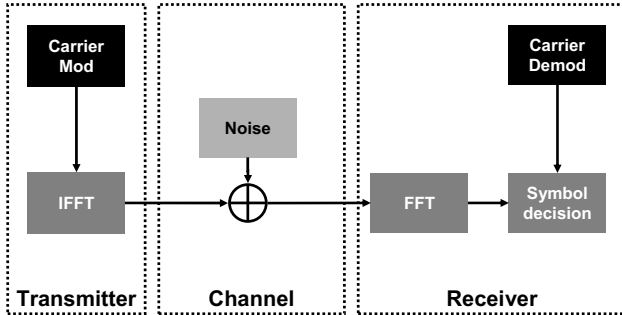


Figure 6.1: Overview of the OFDM scheme.

4 OFDM modulation

Orthogonal frequency-division multiplexing is a popular method to implement multi-carrier communication systems. The sub-carriers are complex harmonics, each of which can be modulated with a different traditional single-carrier modulation scheme (e.g. PAM, PSK, QAM), although usually all sub-carriers use the same scheme to reduce complexity. The modulation/demodulation process is implemented efficiently using FFT algorithms [12], see Figure 6.1. For PLC applications, phase shift keying is the preferred sub-carrier modulation. Due to the fact that PSK demodulation only indirectly takes into account the signal amplitude, PSK can be considered more robust than e.g. QAM, because it reduces the sensitivity to channel attenuation. Note that, since information is conveyed by the phase of the sub-carriers exclusively, each sub-carrier and thus each OFDM symbol has the same signal energy. This also proves advantageous for the requirements concerning analog amplifiers at the transmitter and the receiver.

4.1 BPSK redundancy

The OFDM system described in Section 3.2 uses BPSK as sub-carrier modulation scheme. Since its symbols have the largest Euclidian distance in the signal space diagram among all carrier modulation schemes, it provides the best resilience against noise. Since all OFDM symbols are Hermitian symmetric in the frequency domain and BPSK sub-symbols

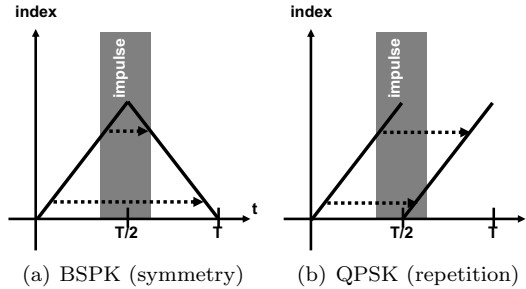


Figure 6.2: Influence of a noise impulse around the symbol center, for a symbol that is symmetric (a) and a symbol that consists of a symbol of half the length that is repeated (b)

are real-valued, OFDM symbols that only have BSPK modulated sub-carriers, have real-valued, symmetric spectra. Simple correspondences of the DFT show that also the time signals of such spectra are real-valued and symmetric. Thus they contain an inherent redundancy that could be employed to compensate impulse noise.

4.2 Redundancy through symbol repetition

Another possibility to introduce redundancy into a signal is to take a signal of half the length and repeat it, instead of making it symmetric. If we make the assumption that a single noise impulse is shorter than half an OFDM symbol (see 2.5), and that the impulse arrival rate λ ensures that there is most likely only one noise impulse per OFDM symbol, symbol repetition should be more effective than utilizing symbol-inherent symmetry. Suppose we can localize the impulse within the signal. Then, reconstruction of the corrupted parts is always possible for the repeated symbol. For the symmetric symbol however, the possibility of symbol reconstruction is dependent on the localization of the corrupted parts. Figure 6.2 clarifies this statement. If the impulse occurs in the vicinity of the axis of symmetry, both redundantly transmitted signal values are corrupted, and reconstruction is not possible. In order to obtain a redundant signal through repetition while maintaining the original data rate, one can use OFDM symbols of half the length with a higher order

PSK scheme, e.g. QPSK if BPSK symbols are to be repeated once. This has the additional benefit of reducing the maximum required FFT size within the system by a factor of two.

4.3 STFT, block-wise analysis

To make use of the redundancy within such modified OFDM symbols it is indispensable to locate the impulse within the received signal. To this end, a signal representation is required that offers time resolution, as opposed to the Fourier transform that offers no time resolution at all. Thus, it is desirable to use a method that provides a representation of the signal in time domain and frequency domain at the same time, as e.g. the Short-time Fourier transform (STFT), Wavelet-based approaches or the Wigner-Ville-Distribution. Because of its similarity to the Fourier transform (which is implemented in every OFDM system anyway), we use the STFT for our explanation within the scope of this paper, but without restricting the described method to this representation (similar trials have been made using a wavelet packet transform).

The STFT $X^\gamma(n', k)$ of a signal x_n can be constructed by first multiplying the signal with a time-shifted window $\gamma_{n-n'}$ and then taking the Fourier transform of the windowed signal. If γ is a rectangular window with size L being a divisor B of the signal length N , and the time shifts n' are multiples of this size, i.e.

$$N = B \cdot L \quad \text{and} \quad n' = b \cdot L, \quad (6.7)$$

then the STFT can be expressed as

$$X(b, k) = \sum_{n=b \cdot L}^{(b+1) \cdot L - 1} x_n e^{-j2\pi \frac{nk}{L}} \quad (6.8)$$

with

$$k \in [0 \dots N - 1] \quad \text{and} \quad b \in [0 \dots B - 1]. \quad (6.9)$$

This is the same as dividing the signal into B blocks of length L and then calculating the (zeropadded) Fourier transform of each of the blocks.

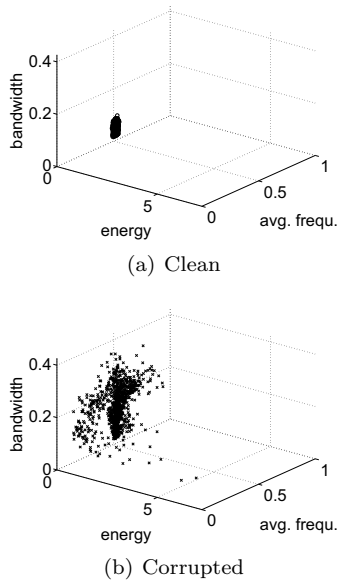


Figure 6.3: Features of clean blocks compared to corrupted blocks.

5 Signal feature classification

The basic idea for detecting noise impulses within the received OFDM symbol is to compute the general signal properties from chapter 2 for each block introduced by the STFT in Equation 6.8. Having calculated the STFT, each block can then be classified based on the calculated properties as either corrupted or clean. This is equivalent to creating a three-dimensional feature space with the dimensions *signal energy*, *average frequency* and *bandwidth*. Figure 6.3 shows that corrupted and clean blocks can be distinguished from each other very easily by means of this feature space.

5.1 Noise/signal separation in the feature space

As has been shown in section 2.4, all clean OFDM symbols have the same energy, average frequency and bandwidth and are therefore concen-

trated in a single point in feature space. Experiments showed that, when taking only parts of OFDM symbols (cf. ‘blocks’ in 4.3) into account for calculating these features, the features vary, but only in a comparably small area of the feature space, as can be seen in Figure 6.3(a). Opposed to this, extensive analysis of recorded noise impulses showed that their features vary within the whole feature space (see section 2.5 and Figure 6.3(b)). This implies that a reliable separation of clean and corrupted signals should be possible in most cases. Figure 6.3 illustrates that although most points that belong to the noise cloud can easily be separated from the clean ones, both clouds overlap. However, this overlap results mostly from trailing ends of impulses within the classified blocks, which lead to a classification as noisy, but hardly affect the signal.

5.2 Feature space risk estimation via training

Experiments showed that a mere classification into corrupted and clean blocks works very reliably, but is not optimal for utilization in a reconstruction scheme. Since many of the measured impulses proved to not contain any energy within the actual passband of the PLC transmit signal, they do not pose a critical threat to correct data transmission. However, their occurrence has a relevant influence on the features, so they will be detected as corrupted signals nevertheless. In order to overcome the issue of such ‘false positive’ detections, an advanced classification is desired that also includes an estimation of the risk for the transmitted data.

The feature space is divided into equal sectors for the sake of defining classes, which can be done easily by quantizing the features. All blocks that are in the same sector are assumed to bear a similar risk with respect to the correctness of the data represented by the signal under consideration. It is then necessary to obtain a risk estimation for each class, which can be achieved by a training process.

Before the training starts, the receiver creates an empty table like in table 6.2 with a row for each class. The table is then filled with counts of how often a class occurs during training, and how often this appearance leads to symbol errors. During training a known training sequence of symbols is communicated from the transmitter to the receiver. The receiver will thus have both a corrupted and a clean version of the symbol. Now the receiver can demodulate the clean symbol to obtain the original

Table 6.2: Empty table at the beginning of the risk training (if only four classes are used).

class Index	#Occurrences	#Symbol Errors
00	0	0
01	0	0
10	0	0
11	0	0

data. Then, demodulation is performed for each block, where only the current block is taken from the corrupted signal. After a comparison of the restored data with the original data it is known whether inserting this block produced a symbol error or not. After the classification of the block according to its features, the number of occurrences is recorded in the initially created table and also whether it resulted in errors.

After the whole training sequence has been completed, the risk estimation per class is simply the ratio of symbol errors produced by a class and the number of its occurrences:

$$R_{class} = \frac{\text{SymbolErrors}_{class}}{\text{Occurrences}_{class}}. \tag{6.10}$$

6 Implementation and simulation

6.1 OFDM symbol reconstruction algorithm

In order to make further use of the obtained risk estimation, a weighted average of corresponding blocks in the time domain according to

$$x_{nr} = \frac{R_2}{R_1 + R_2} \cdot x_{n1} + \frac{R_1}{R_1 + R_2} \cdot x_{n2}, \tag{6.11}$$

showed good results. Here, R_1 and R_2 are the risks of the two blocks taken from the trained risk table.

The proposed overall algorithm to reduce errors due to impulse noise can finally be summarized as:

1. Receive possibly noisy symbol

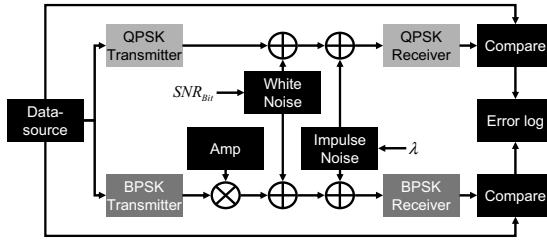


Figure 6.4: Simulation setup.

2. Perform $\frac{N}{B}$ -point FFT for each of the B Blocks (Equation (6.8))
3. Calculate and quantize features for each block based on its FFT
4. Perform risk look-up for calculated features
5. Perform weighted average of corresponding blocks (Equation (6.11))

After that, the commonly applied OFDM demodulation can be carried out based on the averaged signal.

6.2 Simulation setup

To show the effectiveness of the proposed algorithm, simulations of transmissions have been carried out. The overall simulation setup is depicted in Figure 6.4. The two systems under test are the BPSK based OFDM system introduced in [11], and a system that utilizes QPSK with symbol repetition and the proposed risk estimation/signal averaging. The number of blocks in the QPSK system are chosen as four. The symbol length of the QPSK system was set to 512 samples, assuring the same data rate as with the BPSK system. The amplifier in the BPSK chain is necessary to ensure the same energy per bit for both methods.

The background noise is simulated as White Noise with a fixed standard deviation σ , which ensures a given SNR per bit SNR_{Bit} .

As stated in Section 2.5 six mathematical models of typical impulse envelopes were obtained, each with a set of parameters that can be determined independently for each instantiation. Figure 6.5 shows an example impulse of each model. For simulation purposes, impulses are created at random points in time, where the intervals between the impulses are

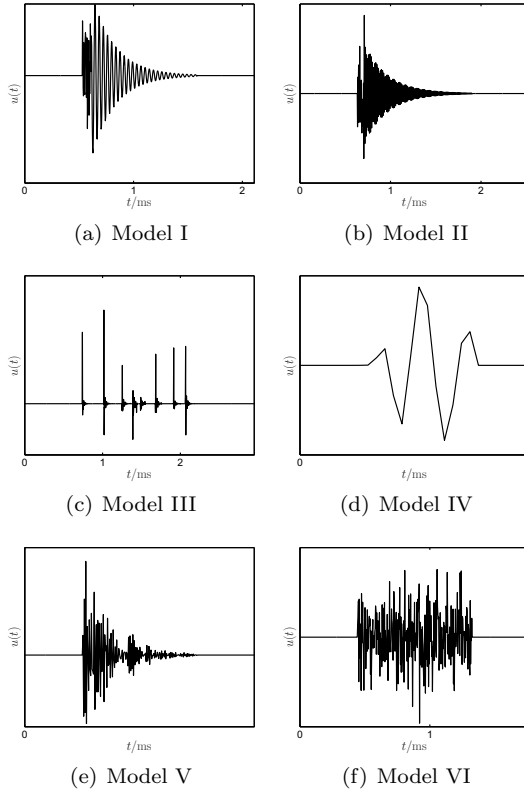


Figure 6.5: Examples of simulated impulses.

exponentially distributed with arrival rate λ . One of the six models is chosen randomly at every of these points in time. Each model is supposed to appear equally probable. An instantiation of the randomly selected model is created and added to the transmission signal. Since the characteristic parameter of impulse noise is rather its arrival rate than the energy per impulse, the ratio of impulse noise and clean signal is kept constant at an experimentally determined value for all SNR_{Bit} .

6.3 Simulation results

Simulations have been run with 10^4 symbols for each combination of SNR_{Bit} and λ . The resulting SNR_{Bit} to BER plots are shown in Figure 6.6. Up to a SNR_{Bit} of -20 dB the BER is dominated by background noise, and a higher SNR_{Bit} reduces the BER . The value at which the BER curve reaches a floor is determined by the impulse noise and the system's capability to handle it. The arrival rate λ of the impulses influences the stationary BER that can be achieved. The results in Figure 6.6 show that our proposed algorithm reduces the BER by up to a factor of ten below the BER of the unmodified OFDM system with BPSK while maintaining the same data rate.

7 Conclusion

We have presented a method for combating the detrimental effects of impulsive noise on OFDM-based multi-carrier modulation signals. Minor reconfigurations of the system parameters and investing moderate additional efforts resulted in a reduction of bit errors that could be verified by simulation. The method proposed in this work has yielded encouraging results in our comprehensive simulation scenario.

References

1. M. Zimmermann and K. Dostert, "Analysis and modeling of impulsive noise in broad-band powerline communications," *IEEE Trans. on Electromagnetic Compatibility*, vol. 44, no. 1, pp. 249–258, Feb 2002.
2. Gautier Avril and Mohamed Tlich and Fabienne Moulin and Ahmed Zeddami and Fabienne Nouvel, "Time/Frequency Analysis of Impulsive Noise on Powerline Channels," in *Home Networking*, ser. IFIP International Federation for Information Processing, vol. 256. Springer Boston, 2008, pp. 143–150. [Online]. Available: <http://www.springerlink.com/content/r47036x268j235lm/>
3. J. Bausch, T. Kistner, M. Babic, and K. Dostert, "Characteristics of Indoor Power Line Channels in the Frequency Range 50 - 500 kHz," in *IEEE Int. Symp. on Power Line Communications and Its Applications*, 0-0 2006, pp. 86–91.

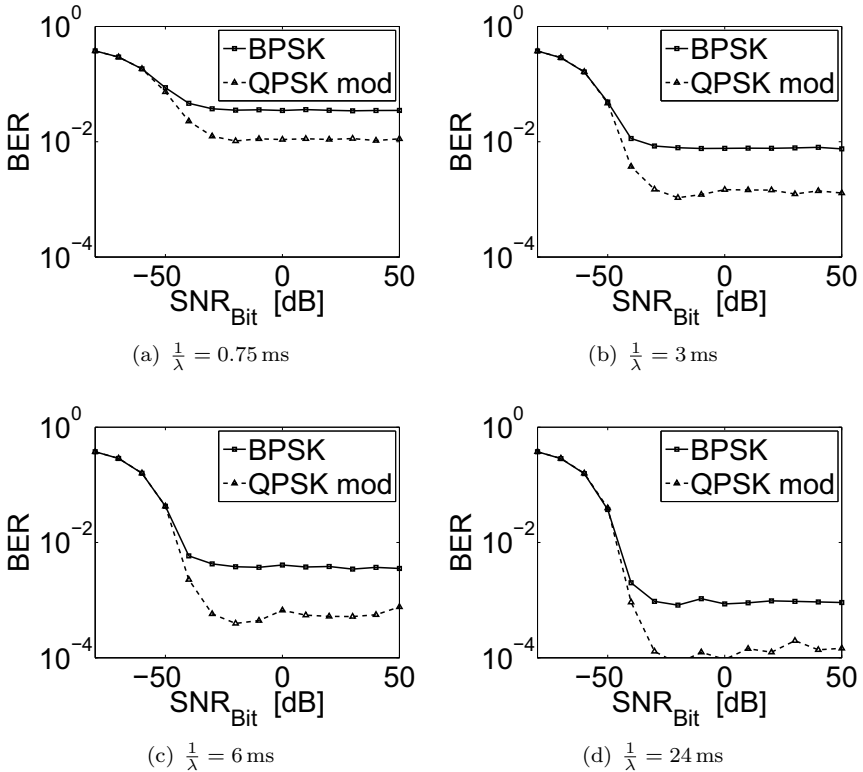


Figure 6.6: Simulation results.

4. M. Babic, J. Bausch, T. Kistner, and K. Dostert, “Performance analysis of coded OFDM systems at statistically representative PLC channels,” in *IEEE Int. Symp. on Power Line Communications and its Applications*, 0-0 2006, pp. 104–109.
5. J. Mitra and L. Lampe, “Coded narrowband transmission over noisy powerline channels,” in *IEEE Int. Symp. on Power Line Communications and Its Applications (ISPLC)*, 2009, 29 2009–April 1 2009, pp. 143–148.
6. EN 50065, *Specification for signalling on low-voltage electrical installations in the frequency range 3 kHz to 148.5 kHz. General requirements, frequency*

bands and electromagnetic disturbances, CENELEC Std.

7. U. Kiencke, M. Schwarz, and T. Weickert, *Signalverarbeitung: Zeit-Frequenz-Analyse und Schätzverfahren*. München: Oldenbourg, 2008.
8. O. Hooijen, “A channel model for the residential power circuit used as a digital communications medium,” *IEEE Trans. on Electromagnetic Compatibility*, vol. 40, no. 4, pp. 331–336, Nov 1998.
9. K. Dostert, M. Zimmermann, T. Waldeck, and M. Arzberger, “Fundamental Properties of the Low Voltage Power Distribution Grid Used as a Data Channel,” *European Transactions on Telecommunications*, vol. 11, pp. 297–306, 2000.
10. M. Zimmermann and K. Dostert, “A multipath model for the powerline channel,” *IEEE Trans. on Communications*, vol. 50, no. 4, pp. 553–559, Apr 2002.
11. T. Kistner, “Ein neuartiges mehrträgerbasiertes PLC-System mit störresistenter Synchronisation,” Ph.D. dissertation, Karlsruhe, 2008.
12. J. Bingham, “Multicarrier modulation for data transmission: an idea whose time has come,” *IEEE Communications Magazine*, vol. 28, no. 5, pp. 5–14, May 1990.

Robustness testing of an FSK PLC physical layer implementation by means of a channel emulator

Michael Bauer and Wenqing Liu

Karlsruhe Institute of Technology (KIT),
Institute of Industrial Information Technology (IIIT),
Hertzstr. 16, D-76187 Karlsruhe

Abstract Verifying the functionality of a communication system is a complex task. When it comes to determining the reliability of individual communication links in real-world scenarios, the task of verification becomes even more difficult, even more so in the case of power line communications. Yet, verifying the functionality and reliability of such communication links established by means of not yet mature technology is indispensable. In this paper, we propose a test procedure that allows for verifying the implementation of an FSK physical layer for communication over the mains grid. Furthermore, we present results that allow to determine the system's robustness in different scenarios. The proposed test procedure involves a transmitter and a receiver for establishing a uni-directional communication link and a PLC channel emulator that emulates the behavior of the communication channel in a reproducible manner.

1 Introduction

It is a well-established fact that the energy distribution grid states a difficult transmission medium for digital communications [1,2]. Nevertheless, the economic advantages of utilizing an already existing infrastructure for both, energy distribution and communication, at the same time are compelling enough to challenge the adverse behavior of the transmission channel. In the context of smart grids and automated metering infrastructures, PLC technologies are envisaged to provide the backbone

for bi-directional digital data transfer between distributed system components, aiming at more efficient energy consumption on a large scale. This involves data transmission between household appliances and smart home gateways as well as data transmission between smart meters and data concentrators, thus involving both, the so-called *in-house domain* and *access domain*.

Numerous PLC systems, i.e. technologies, have been brought to the market and some industry standards have been released, the numbers of both being expected to increase as the smart grid evolves. Only few of these standards actually establish test conditions. System performance has almost never been considered, apart from nominal values of bit rates provided by manufacturers themselves. System performance can be understood in several ways, in this context, however, we focus on the reliability and availability of the specified service, i.e. the quality of the communication link. Therefore, the focus of our discussion is on the physical layer of the communication system.

One reason for the lack of knowledge about system performance under adverse conditions might be that the PLC transmission channel is time-variant and therefore itself not suitable for testing, which renders system test and verification under real-world conditions almost impossible. Link quality and thus the observed system performance may vary significantly over time of day, depending on the current status of the mains grid. Influencing factors are known to be various, e.g. the number and kind of electrical appliances on the grid, signal propagation paths, number of switching events, etc.

In order to establish a test environment that provides reproducible and configurable scenarios, we have devised a channel emulator for PLC in low-frequency bands between 9 kHz and 500 kHz [3], focusing on the frequency bands specified in CENELEC EN 50065. Having such equipment at hand, the next step is to define test scenarios that in turn provide useful insights into system performance by measurement results. Different approaches to testing the reliability and availability of a PLC system are conceivable in general. In any case, the first step of testing must identify the limitations of the communication system under consideration, which thus states the focus of this work. The next step could then be system optimization. Test scenarios that have been identified to be problematic can be reproduced and the communication system can be improved iteratively.

2 Test setup

Figure 7.1 shows the overall setup that has been used for conducting the tests described in Sect. 3. Binary data is generated by a PC and handed to the FSK transmitter through an RS-232 COM port. The signal $s(t)$ generated by the transmitter is manipulated by the channel emulator according to the user-defined settings resulting in the receive signal $r(t)$. The binary data output by the receiver is estimated based on this signal and may contain erroneous bits. Bit errors are identified by comparing received bits with the originally transmitted bits.

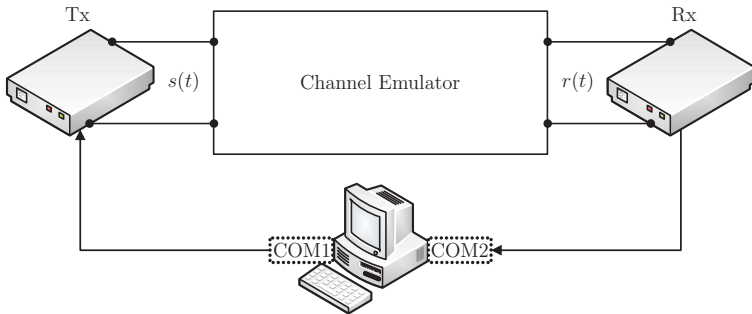


Figure 7.1: Overall test setup.

In order to determine the parameters of $r(t)$, e.g. the receive signal level, the signal is observed by means of a spectrum analyzer and a digital storage oscilloscope (DSO).

2.1 Communication system under test

The communication system under consideration is an implementation of an FSK modulated physical layer for PLC. Since the test setup requires unidirectional transmission, one modem operates in transmit mode and the other in receive mode; the modems do not change their roles during the whole test.

Binary information is encoded according to an FSK modulation scheme that utilizes two carrier frequencies, $f_{C,1} = 100$ kHz and $f_{C,2} = 108$ kHz. Figure 7.2 depicts the carrier frequencies and the superposition of the

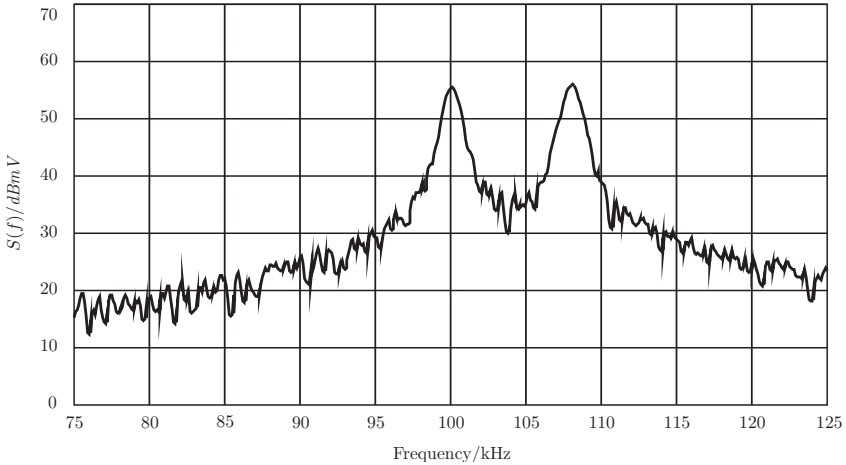


Figure 7.2: Transmit signal spectrum. The maximum signal level is approximately 55 dBmV.

$\frac{\sin(x)}{x}$ -like spectra that result from rectangular pulse shaping for each of the carriers.

Modulation Scheme	FSK
Utilized Frequency Range	$f_{C1} = 100 \text{ kHz}$, $f_{C2} = 108 \text{ kHz}$
Symbol Duration	0.833 ms

Table 7.1: System parameters of the FSK implementation.

Prior to transmission, the receiver re-arranges binary data bytes received from the PC via RS-232 to frames of $B_{Frame} = 15 \cdot 8 = 120$ bits. A frame consists of a preamble followed by payload counting 120 bits.

The channel emulator allows for modifying the following parameters: channel transfer function, background noise, narrowband noise, and impulsive noise. Furthermore, it emulates the access impedance. Of course, it is necessary to specify scenarios so that the sources of bit errors can be related to a number of possible sources being as low as possible.

3 Test procedure and test results

For each of the test scenarios described in the following, a set of random binary data is transmitted while the channel parameters remain constant.

The test cases described in the following are defined so that only one single channel parameter or noise class, respectively, affects the transmission of the test data bulk. This parameter is then varied within an interval specified uniquely for each of the test cases. Since the $\frac{E_B}{N_0}$ actually experienced by the receiver cannot be obtained directly from the DUTs, the bit error rate is related to the channel parameters measured by means of a spectrum analyzer.

Note that the spectra have been recorded by means of the “max hold” function. Thus, all spectra displayed in the following show an optimistic estimate of the carrier signal PSD, and a pessimistic estimate of the noise signal PSD.

The bit error ratio corresponding to each of the parameter settings is calculated from the ratio of the number of received bits $B_{r,err}$ deviating from the originally transmitted bits $B_{r,total}$. Ideally, the BER would be obtained by

$$BER = \frac{B_{r,err}}{B_{r,total}}. \quad (7.1)$$

However, as described in Subsect. 2.1, data is transmitted in frames of 120 bits. Furthermore, it is important to detect the loss of whole frames due to transmission errors. Thus, the bit error ratio is calculated for each of the frames, i.e.,

$$BER_{Frame} = \frac{B_{r,err}}{B_{Frame}}.$$

In order to obtain significant statistics, a large number of frames must be transmitted for each of the test cases. Then the BER equation

$$BER = \frac{1}{N_{Frame}} \sum_{i=1}^{N_{Frame}} BER_{Frame,i} \quad (7.2)$$

yields the same result as in Eq. (7.1). Mind that, as opposed to well-known graphs displaying theoretically derived bit error probabilities, a

bit error ratio of 1 may occur during the measurements. Due to the fact, however, that this is a very unlikely event, it is assumed that frames with $BER = 1$ are due to channel interference causing the frame detection method to fail. Such frames are considered as "lost" frames and therefore accounted for in the frame loss ratio (FLR) rather than BER.

For each of the configurations in a test scenario, it is defined as the number of lost frames divided by the total number of frames transmitted while the configuration of parameters of a test scenario remains unaltered,

$$FLR = \frac{N_{Frame,lost}}{N_{Frame}}. \quad (7.3)$$

3.1 Step 1: Attenuation by channel transmission function

First of all, we assume a frequency-selective channel transmission function (CTF) without notching. As described in subsection 2.1, the communication system relies on two carrier frequencies $f_{C,1}$ and $f_{C,2}$ that are interpreted either independently or together, depending on the estimated noise levels for each of the correlators.

Therefore, we consider three test cases with differing prototype frequency response

1. $\tilde{H}_0(f)$: "flat" channel transmission function affecting both, $f_{C,1}$ and $f_{C,2}$
2. $\tilde{H}_1(f)$: prototype channel transmission function letting $f_{C,1}$ pass, but not $f_{C,2}$
3. $\tilde{H}_2(f)$: channel transmission function letting $f_{C,2}$ pass, but not $f_{C,1}$

Each of the prototype frequency responses will be applied to the transmit signal at different SNR levels c_0 , c_1 , and c_2 ,

$$H(f) = \begin{cases} c_0 \cdot \tilde{H}_0(f) \\ c_1 \cdot \tilde{H}_1(f) \\ c_2 \cdot \tilde{H}_2(f) \end{cases}. \quad (7.4)$$

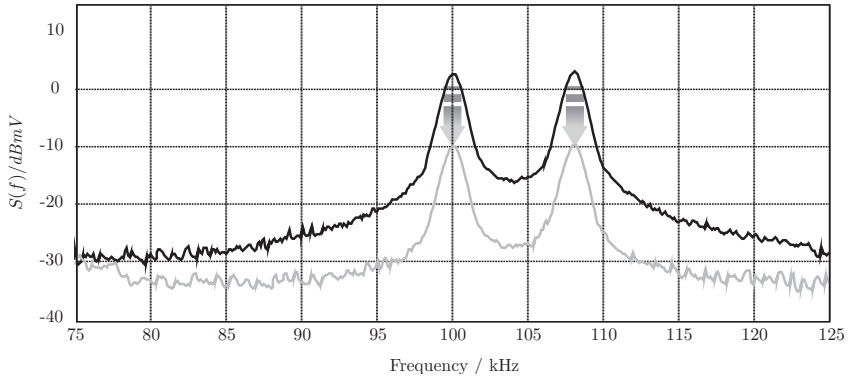


Figure 7.3: Maximum (black) and minimum (grey) PSD of the receive signal. The corresponding receive signal levels are 2.5 dBmV and -10 dBmV, respectively.

Results for flat channel transmission function

In this test scenario, the coefficient c_0 is varied so that the amplitudes of the receive signal vary between the two power spectral density curves depicted in Figure 7.3. The receive signal levels are very low. Compared to the levels in Figure 7.2, attenuation is 52.5 dB and 65 dB, respectively.

The resulting bit error ratio is displayed in Figure 7.4. The receiver is obviously operated at the limits of its sensitivity. At a signal level of -10 dBmV, the receiver cannot detect the start of frame anymore, which results in a frame loss ratio of 100%. At an attenuation level of -65.5 dB, the frame loss ratio drops to 98.9%, and a bit error ratio can be calculated. The frame loss ratio further drops to 47.9% at -63.75 dB at constant bit error ratio and 10% at -63.05 dB attenuation, where the bit error ratio starts to improve. From attenuation levels of -62.4 dB, the frame loss ratio remains at zero. Note that the bit error ratio becomes zero as soon as the attenuation is less than -56.34 dB.

For each of the points in the resulting BER plot, 550 packets have been transmitted, resulting in a total of 66000 bits.

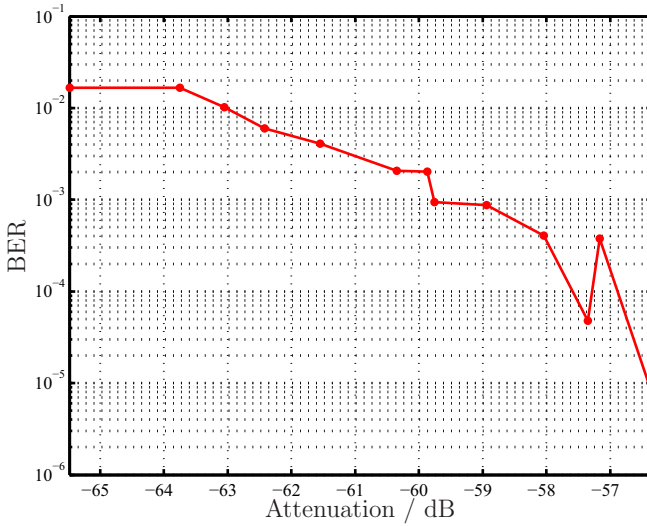


Figure 7.4: Bit error ratio for scenario “Flat channel transmission function.”

Results for channel transmission function affecting one carrier

Figure 7.5 depicts the PSD of a transmit signal with carrier frequencies f_{C1} and f_{C2} . In this test scenario, $\tilde{H}_2(f)$ is utilized. The attenuation for f_{C1} is increased gradually while f_{C2} remains at the same level.

The resulting bit error ratio is displayed in Figure 7.6. Again, the receiver is obviously operated at the limits of its sensitivity. However, the frame loss ratio does not reach 100%. Instead, the maximum observed frame loss ratio is 40% at -30.77 dB carrier attenuation, drops to 16.9% at -29.72 dB and reaches zero at -28.19 dB. Both, BER and FLR, become zero at attenuation levels less than -18.11 dB. 510 packets have been transmitted for each of the points in the graph.

The results in Figure 7.6 prove that the system can tolerate the loss of one carrier frequency to great extent. The mechanism for evaluating the transmission quality in each of the correlators obviously works correctly and improves transmission quality dramatically.

Similar behavior is expected for the case of prototype CTF $\tilde{H}_1(f)$,

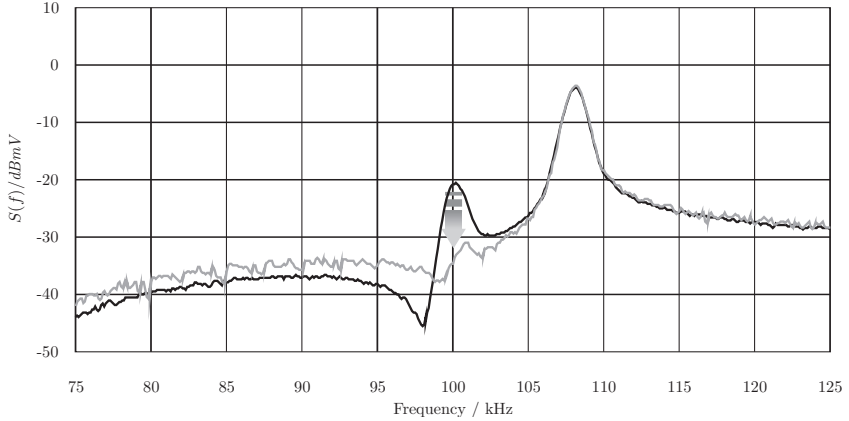


Figure 7.5: PSD of the receive signal with mildly (black) and strongly (gray) attenuated carrier f_{C1} . The corresponding receive signal levels are -20.88 dBmV and -34.9 dBmV, respectively.

therefore we assume that this test case has already been covered by the test scenarios described up to now.

3.2 Step 2: Background noise

For this test scenario, we consider level and PSD $\tilde{N}(f)$ of the background noise to be independent of the CTF, thus $H(f) = 1$.

Similar to the approach described in subsection 3.1, the prototype PSD of the background noise will have the following properties:

1. $\tilde{N}_{BG,0}(f)$: “flat” noise PSD affecting both, $f_{C,1}$ and $f_{C,2}$
2. $\tilde{N}_{BG,1}(f)$: prototype noise PSD affecting $f_{C,1}$, but not $f_{C,2}$
3. $\tilde{N}_{BG,2}(f)$: prototype noise PSD affecting $f_{C,2}$, but not $f_{C,1}$

Results for flat background noise PSD

In the first test scenario involving background noise generated by means of the channel emulator, the PSD of the background noise is assumed to be constant for both carrier frequencies. Again, the signal carrier frequencies are not attenuated by the channel transfer function. The

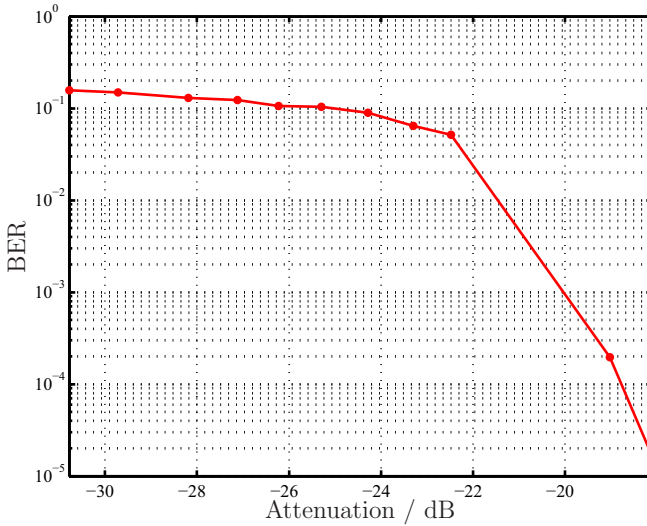


Figure 7.6: Bit error ratio for scenario “Channel transmission function affecting one carrier.”

background noise level, however, is increased gradually, as depicted in Figure 7.7.

The resulting bit error ratio is displayed in Figure 7.8. The curve progression resembles that of the theoretical bit error probability for FSK. The frame loss ratio is 73.5% at $\text{SNR}_{BG} = 1.27$ dB, 24.7% at $\text{SNR}_{BG} = 2.07$ dB, and attains zero starting from $\text{SNR}_{BG} \geq 3.07$ dB. Neither bit errors nor frame losses occur for $\text{SNR}_{BG} \geq 12.16$ dB. 510 frames have been transmitted for each of the configurations.

3.3 Step 3: Narrowband noise

For this test scenario, we consider the PSD of the background noise $\tilde{N}(f)$ to be zero. Furthermore, no attenuation is applied to the transmit signals, i.e. $H(f) = 1$. Instead, a sinusoidal and thus narrowband noise

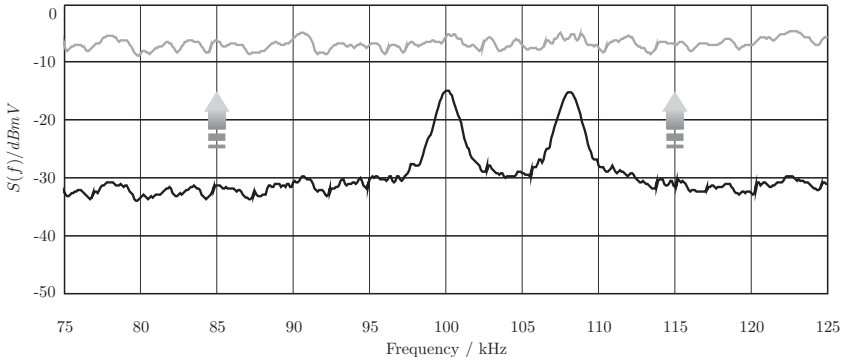


Figure 7.7: PSD of the receive signal with low (black) and high (gray) background noise level. The background noise signal level increases from -33.43 dBmV to up to -8.55 dBmV.

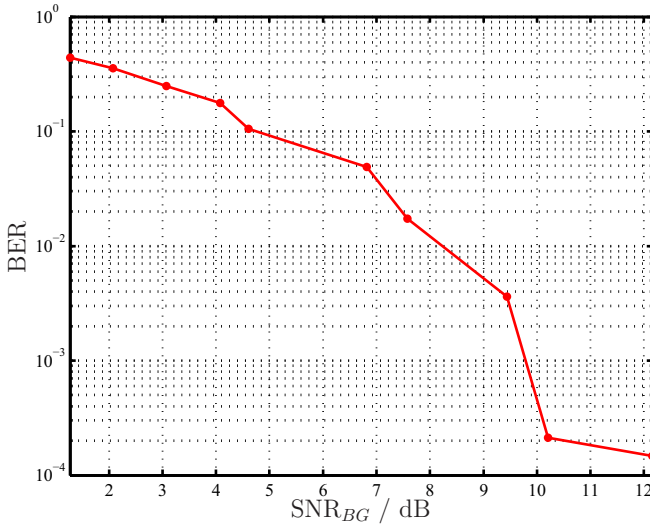


Figure 7.8: Bit error ratio for scenario “Flat background noise PSD.”

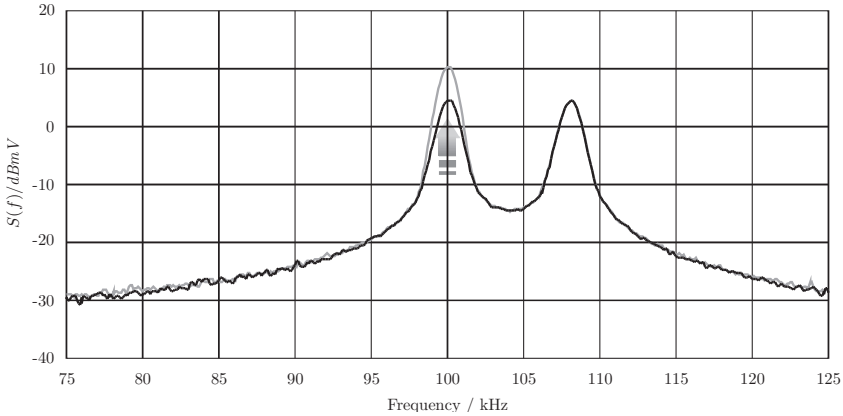


Figure 7.9: PSD of the receive signal with low (black) and high (gray) narrowband noise level affecting f_{C1} . The receive signal level is constant at 4.41 dBmV, while the noise signal level is increased gradually until it attains its maximum at 10.15 dBmV.

signal is added,

$$n_{BG} = A \cdot \sin(2\pi f_0 t).$$

The frequency is kept constant at $f_0 = 100$ kHz, while the amplitude A is varied as shown in Figure 7.9.

The resulting bit error ratio is displayed in Figure 7.10. The frame loss ratio is 100% at $\text{SNR}_{NB} = -1.33$ dB, but quickly drops to only 1.4% at $\text{SNR}_{NB} = -0.57$ dB. Starting from $\text{SNR}_{BG} \geq -0.36$ dB, it attains zero. Bit errors cease to occur from $\text{SNR}_{NB} \geq 1.28$ dB. Again, 510 frames have been transmitted in order to estimate each value for bit error ratio and frame loss ratio, respectively.

3.4 Step 4: Impulsive noise

Impulsive noise has been approximated for this test by a waveform according to

$$n_{Imp}(t) = A_0 \cdot \sin(2\pi f_p t) \cdot \exp(-d \cdot t).$$

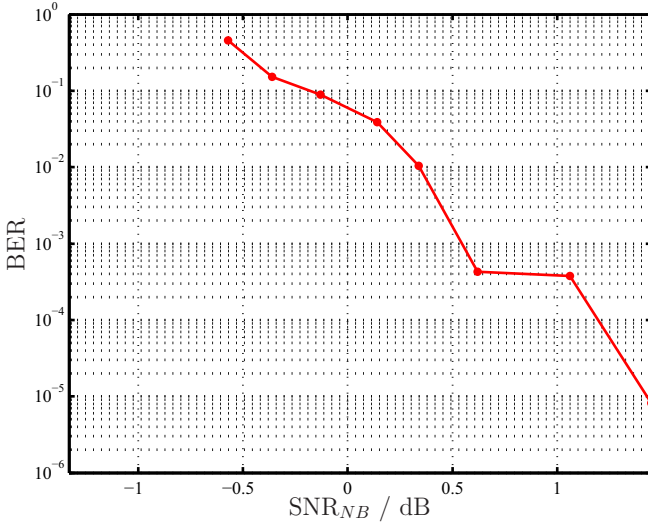


Figure 7.10: Bit error ratio for scenario “Narrowband noise.”

The parameter A_0 has been varied, as well as the impulsive noise waveform duration t_w . The test has been run with two waveform durations $t_{w,1} = 85\mu\text{s}$, see 7.11(a), and $t_{w,2} = 170\mu\text{s}$ depicted in 7.11(b). The pseudo-frequency is kept constant at $f_p = 100\text{ kHz}$ for all measurements. In order to ensure that a sufficient number of FSK symbols and packets coincide with an instance of an impulsive noise waveform, the waveforms are repeated periodically with a repetition rate of $1/(3.33\text{ ms})$. Since impulsive noise did not result in bit errors for the full transmit signal amplitude depicted in Figure 7.2, the CTF had to be modified so that it causes an attenuation of the transmit signal.

The resulting bit error rates are displayed in Figure 7.12. At the same worst-case SNR, the longer impulsive noise waveform causes significantly higher bit error ratios than the shorter waveform. Frame losses do not occur except for a FLR of 0.78% at $\text{SNR}_{Imp} = 2.36\text{ dB}$, which is due to one lost frame presumably caused by one impulse obstructing the frame synchronization sequence. For this scenario, 500 frames have been

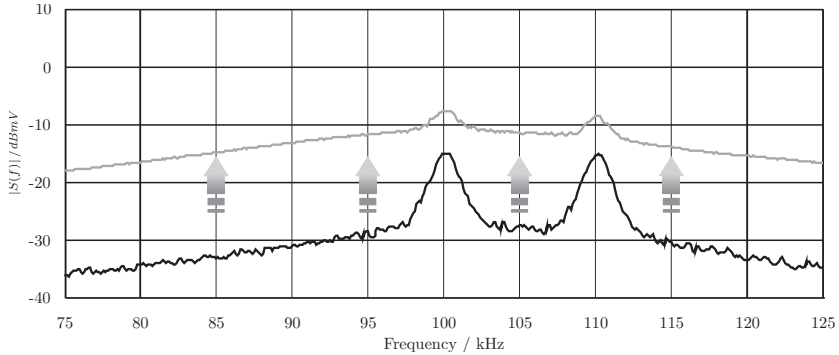
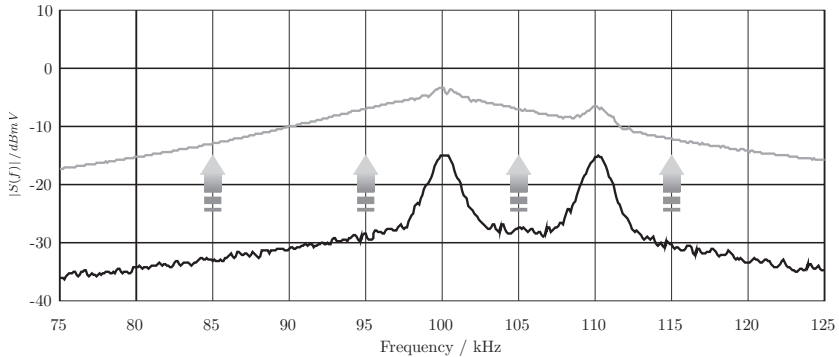
(a) Impulsive noise and signal PSD – $t_{w,1} = 85\mu\text{s}$.(b) Impulsive noise and signal PSD – $t_{w,1} = 170\mu\text{s}$.

Figure 7.11: PSDs of the receive signal with low (black) and high (gray) impulsive noise PSDs for different noise signal waveform durations.

transmitted in order to obtain each of the BER estimates. This number is comparably low, but is still justifiable since the noise waveforms appear periodically.

4 Summary

In this work, we have presented a selection of test scenarios for identifying the limitations of system performance of an FSK physical layer for

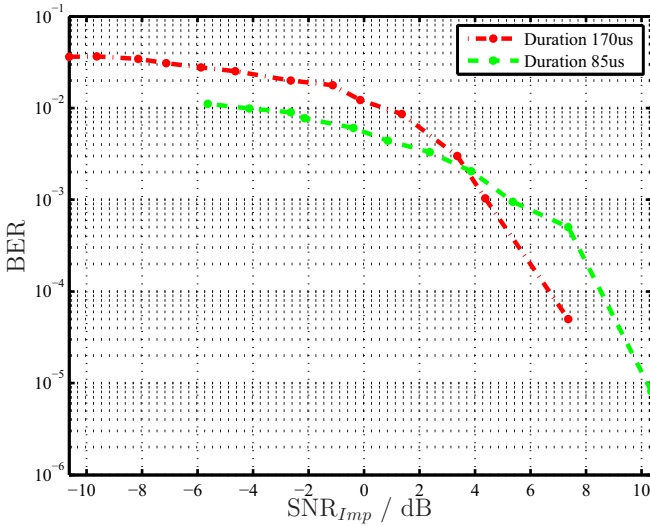


Figure 7.12: Bit error ratio for scenario “Impulsive noise.”

PLC by means of a channel emulator. As a result, the system performance for different scenarios has been documented, thereby identifying the limitations of the implementation under consideration. One significant conclusion is that the system can deal remarkably well with high signal attenuation, and is very robust even if one carrier signal is severely obstructed by narrowband noise. The measurements serve very well as a reference for performance comparison with other systems.

References

1. M. Götz, M. Rapp, and K. Dostert, “Power line channel characteristics and their effect on communication system design,” *IEEE Communications Magazine*, vol. 42, no. 4, pp. 78–86, Apr 2004.
2. J. Bausch, T. Kistner, M. Babic, and K. Dostert, “Characteristics of indoor power line channels in the frequency range 50–500 kHz,” in *IEEE Int. Symp. on Power Line Communications and its Applications*, 2006, pp. 86–91.

3. M. Bauer, W. Liu, and K. Dostert, "Channel emulation of low-speed PLC transmission channels," in *IEEE Int. Symp. on Power Line Communications and its Applications (ISPLC)*, 2009.

Least-squares-estimation based zero-crossing prediction for an automated PLC channel measurement system

Wenqing Liu and Yuelou Bao

Karlsruhe Institute of Technology (KIT),
Institute of Industrial Information Technology (IIIT),
Hertzstr. 16, D-76187 Karlsruhe

Abstract For power line communication (PLC) applications, the robustness and accuracy of synchronization is one of the most important factors. The zero-crossing (ZC) based global synchronization has superiority over other common symbol synchronization schemes for PLC channels. The commonly used ZC detection circuit is based on comparator and susceptible to transients. This paper presents a least-squares (LS) estimation-based method which predicts the ZCs within a period of mains voltage. Computer simulations prove its robustness and accuracy even at the appearance of large transients existing in common power line channels. Its ability of detecting, and extracting the noises can be used to capture and analyze transient noises. It can also track the change of mains frequency as well as fluctuation of amplitude, providing quality information of power networks. Although the method is computationally intensive, it is mainly based on multiplications and accumulations which can be implemented in ordinary digital signal processors (DSPs) or field programmable arrays (FPGA).

1 Introduction

Power line communication (PLC) technology is used to transfer data over the existing power transmission lines. Its low cost and wide coverage range makes it one of the key technologies in the development of automated meter reading (AMR) or even advanced metering infrastructure (AMI) services. However, the low voltage power transmission lines

are optimized for delivering electricity, they are not guaranteed for data transfer at higher frequencies. Many PLC systems suffer from serious deficiencies due to insufficient information on channel characteristics such as access impedance, transfer function and existing interferences. Therefore, measurement of the power line channels and evaluation of their characteristics should be the first and one of the most important steps before system design begins. A measurement setup has been introduced in [1], with which a mass of indoor power line channels are investigated. Although this setup has a very high mobility and it can measure access impedance, the amplitude response and the noise spectrum, it is unable to investigate phase or delay response. An automated measurement system (AMS) will make the measurement easier. The AMS can be considered as a communication system which is composed of units of the same design. Each unit consists of a transmit part, a receive part, and circuit components for power supply, synchronization, and state control. A unit can be configured as either a transmitter or receiver during measurement. The transmitter generates sequences of test signals at predefined time points.

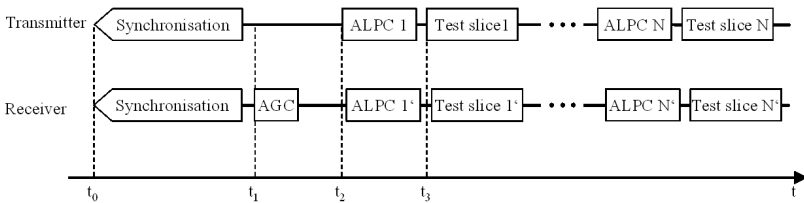


Figure 8.1: Measurement procedure of AMS.

Figure 8.1 illustrates the work flow. The transmitter and receiver begin a new measure event at t_0 by synchronizing with each other, and the algorithm will be discussed in detail in the following parts. The receiver adjusts its gain factor through the automatic gain control (AGC) component at t_1 before the first test stimulus comes and holds the gain factor constant until the current measure event is finished. The transmitter has a automatic level and phase control (ALPC) part to make sure the test signal has a defined amplitude and phase despite of the time-varying access impedance. The test slices are sampled, and the system

estimates their parameters and finally calculates the transfer function of the channel under test.

The AMS does not need high data rate. The only requirement on speed is that a complete measurement over the whole frequency range should be finished before the access impedance or the transfer function change. According to results of earlier measurements, the interval between two changes can be several minutes to even hours. As mentioned before, the validity of measurement results, especially those for the phase estimation, rely largely on the robustness and accuracy of the synchronization. In this paper we will focus on the design of a robust and reliable synchronization method. The first part gives an overview over existing methods, their pros and cons and the availability for the AMS. The second part analyzes a currently widespread zero-crossing detection based synchronization method. The third part presents our proposed solution. Finally simulation results and conclusions are given.

2 Typical methods of synchronization

In some communication systems, symbol synchronization is used. As preambles, chirps or random sequence having wide bandwidth in spectrum and complicated waveform in time space are widely used. These signals have satisfying resistance against most additive background noise and narrowband interference. Furthermore, their time autocorrelation function possesses an explicit maximum. A correlator at receiver can provide accurate detection by correlating the received signal with the stored preamble. However, it is improper to apply this scheme to PLC systems because of the tough channel conditions. The frequency-selective attenuation and possibly existing resonance might largely decrease the preamble energy and distort the waveform resulting in detection failure. Although the Schmid-Cox method introduced in [2] cancelled effects of the channel by multiplying samples from the first half with the corresponding samples from the second half, the timing metric has a flat region impeding an accurate timing estimation. Minn-Zeng-Bhargava method in [3] produces a peak in the timing metric instead of a flat plateau, improving the accuracy. However, it is still suffering from high attenuation and interference. Furthermore the symbol is also delayed by the channel transfer function, which makes the evaluation of phase

response and group delay of the channel under test almost impossible.

Another way to realize symbol synchronization can be accomplished by integrating timing information in test slices. At the receiver, different methods such as decision-directed or non-decision-directed methods can be used to achieve self-synchronization [4]. A typical application is the pilot tone in many multicarrier-based communication systems. With pilot tones the spectrum difference between test slice and pilot slice can be investigated. However, the test slice has to share the transmit power with pilot tones, leading to a weakened signal-to-noise ratio. Besides, some or even all subcarriers could be highly degraded by attenuation and noise of the PLC channel. In this case, the required unaltered pilot tones are no longer fulfilled and the synchronization may fail.

In some low speed communication systems, so called global synchronization is used. The transmitter and receiver share the same timing source which provides a very precise timing signal. Detection of zero-crossing (ZC) of the mains voltage provides a robust and channel independent alternative for synchronization. In electronics a ZC is considered the instantaneous point at which the voltage changes from positive to negative value or vice versa. In low voltage three-phase power system, the mains voltage has approximately sine waveform [5], which has two ZCs within a cycle. Within the channel of interest, the transmission length is much smaller than the wavelength of the mains voltage, a ZC is detected almost at the same time on any site. The channel also imposes little attenuation on the mains voltage since it is optimized for maximum transmission of mains power. Furthermore the mains voltage has large amplitude compared with background noise and most impulsive interferences. Although dangerous transients could occur, most of them have very small pulse width. From these points of view, the mains voltage could be a good choice for synchronization of AMS.

3 Comparator-based ZC detection

The power system in North America has a nominal frequency of the 60 Hz, while in Europe and many other areas the nominal frequency is set to 50 Hz. We will use the 50 Hz as our nominal frequency in the rest of the paper. However, the methods could also be applied to 60 Hz power system with minor adjustment. An easy to realize ZC detection circuit,

converting the 50 Hz mains voltage into low voltage rectangular signal has been introduced in [5]. This circuit and its slightly modified versions are used in many PLC modem designs.

3.1 Detector hardware

The basic structure of the detector circuit is shown in Figure 8.2. As described in [6], the CMOS operational amplifier $OP1$, working as a comparator, is supplied from the 230 V mains over a large resistor $R1$. The mains voltage is scaled by the combination of $R1$ and $R2$. The diode $D1$ prevents damage to $OP1$ caused by excessive negative voltage. Diode $D2$ rectifies the incoming AC voltage. The Zener diode $D3$ and the capacitor $C1$ are used to stabilize and filter the supply voltage for $OP1$. The optocoupler generates a rectangular signal $Sync$ at 50 Hz with a duty cycle of about 50% and galvanically separates the low voltage part from the 230 V mains side.

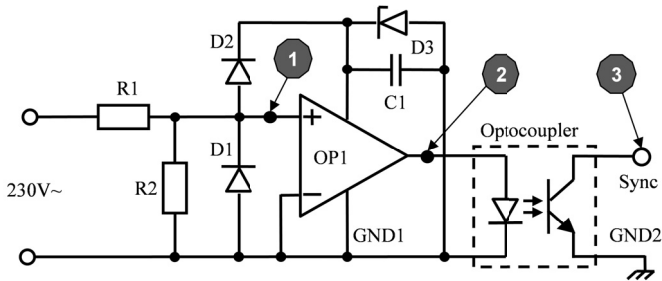


Figure 8.2: Detector hardware.

This detector has an advantage over other detector designs because of its low power requirement and simplicity. Its capability of potential isolation makes it appropriate in PLC applications. However, several points should be considered with respect to detection precision and robustness against interference.

3.2 Analysis of burst error

Burst detection errors are mentioned in [6] and [7]. Figure 8.3 shows an example of those errors. The y-axis refers to the detected time interval

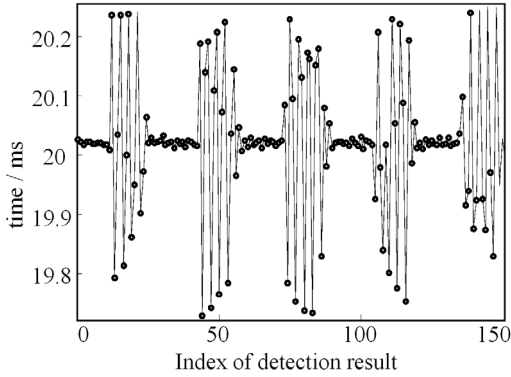


Figure 8.3: Burst errors of detector.

in milliseconds between two adjacent zero crossings. The x-axis is the index of detection samples. It is observed that five clusters of burst errors appear within 150 results. The maximum detected interval is over 20.3 ms and the minimum is about 19.5 ms. These errors are described as stochastic events causing serious synchronization problems.

Figure 8.4 illustrates the platform to capture burst errors. It is composed of the ZC detector, a FPGA board and a two-channel oscilloscope. Three points of the detector circuit are to be observed, two points at one time. Points 1 through 3 refer to the positive input of *OP1*, the output of *OP1* and the output of the optocoupler respectively. Point 2 is also the input of the optocoupler, see also Figure 8.2.

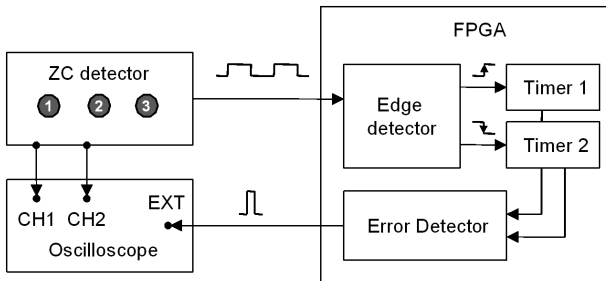


Figure 8.4: Platform to capture burst errors.

The output signal is feed into the edge detector in the FPGA, where both rising and falling edges are detected. Timer 1 and 2 measure timing intervals between two consecutive rising and falling edges respectively. In error detection module, two thresholds, 90% and 110%, define the lower and upper boundaries of an error-free area. As soon as the measured value goes beyond this area, a pulse is generated to trigger the oscilloscope so that the disturbed signals at probes can be captured in time.

Figure 8.5 shows examples of error-free and disturbed signals at point 2 and 3 respectively. The output of *OP1* is inverted by the optocoupler. If there is no error, as shown in the left, a rectangular signal having a frequency of 50 Hz and duty-cycle of about 50% appears at output of optocoupler. The plot in the right gives an example of burst error. The *OP1* signal are corrupted at ‘high’ level by a cluster of narrow negative peaks which are then converted as narrow pulses by the optocoupler. We can see that the coupler just inverts the signal at its input, no matter noise or signal, it generates no burst error itself.

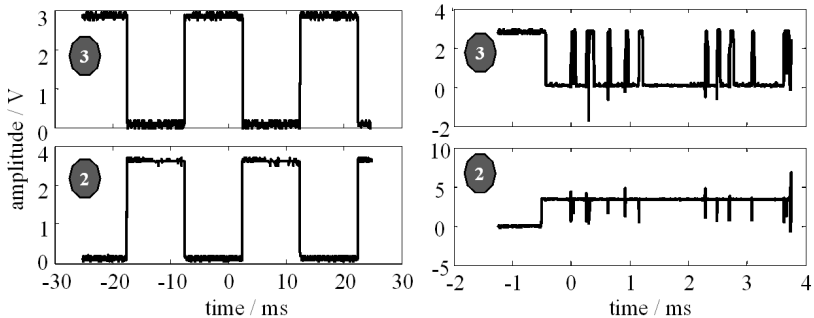


Figure 8.5: Error-free (left) and disturbed (right) optocoupler signals.

Disturbances at the input and the resulting error at the output of *OP1* are shown in Figure 8.6. In the left plot, the input signal is having its negative half wave. A narrow pulse with amplitude smaller than 300 mV even leads to a notch of the ‘high’ level at the output. However, an impulsive noise with amplitude over 1.5 V locating at the positive half wave does little harm to the ‘low’ level signal. This interesting phenomenon can be explained by the gain of *OP1*. As shown in Figure 8.2, *OP1* works in its open loop mode, the gain can easily exceed several thou-

sand. With this large gain factor, a noise voltage of about 100 mV drives *OP1* to saturation very quickly. The output signal turns on the input diode of the optocoupler and is clipped to ‘low’ level. The positive half wave is clipped to about 0.8 V by diode *D1* at the input of *OP1*. Again, *OP1* is driven to saturation and turns on the input stage of the optocoupler. Additive noises contributing to larger amplitude of the input signal does not change the saturation state of *OP1*, so the output signal stays still low and leading to no error. However, as soon as the input signal is dropped down to small enough by noises, the output could also change from ‘low’ level to ‘high.’

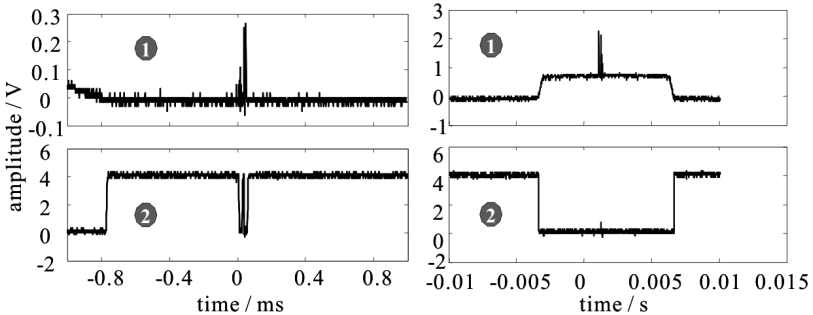


Figure 8.6: Noise at input and output of OP1.

From the analysis, we see that although an operational amplifier working as a comparator makes the ZC detection simple and low cost, its open-loop gain makes it extremely sensitive to additive noises locating at the negative half wave of mains voltage.

The burst errors shown in the right plot in Figure 8.6 can cause fatal error of a communication system. An effective method to ease the impact of these burst error is to utilize a mask window: as soon as a ZC is detected the detector output is ignored until the next ZC is about to come. In this way, the burst errors are blocked out and cannot harm the synchronization. However, a detection error can still occur when the noise appears shortly before a ZC. For modulation methods that are insensitive to phase errors, such as frequency-shift-keying (FSK) or amplitude-shift-keying (ASK) the tiny detection errors can be tolerable. For systems that are based on phase-shift-keying (PSK) or a measurement system which is

to investigate the phase response of a PLC channel, a more sophisticated and accurate detection strategy has to be developed. In following part, a least-squares-estimation based ZC detection will be discussed.

4 Proposed ZC detection method

First the conceptual design of our proposed detection method is presented. And a system block diagram is introduced to achieve an overview. The detailed information is given for the relevant parts, for example, the selection of estimation input slice, the two-step LS estimation algorithm, the detection of frequency and the prediction of new ZC.

4.1 Conceptual design

The conceptual design is shown in Figure 8.7. A voltage divider composed of $R1$ and $R2$ scales the mains voltage from over 230 V down to 5 V. A differential amplifier with high common voltage rejection will be used as an isolator. On one hand, it has high input impedance isolating $R2$ from internal circuit; on the other hand, the ground of low voltage side is also separated from neural wire of mains. The isolator output is filtered by a low pass filter to avoid aliasing effect, and then sampled by an analog/digital converter (ADC). The converted samples are feed in the FPGA, where estimations for different frequencies, a frequency detection, and a prediction of zero crossing are performed.

4.2 Estimation input slice

The first consideration concerns the estimation input: how many samples and which samples should be used for estimation. The size of sampled slice should be smaller than a period of mains voltage, so that the next ZC point of mains voltage can be predicted prior to its appearance. However, the accuracy and robustness of LS algorithm benefits from increased slice size. Since the power system can have a frequency up to 57.5 Hz when the power generation exceeds the sum of loads plus losses, the window size should be smaller than 17.39 ms. So we set the window size to 17.13 ms in the following discussion.

We will use Figure 8.8 to explain how to choose input slices. The first three slices right after system power-on are denoted by S_1 , through S_3 .

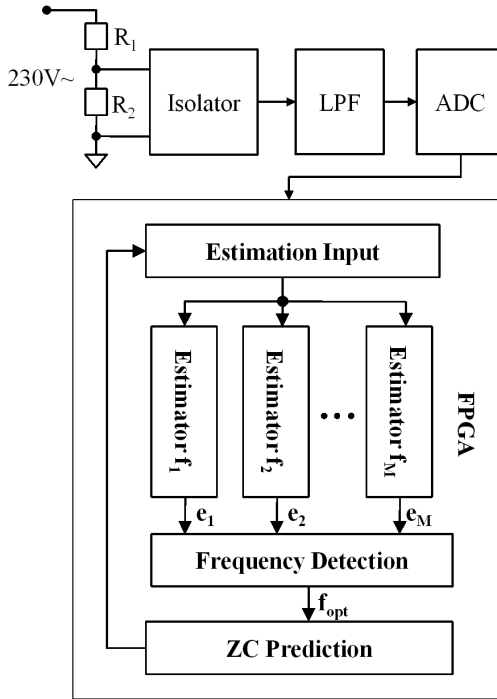


Figure 8.7: Conceptual design of ZC detector.

Since the system could be turned on at any time, the possibility that S_1 starts with a zero crossing is very small. We assume a start point other than ZC for S_1 to make the situation more realistic. The estimation with respect to S_1 should be finished between the slice end at t_1 and the rising edge of next ZC at t_2 . With the help of estimated phase and frequency, the next ZC rising edge can be predicted to be at t_2 . At t_2 the system begins to buffer the second slice S_2 for the estimation function. Again the estimation of phase and frequency values should be finished as quickly as possible and the next ZC rising edge is predicted to be at t_4 , and so on. In this way, ZC's can be predicted within a mains period.

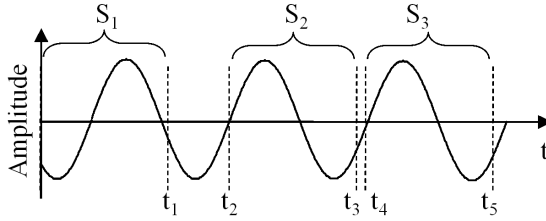


Figure 8.8: Choose input slices.

5 Estimator

An estimator bank shown in Figure 8.7 estimates the amplitude and phase of the sampled signal slice. It covers a frequency range from 42.5 to 57.5 Hz with a resolution of 0.5 Hz. Each estimation is based on a two-step LS algorithm. At the first step, the amplitude and instantaneous phase of the signal slice are evaluated. Since the input slice could be superimposed by additive impulsive noise which could lead to estimation errors. Therefore the parameter should not be used to predict ZCs. A sine wave is reconstructed with the help of estimated parameters and used to detect as well as eliminate the noise if there is any. The parameters of the conditioned signal are estimated. Since the noises are filtered, the estimation results must have a better accuracy. The following parts will introduce the details step by step.

5.1 LS estimation

We model the input signal $y(t)$ as a sinusoidal signal superimposed by additive noise

$$y(t) = A \sin(\omega t + \varphi) + n(t) \quad (8.1)$$

where A , ω , φ are amplitude, angular frequency and phase respectively. According to the sum formulas, we get

$$y(t) = a_1 \sin(\omega t) + a_2 \cos(\omega t) + n(t) \quad (8.2)$$

where $a_1 = A \cos(\varphi)$, $a_2 = A \sin(\varphi)$. Since the input slice is a 1-D array of size N , we can rewrite the equation in a matrix form

$$\begin{pmatrix} y(t_1) \\ y(t_2) \\ \vdots \\ y(t_N) \end{pmatrix} = \begin{pmatrix} \sin(\omega t_1) & \cos(\omega t_1) \\ \sin(\omega t_2) & \cos(\omega t_2) \\ \vdots & \vdots \\ \sin(\omega t_N) & \cos(\omega t_N) \end{pmatrix} \cdot \begin{pmatrix} a_1 \\ a_2 \end{pmatrix} + \begin{pmatrix} n(t_1) \\ n(t_2) \\ \vdots \\ n(t_N) \end{pmatrix} \quad (8.3)$$

or

$$\underline{y} = \underline{H}\underline{a} + \underline{n}.$$

This model is an overdetermined linear system with parameter vector \underline{a} since the number of equations N is larger than the number of parameters. In these systems, a model is proven the best approximation of the measured data if the sum of squared differences between the values derived by the model and the measured data reaches its minimum. And the parameters of the model can be obtained with the help of the formulas:

$$\underline{a} = (\underline{H}^T \underline{H})^{-1} \underline{H}^T \underline{y} \quad (8.4)$$

A and φ can be obtained by

$$A = \sqrt{(a_1)^2 + (a_2)^2} \quad (8.5)$$

$$\varphi = \arctan\left(\frac{a_2}{a_1}\right). \quad (8.6)$$

5.2 First estimation

As mentioned before, LS estimation is applied to the signal slice. The estimated parameters are used to reconstruct a sinusoidal signal of the same frequency. Figure 8.9 shows an example of disturbed signal slice (dashed line). The mains voltage is scaled to 4 V peak to peak, infested by a transient that has a peak-to-peak voltage over 13 V and a pulse width of about 2 ms. The reconstructed s is shown in solid line. Due to the interference, the amplitude is overestimated by 5.3%, and the estimation error of phase causes a jitter of 100 μ s. The estimated inaccuracy can be

exacerbated by larger, more intensive noises. Furthermore, the position of these noises can also degrade the estimation result. To guarantee a reliable prediction of ZC, the transients must be detected and eliminated first.

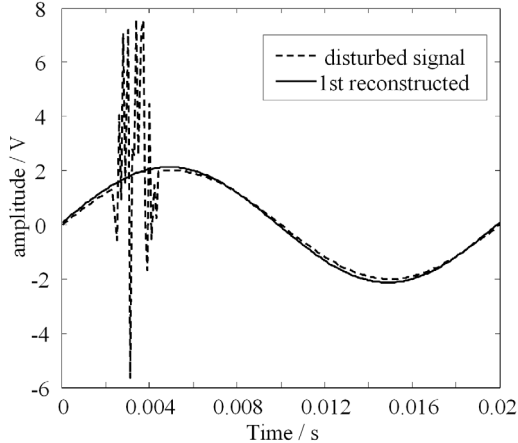


Figure 8.9: Original and reconstructed signals after the first estimation.

5.3 Signal conditioning and second estimation

Although the reconstructed signal shown in Figure 8.9 is not suitable for the prediction of ZC due to the amplitude and phase errors, it can still be used to detect the transient noise. The difference between the original signal slice and its reconstructed counterpart is mostly characterized by the large transient. The conditioned signal can be expressed as follows:

$$y_c(t) = \begin{cases} x(t) & |x(t) - y_r(t)| \leq L_{TH} \\ y_r(t) & \text{else} \end{cases}$$

where $x(t)$, $y_r(t)$ are the original and the reconstructed signals respectively, and L_{TH} is a threshold of 0.2 V. The left plot in Figure 8.10 shows the conditioned signal $y_c(t)$. Although there are still protuberances, the noise is largely eliminated. The second estimation follows the same step

as the first one, the only difference is that it takes the conditioned signal as its input. As a result, the amplitude error reduces to 0.14%, and the phase error to $3.5\mu\text{s}$. The estimation accuracy is largely improved through the signal conditioning and the two-step LS estimation.

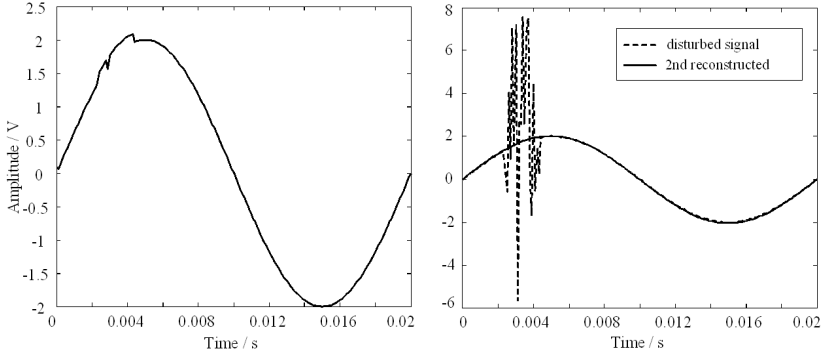


Figure 8.10: Conditioned signal (left) and reconstructed signals after the second estimation (right).

5.4 Frequency detection and ZC prediction

The mains frequency depends largely on the total generation and the sum of collective loads plus losses. If both values are equal, the frequency stays constant. Otherwise the frequency decreases if total generation cannot cover the sum of loads and losses, and increases if there is overplus of the generated power [8]. Although many efforts are taken to maintain the frequency of power system to its nominal frequency, for example, the utilization of underfrequency and overfrequency relays, the mains voltage still has its frequency varying between 47 and 52 Hz if the mains is connected to central network synchronously. The variation might fall between 42.5 and 57.5 Hz if mains is not synchronized to central network [9], which also leads to estimation and prediction errors. After the signal conditioning and the second estimation, the degradation caused by additive noise is largely reduced, and the remaining estimation error is mostly contributed by the frequency deviation.

The error vector

$$\underline{e} = \left| \underline{I} - \underline{H}(\underline{H}^T \underline{H})^{-1} \underline{H}^T \right| \underline{y} \quad (8.7)$$

measures the difference deviation between measured and reconstructed signal. The sum of squared error

$$SSE = \sum_{i=1}^N e(i)^2 \quad (8.8)$$

is often used to describe the quality of LS estimations. The frequency at which SSE has minimum value is considered to be the optimal frequency. Figure 8.11 gives an example of the detection result. The test signal has a frequency of 50 Hz. And the calculated SSE's vary between 0.2 and 63. We choose the segment between 48 and 52 Hz to achieve a better view of SSE near optimal frequency. The minimum SSE value is observed right at 50 Hz.

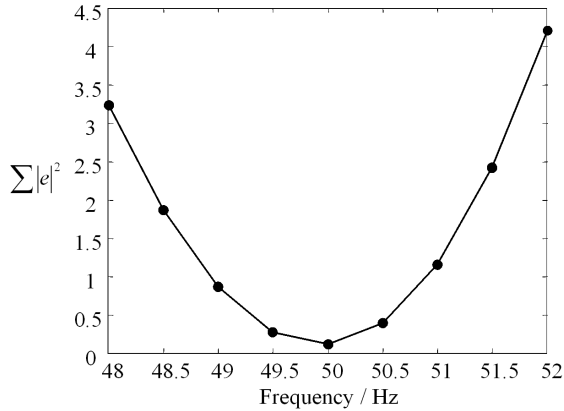


Figure 8.11: SSE of LS estimations for different frequencies.

5.5 Computer simulation results

The proposed conception is verified with simulations. As input signal we generated 9 periods of sine waveforms, shown in Figure 8.12. To

investigate the frequency detection, we changed the frequency between 48 and 52 Hz. Superimposed impulsive noises are added, whose amplitude and pulse width are allocated randomly. The impulses are so positioned that each period of sine wave has been interfered by at least one impulse. As shown in Figure 8.12, the original signal is well reconstructed, the predicted ZCs agree with the real ZCs, and frequencies 50, 51, 52, 49, 48, 49, 49, 51 and 50 Hz predefined for period 1 through 9 respectively are also detected successfully.

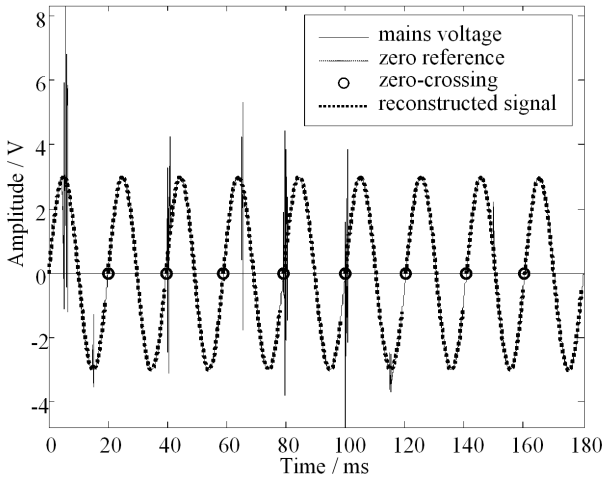


Figure 8.12: Mains voltage superimposed by impulsive noises and reconstructed signal.

6 Conclusion

In this paper, we discussed several methods of synchronization for PLC systems; we also studied the simple ZC detector circuit and analyzed the burst errors. As mentioned before, it can provide satisfactory synchronization for PLC systems by applying sophisticated digital filtering. For the AMS we proposed a LS estimation-based ZC detection strategy. The system conception is introduced, and the estimation and detection algorithms are discussed. Based on the conducted studies conclusions with

respect to the proposed ZC prediction method can be drawn that it is robust against large transients existing in common power line channels; its ability of detecting, locating and extracting large impulsive noises can be used to capture and analyze transient noises; it can predict a new ZC within one mains period, suitable for ZC-based global synchronization and other real-time applications; it can also track change of mains frequency as well as fluctuation of amplitude, providing quality information of power transmission system. Although the method is computationally intensive, it is mainly based on multiplications and accumulations which can be implemented in ordinary digital signal processors (DSPs) or field programmable arrays (FPGA) without many efforts.

References

1. J. Bausch, T. Kistner, M. Babic, and K. Dostert, "Characteristics of indoor power line channels in the frequency range 50–500 kHz," *IEEE Int. Symp. on Power Line Communication and its Applications*, 2006.
2. T. Schmidl and D. Cox, "Robust frequency and timing synchronization for OFDM," *IEEE Trans. Commun.*, 1997.
3. H. Minn, M. Zeng, and V. K. Bhargava, "On timing offset estimation for OFDM systems," *IEEE Commun. Lett.*, vol. 4, pp. 242–244, 2000.
4. J. Proakis, *Digital Communications*. New York; McGraw-Hill, 2001.
5. K. Dostert, *Powerline Communications*. Upper Saddle River: Prentice Hall, 2001.
6. T. Kistner, M. Bauer, A. Hetzer, and K. Dostert, "Analysis of Zero Crossing Synchronization for OFDM-Based AMR Systems," *IEEE Internal Symposium on Power Line Communication and its Applications*, 2008.
7. T. Kistner, "Neuartiges mehrträgerbasiertes PLC-System mit störresistenter Synchronisation," Ph.D. dissertation, University of Karlsruhe, 2008.
8. T. S. Sidhu, "Accurate measurement of power system frequency using a digital signal processing technique," *IEEE Trans. Instrum. Meas.*, vol. 48, 1999.
9. *DIN EN 50160, Voltage characteristics of electricity supplied by public distribution systems; German version prEN 50160:2005*.

Information fusion for environment exploration

Michael Heizmann,¹ Ioana Gheța,² Fernando Puente León,³
and Jürgen Beyerer^{1,2}

¹ Fraunhofer Institute of Optronics, System Technologies and Image
Exploitation IOSB, Fraunhoferstr. 1, D-76131 Karlsruhe

² Karlsruhe Institute of Technology, Institute for Anthropomatics,
Vision and Fusion Laboratory (IES), Adenauerring 4, D-76131 Karlsruhe

³ Karlsruhe Institute of Technology, Institute of Industrial Information
Technology, Hertzstr. 16, D-76187 Karlsruhe

Abstract Perception and task-specific interpretation of dynamic environments represent key components of forthcoming intelligent systems. To master these abilities, methods are required that are capable of extracting relevant information from signals and combining them adequately to construct a semantically enriched model of the scene of interest. This contribution focusses on two aspects of this task. On the one hand, a method is presented to make an optimal selection from the available input data. On the other hand, an object-oriented environment model is proposed that enables a continual fusion of available knowledge with new sensor information and combines this with a memory model. All methods are based on Bayesian statistics in an objective degree-of-belief (DoB) interpretation. The application areas of these approaches are demonstrated with humanoid robots and autonomous vehicles.

1 Introduction

In the last years, autonomous technical systems have become part of many domains of everyday life: They are not limited to special environments anymore, as is the case in surveillance, manufacturing or remote sensing applications. Rather, they increasingly take part in human assistance and care, cleaning, construction, agriculture, freight traffic,

individual transportation, rescue and disaster scenarios as well as in entertainment. Many additional applications are under development.

A point that many applications have in common is that the environment is both dynamic and a priori unknown. Such an environment has to be sensed and “understood” to enable an interaction with it or to navigate safely within it.

One can guess that environment perception and interpretation represents one of the biggest challenges to solve such tasks. To enable an inference about a three-dimensional environment, typically several heterogeneous sensors are used to collect information—e.g., in the form of images, acoustic signals or geometric measurement results. Consequently, methods are needed to extract relevant features from the signals and classify them reliably. Moreover, relations between the recognized objects⁴ have to be registered and fused to a situation picture. In general, the environment is dynamic. Thus, to enable a reliable prediction of the intention of the “characters” or entities involved in the scene, an estimate of their state vector is required.

The present contribution deals with methods to sense and describe dynamic environments for technical autonomous systems equipped with multiple sensors. Thereby, we focus on two important components of the information processing chain:

- In the following section, we assume that both sufficient sensors and analysis methods are available, and that a selection of the most promising ones is to be accomplished, such that the input data are optimal given the available resources.
- Section 3 presents an object-oriented environment model suitable for environment representation. It features not only methods to describe the entities in the environment together with their attributes and mutual relations, but also mechanisms to gradually refine this description with increasingly available sensor data as well as a simple memory model for the situation picture.

The common theoretical foundation of these two components is Bayesian statistics, by means of which the knowledge about the involved quantities is expressed objectively in terms of degree of belief. In Section 4, two

⁴ To distinguish between actually existing objects and objects of an object-oriented model, actually existing objects are referred to in the following as “entities.”

application scenarios of the presented methods are discussed exemplarily. For other aspects of technical cognition, which cannot be covered in this contribution, we refer, e.g., to the research activities of the DFG Clusters of Excellence ‘‘Cognition for Technical Systems’’ in Munich [1] as well as ‘‘Cognitive Interaction Technology’’ in Bielefeld [2].

2 A Bayesian selection method for sensor systems

When solving tasks of information acquisition, the question of choosing the most suitable sensor systems often arises. Considering that a set of sensor systems and evaluation strategies (in the following referred to as information channels) is available, the most suitable information channel or a combination of them must be found such that their abilities are optimally exploited with regard to the specific task. This contribution proposes a methodology for obtaining an optimal choice based on Bayesian statistics in a objective degree-of-belief (DoB) interpretation.

First, the task-relevant properties, i.e., the target quantities, are combined to a vector \mathbf{z} , $\dim(\mathbf{z}) := \mathcal{Z}$. The task-relevant knowledge can be described in a probabilistic way in form of probability distributions⁵ $\mathbf{p}(\mathbf{z}) := (p(z_1), \dots, p(z_{\mathcal{Z}}))^T$ over the definition domains \mathcal{Z}_i , $i = 1, \dots, \mathcal{Z}$ of the properties of interest.

The task-specific interest regarding the target quantities \mathbf{z} is modeled using an interest vector \mathbf{w} , $\dim(\mathbf{w}) = \dim(\mathbf{z})$, $w_i \in \{0, 1\}$. The interest can then be represented by the probability distributions $\mathbf{p}(\mathbf{w}) := (p(w_1), \dots, p(w_{\mathcal{Z}}))^T$. These picture the knowledge demand or reconnaissance demand regarding the properties z_i . The value $p(w_i = 1) = 1 - p(w_i = 0)$ represents the interest in the target quantity z_i in the form of a DoB.

Following, the information channels are defined, and their contributions to the determination of the target quantities are modeled. To this purpose, the vector of information channels \mathbf{m} , $\dim(\mathbf{m}) := \mathcal{M}$, is used. This modeling approach includes all steps for the determination of the target quantities starting from the acquisition of sensor data until their evaluation yielding one or more target quantities.

⁵ The symbol $p(\cdot)$ stands for probability distribution functions for the case of continuous quantities as well as for probability mass functions in the discrete case.

The use of an information channel is modeled by means of the distributions $\mathbf{p}(\mathbf{m}) := (p(m_1), \dots, p(m_{\mathcal{M}}))^T$, where the value for $p(m_i = 1)$, $\sum_{i=1}^{\mathcal{M}} p(m_i = 1) = 1$, describes the contribution of this information channel for solving the task. Finally, sensor data is defined as a vector \mathbf{d} with $\dim(\mathbf{d}) = \dim(\mathbf{m})$.

Based on this modeling approach, the following questions can be answered:

- Which optimal combination of information channels $\mathbf{p}_{\text{opt}}(\mathbf{m})$ has to be chosen in order to satisfy the knowledge demand \mathbf{w} regarding the target quantities \mathbf{z} ?
- How can the target quantities $\hat{\mathbf{z}}$ be estimated, if an optimal combination of information channels $\mathbf{p}_{\text{sel}}(\mathbf{m})$ or a combination deduced from the optimal one is chosen?
- How can the selection method for the information channels be extended, if the target quantities are to be determined iteratively, e.g., if the knowledge demand changes with time or the target quantities are dynamic?

Choice of optimal information channels Given the previous knowledge about the target quantities as prior distributions $p(z_{i,0})$ and the respective knowledge demand, the determination of the optimal combination of information channels $\mathbf{p}_{\text{opt}}(\mathbf{m})$ is needed. By means of a Bayesian formalism, the problem can be formulated as task of the determination of the posterior distributions:

$$p(m_j | w_i, z_{i,0}) = \frac{p(w_i, z_{i,0} | m_j) \cdot p(m_j)}{p(w_i, z_{i,0})} = \frac{p(w_i | z_{i,0}, m_j) \cdot p(z_{i,0} | m_j) \cdot p(m_j)}{p(w_i, z_{i,0})} \quad (9.1)$$

with $i = 1, \dots, \mathcal{Z}$, $j = 1, \dots, \mathcal{M}$.

A distribution $p(w_i | z_{i,0}, m_j)$ models the knowledge demand about a target quantity (w_i) in case that previous knowledge ($z_{i,0}$) is given and an information channel (m_j) is employed. Since the knowledge demand is independent of the employed information channels, the distribution can be simplified to $p(w_i | z_{i,0}, m_j) = p(w_i | z_{i,0})$. The knowledge demand depending on the existing previous knowledge can now be constituted

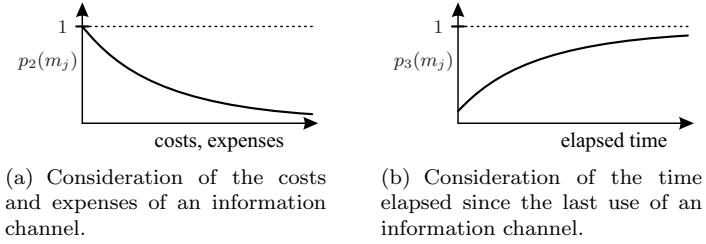


Figure 9.1: Modeling of the applicability of an information channel.

to:

$$p(w_i|z_{i,0}) \propto H(z_{i,0}) \cdot p_1(w_i), \quad (9.2)$$

where $H(z_{i,0})$ is the entropy of the distribution $p(z_{i,0})$ describing the lack of knowledge about z_i . $p_1(w_i)$ specifies the a priori existing knowledge demand about z_i .

The distribution $p(z_{i,0}|m_j)$ represents the contribution of information which can be delivered by an information channel (m_j) regarding a target quantity (z_i). This contribution is a property of the information channel and not of the a priori existent knowledge:

$$p(z_{i,0}|m_j) = p(z_i|m_j). \quad (9.3)$$

Using this distribution, the information quality an information channel is able to deliver regarding a target quantity can be modeled.

The distribution $p(m_j)$ describes features of the information channel m_j which are independent of a specific task. In terms of the Bayesian formalism, $p(m_j)$ can be interpreted as a prior distribution. This distribution can be used, e.g., to model the costs which are connected with the use of an information channel. A possible modeling is given by the following distribution:

$$p(m_j) \propto p_2(m_j) \cdot p_3(m_j), \quad (9.4)$$

where $p_2(m_j)$ describes the costs and expenses caused by the information channel and $p_3(m_j)$ evaluates the elapsed time since the last use of the channel. Figure 9.1 shows possible distributions for $p_2(m_j)$ and

$p_3(m_j)$. The exponentially decreasing function for $p_2(m_j)$ reduces the weight of an information channel with increasing expenses for the information acquisition and processing. The course of $p_3(m_j)$ starting from a small value and increasing with elapsed time guarantees that different information channels are considered sequentially in time.

The choice of the optimal information channel can now be accomplished by summing over the dimension \mathcal{Z} of the vector of the target quantities:

$$\mathbf{p}_{\text{opt}}(\mathbf{m}) = (p_{\text{opt}}(m_1), \dots, p_{\text{opt}}(m_{\mathcal{M}}))^{\text{T}} \quad \text{with} \quad (9.5)$$

$$p_{\text{opt}}(m_j) := \lambda \sum_{i=1}^{\mathcal{Z}} p(m_j | w_i, z_{i,0}). \quad (9.6)$$

Neglecting the denominator of Eq. (9.1), the choice of an appropriate constant λ ensures that the normalization constraint $\sum_{j=1}^{\mathcal{M}} p_{\text{opt}}(m_j = 1) = 1$ is kept.

If not all possible information channels can be employed, e.g., due to a lack of resources or temporal constraints, their use can be prioritized according to their DoBs $p_{\text{opt}}(m_j = 1)$. This way, the optimal choice of information channels with respect to the task and the previous knowledge at hand can be assured. As an example, considering the list $p_{\text{opt}}(m_{(k)} = 1)$ sorted in descending order, the first $N < \mathcal{M}$ information channels may be chosen. The contributions of the selected information channels are then given by:

$$p_{\text{sel}}(m_{(k)}) := \kappa \cdot p_{\text{opt}}(m_{(k)}), \quad (9.7)$$

where the constant κ guarantees again that the normalization constraint $\sum_{k=1}^N p_{\text{sel}}(m_{(k)} = 1) = 1$ holds.

Estimation of the target quantities Once the selected information channels have been employed, the requested target quantities can be obtained by weighted superposition of the posterior distributions $p(z_i | d_j)$ specific to the respective channels and target quantities:

$$p(z_i) := \sum_{k=1}^N p_{\text{sel}}(m_{(k)} = 1) \cdot p(z_i | d_{(k)}). \quad (9.8)$$

Iterative approach The proposed methodology for the selection of information channels and for determining the target quantities can be implemented in an iterative manner. For this purpose, both presented steps must be accomplished alternately. The first step consists in the determination of the optimal selection of information channels (see Eq. (9.1)):

$$p(m_j^t | w_i^t, z_i^{t-1}) = \frac{p(w_i^t | z_i^{t-1}, m_j^t) \cdot p(z_i^{t-1} | m_j^t) \cdot p(m_j^t)}{p(w_i^t, z_i^{t-1})}, \quad (9.9)$$

where the index $t \in \mathbb{N}$ defines the iteration step and z_i^{t-1} represents the knowledge obtained until the preceding iteration step. According to the procedure presented above, the contributions of the information channels are modeled by $p_{\text{sel}}(m_{(k)}^t)$. In the second step, the target quantities are determined according to Eq. (9.8):

$$p(z_i^t) := \sum_{k=1}^N p_{\text{sel}}(m_{(k)}^t = 1) \cdot p(z_i^t | d_{(k)}^t). \quad (9.10)$$

3 Environment modeling

Many systems acquiring information with the purpose of interacting with their environment require a storage in addition to their sensors and information channels. The storage saves the acquired information and provides it for other cognitive components on demand. That way, the information storage acts like a memory, incorporating a time-dependent model of the environment. An example of such a system is an autonomous humanoid robot, which is designed to help humans in housekeeping, see Sect. 4.1. Thus, the autonomous system has the possibility of obtaining a permanent and complete overview of the ongoing events in its relevant environment. Together with other cognitive processes, such as inference and prediction, this approach is known as providing *situation awareness* [3].

A storage with the mentioned properties can be established by means of a dynamic and object-oriented environment modeling approach. The environment model can be compared with a Lego landscape, where the Lego bricks compose virtual substitutes (*instances*) of real objects and

persons (*entities*). In the virtual environment, the entities of the real world object types and persons are represented by instances of classes, see Fig. 9.2.

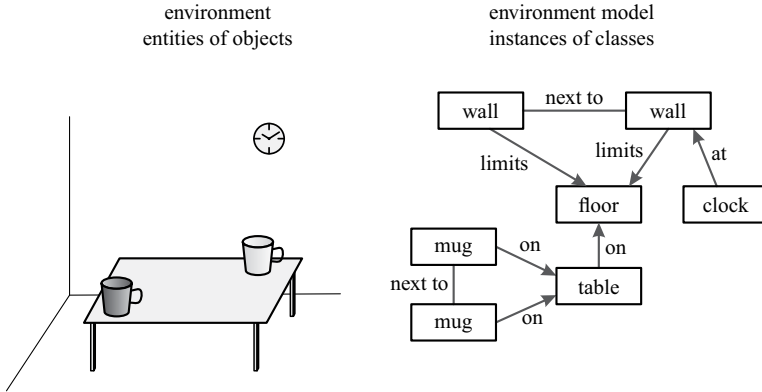


Figure 9.2: Connection between the real world and the environment model.

The properties and relations of the entities are detected by sensors and consecutively assigned to instances as attributes and relations. To simplify the following presentation, attributes and relations of the instances in the environment model are called information. They correspond to the target properties introduced in Sect. 2.

The environment model which will be introduced in Sect. 3.1 is the core of the environment modeling approach. In addition, the modeling approach comprises mechanisms for information modification based on sensor and other information, see Sects. 3.3 and 3.4.

3.1 Object-oriented environment model

The proposed approach for environment modeling is object-oriented and provides all information in the environment model with a respective uncertainty and an acquisition time. As a consequence, the model represents the relevant part of the environment of the system at a certain point in time.

Entities have context-dependent properties such as position, size, color, etc., which are mapped to the respective attributes of instances. Classes

in the environment model are therefore also context-dependent and defined in accordance to the present task.

The basic unit of the environment model is the simple class of *blank objects*, which only has the *existence* as compulsory attribute. Instances of this class are placeholders for unknown information. For example, a blank object can be used to mark a spatial area as being occupied for preventing collisions. In this case, only the attribute *position* is necessary in addition to the *existence*. If a classification of the respective entity is made, instances of blank objects may be replaced by instances of more detailed classes. The new instance receives at least the class attribute *type* in addition. Depending on the new class, several other attributes may be added to the instance. Furthermore, blank objects can be used to specify abstract information, e.g., sounds coming from an unidentified source.

Relations between entities are also provided with uncertainties and are handled in the environment model in a similar way as attributes.

3.2 Modeling of uncertainties

Each information (attribute or relation) is saved in the environment model along with its uncertainty, allowing the quantification of the information quality. There are two types of information that contribute to the environment model: sensor information, which is dynamically acquired by the system (e.g., by exploration), and prior information, which is equivalent to the previous knowledge the system is provided with (e.g., an environment map). Sensor information is generally characterized by its observation uncertainty. Prior information is mostly acquired by means of external sensors or is used as additional knowledge (e.g., knowledge on the attributes of classes).

Uncertainties may be expressed in different ways:

- First, the information on a quantity (attribute or relation) can be given parametrically in form of the most probable value and a respective variance parameter. An example is given by the following statement: “The entity A has the most probable height z_0 with the variance σ_z^2 .” The advantage of this modality of expressing uncertainty is the compactness of the specified parameters.
- The uncertainty of a single quantity may be specified comprehen-

sively by a probability distribution over the domain of all possible values of the quantity, e.g., for the above example of a height specification, the uncertainty can be given by $p(z)$. If the uncertainty is given parametrically by means of the most probable value and the variance, then the corresponding probability distribution can be uniquely determined using the maximum entropy principle [4,5]. For the previous example, the result would be the normal distribution $\mathcal{N}(z_0; \sigma_z)$.

- The uncertainty of several quantities may be specified at first by considering the properties to be independent. For that, parametrical models (e.g., for two position coordinates, this would be $\mathcal{N}((x_0, y_0), (\sigma_x, \sigma_y))$), or independent marginal distributions ($p(x, y) = p(x) \cdot p(y)$) can be used.
- A comprehensive way of expressing the joint uncertainty of several quantities is given by specifying the joint distribution, e.g., $p(x, y)$. The explicit specification of joint distributions has the disadvantage of being resource intensive: for all value combinations of the considered quantities, the probabilities have to be determined and stored.

Besides a frequentistic interpretation used in statistics, the probabilistic specification of uncertainty offers the opportunity of interpreting probability as degree of belief (DoB) in a Bayesian sense [6–8]. The DoB formalism has the following advantages:

- Uncertainties can be expressed consistently: all possibilities for specifying uncertainty can be converted into an analogous DoB representation by using the maximum entropy principle.
- Differently scaled attributes and relations can be handled consistently: probability distributions can be modeled on basis of all possible scales (i.e., nominal, ordinal, interval, ratio and absolute scale) [7].
- Both subjective and objective information can be quantified in a similar way [9].
- For the handling of information, well-proven Bayesian fusion mechanisms can be applied [8].
- Inconsistencies can easily be handled within the Bayesian formalism. Contradictory information with respective uncertainties in

form of DoB distributions can be fused, whereas in the case of other strict fusion formalisms, the straightforward fusion of information is not possible.

As an example, the observation of two cylindrical instances A and B with diameters of 10 cm placed 1 mm apart from each other would lead to a contradiction (two objects cannot overlap), if a strict formalism is applied. By use of a DoB formalism, the observation can be modeled with an observation uncertainty expressed for example by means of variances $(\sigma_x, \sigma_y) = (1 \text{ cm}, 1 \text{ cm})$. In this case, the interpretation of the two instances belonging to the same entity is made possible.

3.3 Bayesian propagation

The environment model reflects the relevant part of the system environment at a certain point in time. As a result of changes in the environment and other new information, the environment model must be modified over time. The modeling of the changes is accomplished by means of Bayesian fusion methods, which propagate the DoB distributions from a point in time t_{i-1} to the next point in time t_i . Modifications of the environment model may originate from two sources: new sensor information is acquired and must be incorporated into the model, and existent information ages. In the next sections, some of the propagation mechanisms are described in detail using the example of the *existence*. For other attributes and relations, analogous procedures are applied.

Instantiation In case that new information about entities and their attributes and relations, which does not have an equivalent in the environment model (i.e., there is no instance representing the observed entity), is observed, an instance of the respective class is created and inserted in the model. The decision regarding the instantiation is made on basis of a posterior DoB for the respective information. In case of the attribute *existence*, the decision means the creation of a new instance. For other attributes and relations, the respective information is assigned to the appropriate existing instance.

Starting from the existence probability $p(O = o)$, i.e., the probability that an entity exists in the real world, and the probability $p(O = \bar{o}) =$

$1 - p(O = o)$ that the entity does not exist, the following conditional DoBs can be defined [10]:

- The conditional probability $p(D = o|O = o) = p_E$ describes the probability of a *hit*, i.e., the entity exists and is observed.
- The conditional probability $p(D = \bar{o}|O = o) = 1 - p_E$ describes the probability of a *miss*, i.e., the entity exists, but it is not observed.
- The conditional probability $p(D = o|O = \bar{o}) = p_F$ describes the probability of a *false alarm*, i.e., an entity does not exist, but an observation is made.
- The conditional probability $p(D = \bar{o}|O = \bar{o}) = 1 - p_F$ describes the probability of a *correct rejection*, i.e., no entity exists and no observation is made.

The combination of the probabilities of the existence and of the observation leads to four possibilities, see Fig. 9.3. If the posterior DoB for the existence of an entity exceeds a given instantiation threshold γ_i , a new instance is created and inserted in the environment model:

$$\begin{aligned}
 p(O = o|D = o) &= \frac{p(D = o|O = o) \cdot p(O = o)}{p(D = o)} \\
 &= \frac{1}{1 + \frac{1-p(o)}{p(o)} \frac{p_F}{p_E}} > \gamma_i.
 \end{aligned}
 \tag{9.11}$$

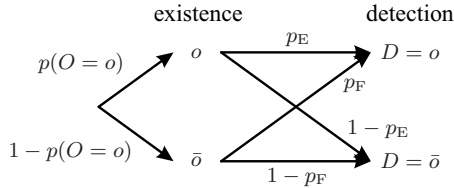


Figure 9.3: Schematic dependencies between the existence and observation of entities.

Propagation through aging The transition of the environment model from one point in time t_{i-1} to the next point in time t_i (with $t_i - t_{i-1} =$

$\Delta t = \text{const.}$) comprises an aging mechanism for the contained information. The aging models the fact that over time, the amount of knowledge about the real world decreases, i.e., the overall uncertainty increases. As a result, the propagation must be defined such that the existence probability decreases over time and the entropy of the DoB distribution of attributes and relations increases. An example of an aging model for the *existence* can be achieved by using an exponentially decreasing function:

$$p_{t_i}^-(O = o) := \beta \cdot p_{t_{i-1}}(O = o), \quad (9.12)$$

where $0 < \beta \leq 1$ is a class specific constant and $p_{t_i}^-(O = o)$ is the existence probability after the aging step. Transient information (e.g., the existence of an apple) is characterized by a small value of β , such that this information becomes uncertain in a little while. By contrast, persistent information (e.g., the existence of a cupboard) is provided with a higher value of β , such that the uncertainty increases more slowly.

Propagation with new acquired information In case that new sensor information having a correspondence in the environment model is available, the new information is fused with the existing information in consideration of their uncertainties.

The main idea of the fusion approach is to apply Bayesian fusion using the DoB distribution $p(O|D_{i-1}, \dots, D_0)$ based on the $i - 1$ preceding observations D_{i-1}, \dots, D_0 as prior and modeling the new information as likelihood function $p(D_i|O)$ [11, 12]:

$$\begin{aligned} p(O|D_i, \dots, D_0) &= \frac{p(D_i, \dots, D_0|O) \cdot p(O)}{p(D_i, \dots, D_0)} \\ &= \frac{p(D_i|O) \cdot p(O|D_{i-1}, \dots, D_0)}{p(D_i|D_{i-1}, \dots, D_0)}. \end{aligned} \quad (9.13)$$

$p(O)$ indicates the knowledge on the system prior to any observation. $p(D_i|D_{i-1}, \dots, D_0)$ is the probability that the i^{th} observation is made and has the role of a normalization factor.

For the propagation, the result of the aging step is used as prior DoB distribution. The observations D_{i-1}, \dots, D_0 are considered to be taken at the points in time t_{i-1}, \dots, t_0 . The new posterior DoB distribution is

then obtained as follows:

$$p_{t_i}(O) := p_{t_i}(O|D) = \frac{p(D_i|O) \cdot p_{t_i}^-(O)}{p(D_i|D_{i-1}, \dots, D_0)}. \quad (9.14)$$

Here, $p_{t_i}(O)$ is the desired posterior DoB distribution, and $p(D_i|O)$ describes the observation for the point in time t_i . $p_{t_i}^-(O)$ is the result of the aging step of Eq. (9.12) taking the role of the prior distribution for Bayesian fusion. $D = \{D_0, \dots, D_i\}$ summarizes the observations up to the point in time t_i .

If no new observation regarding the given information is made at the point in time t_i , the result of the propagation adopts the result of the aging step:

$$p_{t_i}(O) := p_{t_i}^-(O). \quad (9.15)$$

Deletion of information To keep the environment model efficient, outdated or very uncertain information must be deleted. The decision about the deletion of an instance is based on the DoB distribution of the *existence*. If the DoB for the existence is smaller than a given threshold, the instance is deleted from the environment model:

$$p_{t_i}(O) < \gamma_d, \quad (9.16)$$

where γ_d is the deletion threshold, and $\gamma_d < \gamma_i$. The DoB may drop under the given threshold because of aging (see Eq. (9.12)) or because of the fusion with new sensor information not confirming the existence of the respective entity (see Eq. (9.14)).

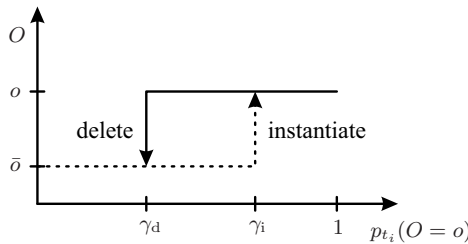


Figure 9.4: Hysteresis for the instantiation and the deletion of instances.

The difference between γ_i and γ_d is necessary to ensure a hysteresis: an instance should not be deleted immediately after it has been instantiated, see Fig. 9.4.

An additional threshold γ_r with $\gamma_d < \gamma_r < \gamma_i$ may be useful to explicitly trigger the reconfirmation of the existence of an entity. If an entity is not observed at random, the reconfirmation can be triggered intentionally before it is deleted due to the aging mechanism. The difference between γ_r and γ_i provides the system with a time buffer, during which the entity is considered to be existing without the need to reconfirm the existence. The time buffer is advantageous particularly in the case of transient information, since it prevents a permanent triggering of the sensors.

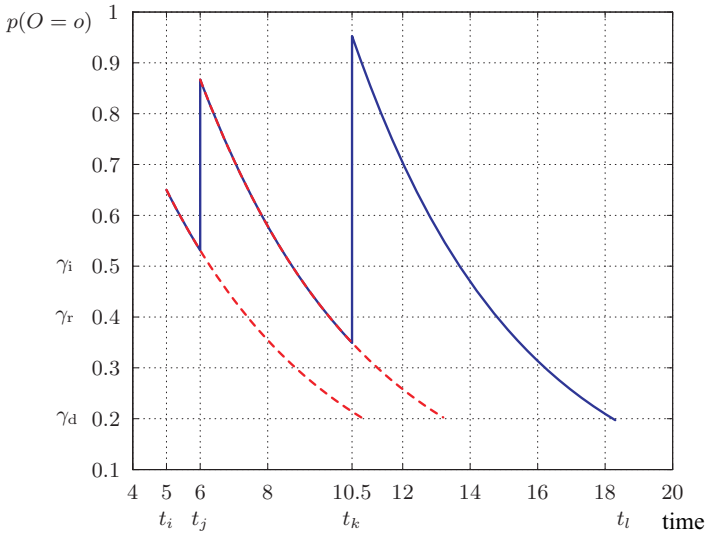


Figure 9.5: Example of the life cycle of an instance of a transient entity.

Figure 9.5 shows an example of the life cycle of an instance of a transient entity by means of the DoBs of its *existence* attribute. The dashed line describes the propagation resulting from the aging mechanism (see Eq. (9.12)), if no appropriate new sensor information is available. The continuous line describes the course of the DoBs, if the existence of the entity is reconfirmed at the points in time t_j and t_k by new observations.

In the end, no new sensor information is acquired and as a result, the DoB drops under the deletion threshold γ_d at the point in time t_l . The instance is then deleted from the environment model.

3.4 Abstraction levels

The information in the environment model is assigned to different abstraction levels. An instance which is described in detail by its class and the respective attributes and relations is situated on a low abstraction level. In contrast, an instance belonging to a class with few attributes and relations is considered on a high abstraction level. The most abstract information in the environment model is represented by blank objects, which only possess the *existence* attribute and have no other specified attributes, see Sect. 3.1. The instances of such blank objects are, therefore, situated on the highest abstraction level.

The abstraction level of an instance may change if new information is available: the more attributes and relations are specified about an instance, the lower its abstraction level is. Figure 9.6 represents the abstraction levels as a pyramid. On top of the pyramid, blank objects are situated. The lowest level is populated with detailed instances, the attributes and relations of which are completely specified.

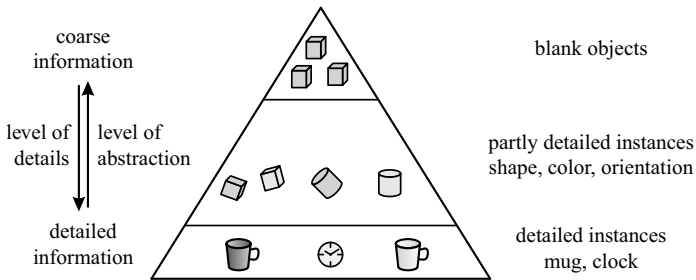


Figure 9.6: Abstraction levels in the environment model.

There is a second point of view on abstraction levels with regard to the information retrieval from the environment model: depending on the task, different degrees of detail of the retrieved information may be necessary. As an example, for path planning, it is sufficient to know the free space in the environment. Hence, only the attributes *position*

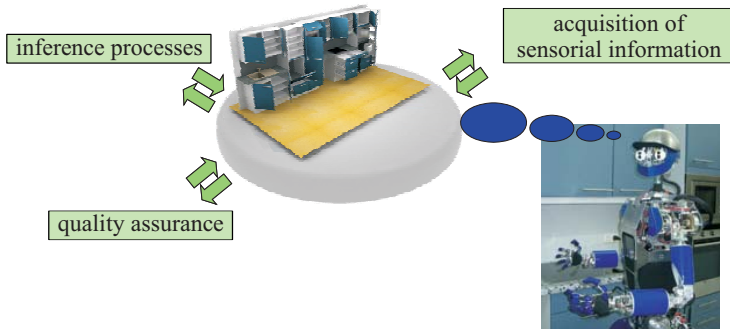


Figure 9.7: Application example of the environment model for the case of a humanoid robot.

and *extension* of the instances, which represent information on a high abstraction level, are required. By contrast, for a manipulation task, detailed information like *3D shape* or *grasp possibility* and relations like *is situated on* of the respective instance is necessary. This information is assigned to a low abstraction level.

4 Applications

4.1 Humanoid robots

Examples of systems which acquire information with the purpose of interacting with the environment are autonomous humanoid robots. Within the scope of the DFG Collaborative Research Center (*Sonderforschungsbereich*) SFB 588 “Humanoid Robots—Learning and Cooperating Multimodal Robots,” [13] humanoid robots are designed with the purpose of helping humans with housekeeping. To solve this task, the humanoid robot needs a comprehensive overview on the environment. To this end, the Bayesian selection method for sensor systems presented in Sect. 2 and the environment model introduced in Sect. 3 are applied. Details regarding the implementation of the conceptions in the context of humanoid robots are given in [14].

The environment model and its properties represent the core cognitive component of the humanoid robot. The model serves as an infor-

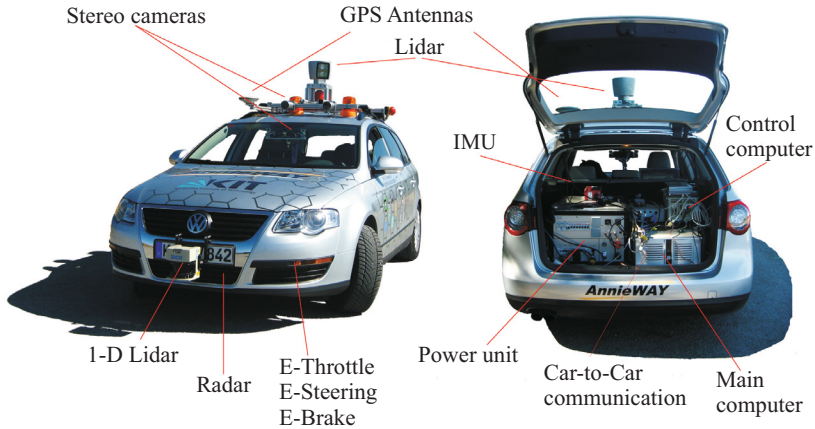


Figure 9.8: Autonomous car AnnieWAY (Source: Team AnnieWay [16]).

mation hub, where information acquired by the robot sensors is saved, propagated, and made available to other cognitive processes. As an example, inference processes, such as automatic path planning and exploration, retrieve the necessary information from the environment model, see Fig. 9.7.

4.2 Autonomous vehicles

In the area of autonomous vehicles, another DFG Collaborative Research Center is involved with environment perception and situation interpretation—the SFB/Transregio 28 “Cognitive Automobiles” [15]. An essential goal of this interdisciplinary center is to investigate machine cognition techniques for mobile systems as a foundation of “intelligent” behavior. Figure 9.8 shows the cognitive automobile “AnnieWAY” developed for this purpose by the Institute of Measurement and Control at Karlsruhe Institute of Technology [16].

The information hub used in this case is the real-time database KogMo-RTDB [17]. This database guarantees all software processes—sensor data acquisition, signal processing, environment perception, situation assessment, and behavior generation—a fast access to the needed input data,

which are all tagged with timestamps, and collects thereafter the processing results. For performance reasons, the database is memory-based.

As far as trajectory planning is concerned, a distinction between roads and unstructured zones is necessary. Moreover, to ensure a collision-free navigation, the drivable area has to be known, which requires taking into account the dynamics of potential obstacles. For this reason, the attribute *mobility* is added to all traffic-relevant entities to discern between static and dynamic ones. A higher level of detail is for example necessary in the case of an unavoidable collision to be able to make a decision such that the risk or the loss can be minimized.

5 Summary

In this contribution, two important components in the context of perception and task-specific interpretation of a dynamic environment have been presented. On the one hand, the best-suited information channels for a specific application were selected based on a Bayesian approach. On the other hand, an object-oriented environment model was proposed that constitutes an information hub, based upon which all information processing processes can suitably represent, share, and update the knowledge about the task-relevant entities and their respective attributes and relations. All knowledge is specified in terms of degree of belief, which enables to apply Bayesian fusion and inference methods to it. Additional mechanisms take care of data consistency and quality assurance, providing for a good suitability of the model for knowledge representation in intelligent autonomous systems.

References

1. "Cognition for Technical Systems," <http://www.cotesys.org/>, Retrieved February 10, 2010.
2. "Cognitive Interaction Technology," <http://www.cit-ec.de/>, Retrieved February 10, 2010.
3. M. R. Endsley, "Toward a theory of situation awareness in dynamic systems," *Human Factors: The Journal of the Human Factors and Ergonomics Society*, vol. 37, no. 1, pp. 32–64, 1995.

4. E. T. Jaynes, "Prior probabilities," *IEEE Transactions on Systems, Science, and Cybernetics*, vol. 4, no. 3, pp. 227–241, 1968.
5. J. N. Kapur, *Maximum entropy models in science and engineering*, 1st ed. New York (NY): John Wiley & Sons, 1989.
6. F. Puente León and J. Beyerer, "Datenfusion zur Gewinnung hochwertiger Bilder in der automatischen Sichtprüfung," *Automatisierungstechnik*, vol. 45, no. 10, pp. 480–489, 1997.
7. J. Beyerer, *Verfahren zur quantitativen statistischen Bewertung von Zusatzwissen in der Meßtechnik*. Düsseldorf: VDI Verlag, 1999.
8. J. Beyerer, M. Heizmann, J. Sander, and I. Gheța, *Image Fusion – Algorithms and Applications*. Academic Press, 2008, ch. Bayesian Methods for Image Fusion, pp. 157–192.
9. J. Sander, M. Heizmann, I. Goussev, and J. Beyerer, "A local approach for focussed Bayesian fusion," in *Multisensor, Multisource Information Fusion: Architectures, Algorithms, and Applications, Proceedings of SPIE Vol. 7345*, 2009.
10. R. O. Duda, P. E. Hart, and D. G. Stork, *Pattern Classification*, 2nd ed. New York: John Wiley & Sons Inc, 2001.
11. J. M. Bernardo, *Encyclopedia of Life Support Systems (EOLSS). Probability and Statistics*. Oxford: UNESCO, 2003, ch. Bayesian Statistics.
12. J. Sander and J. Beyerer, "Fusion agents – realizing Bayesian fusion via a local approach," *2006 IEEE International Conference on Multisensor Fusion and Integration for Intelligent Systems*, pp. 249–254, 2006.
13. "Humanoide Roboter," <http://www.sfb588.uni-karlsruhe.de/>, Retrieved February 10, 2010.
14. B. Kühn, A. Belkin, A. Swerdlow, T. Machmer, J. Beyerer, and K. Kroschel, "Knowledge-driven opto-acoustic scene analysis based on an object-oriented world modelling approach for humanoid robots," in *Proceedings of the 41st International Symposium on Robotics and the 6th German Conference on Robotics*. VDE-Verlag, 2010.
15. "Kognitive Automobile," <http://www.kognimobil.de/>, Retrieved February 10, 2010.
16. "Team AnnieWay," <http://annieway.mrt.uni-karlsruhe.de/>, Retrieved February 10, 2010.
17. M. Goebel, "KogMo-RTDB – Real-time database for cognitive automobiles," <http://www.kogmo-rtdb.de/>, Retrieved February 10, 2010.

Classification of partly occluded pedestrians

Vadim Frolov

Karlsruhe Institute of Technology (KIT),
Institute of Industrial Information Technology (IIIT),
Hertzstr. 16, D-76187 Karlsruhe

Abstract This paper presents a novel approach to classify partly occluded pedestrians. It focuses on the recognition of pedestrians that were fully visible for a certain amount of time and then have been occluded by lateral obstacles. Information about the environment is measured by a lidar sensor and an infrared camera. Both sensor signals are fused to determine a region of interest in the video data. The classification of these regions is based on the extraction of 2D translation invariant features, which are constructed by integrating over the transformation group. Invariant features are pre-processed in order to eliminate influence of occlusion. A support vector machine is used to classify the invariants. The proposed approach was evaluated offline and the sensors were fixed. Results demonstrate successful classification of occluded pedestrians.

1 Introduction

Among specific goals of intelligent applications such as visual surveillance, robotics, autonomous vehicles and driver assistance systems there is a common goal – detect and classify human beings. This is a challenging task not only due to the variability of human appearances and poses, but also because obstacles in urban environments make humans not fully visible. Moreover, pedestrians are often found in heavily cluttered scenes, which makes the extraction of information about the pedestrians especially difficult. Various kinds of vehicle-based sensors and techniques are used to solve this task. Commonly used sensors are passive imaging sensors using visible light and infrared (IR) radiation, as well as active “time-of-flight” sensors, such as radar and lidar scanners. Imaging sensors are widely used because of their high lateral resolution and low cost,

but extracting information from them involves substantial amount of processing. Furthermore, these sensors are very sensitive to the environment illumination and weather conditions. Time-of-flight sensors provide information about objects distances, but they deliver not enough data to perform a complex classification. These two types of sensors complement each another, and their fusion is expected to present better results than single-sensor systems [1].

This paper presents a novel approach to classify partly occluded pedestrians. The signals of an IR camera and a lidar scanner are used as the source data. Recent works to detect pedestrians using infrared cameras can be found in [1–3]. All of these works are based on the fusion of several imaging sensors data. Approaches that use time-of-flight sensors are described in [4–6]. The fusion of image and time-of-flight sensors has been studied in [7–10]. All these works are limited to the detection of fully visible pedestrians.

To recognize pedestrians, a representative set of features has to be extracted from the raw data. State-of-the-art techniques use features based on shape, motion or depth information. Some of the features used for shape-based detection are size and aspect ratio of bounding boxes [2], Haar wavelets [11], Haar-like wavelets [10], pose-specific linear (PCA) features [12], active contours [13], invariant features [14], scale-invariant DoG features [15, 16], intensity gradients [17] and their histograms [18, 19]. Global appearance changes caused by pedestrian articulations and different viewpoints are considered in [20].

Occlusions prevent correct detection and classification. The most common approach to improve classification results in case of occlusion is to use tracking. In [21] an improved mean shift tracking approach is presented. Kalman filter is used in [22] to predict pedestrians new position. The same tracking ID is reassigned to an object in case the occlusion disappears in a short time. In [23] a system for multi-person tracking in busy environments is presented. Their work uses visual odometry and several cognitive loops between internal system modules. In [24] objects appearance models are built to handle occlusions.

This work presents a new method which estimates regions where a pedestrian could appear. Normal impact of the occlusion is that a pedestrian occurred continuously in a sequence of preceding frames disappears abruptly in the current image. Information from the antecedent classifications is used to avoid this disappearance. All calculated vectors

of invariants that have to be tested with a classifier are concatenated with vector of invariants that had produced correct classification before pedestrian disappearance. If the tested image contains an object that is slightly different from the pedestrian training samples, then values of the resulting concatenated vector shift towards the pedestrian class. Since there is no information about the pedestrian's walking direction several neighbour regions are taken into account. Even if pedestrian finishes his movement while occlusion, he will be classified correctly. The proposed approach can be used to classify any desirable class. It incorporates no human body model. Additionally, the trajectory of pedestrian movements can be recorded for further use.

The rest of the paper is organized as follows. Section 2 presents the signal level data fusion and the extraction of regions of interests (ROI) in the IR images. Section 3 describes the extraction of invariant features from the ROIs and neighbour regions. Algorithm to process invariants in order to avoid possible occlusion's influence is presented in Section 4. Finally, Section 5 presents the classification results.

2 Extraction of regions of interest

2.1 Data fusion

The infrared camera perceives the environment and provides information about shape and temperature in form of an image frame sequence over time. Each frame has a size $M \times N$ pixels and is represented by:

$$g_k := g(m, n, k\Delta t), \quad (10.1)$$

where $m \in \{0, \dots, M - 1\}$, $n \in \{0, \dots, N - 1\}$ are conditioned by the camera setup parameters. The recording speed is one frame per Δt seconds. The coordinates (m, n) are understood as Cartesian coordinates in the image plane. At first IR images are fused with lidar data to define Regions Of Interest (ROIs), which are used in the classification process later on. The algorithm focuses on input image areas with a high intensity values. Such areas represent warm objects. Human body temperature is generally higher than the environment. This makes such parts of the human body like head and hands appear brighter than the background in the IR image. Other parts of the person could be isolated by clothes.

Taking this into account, all warm objects on an IR picture can be segmented by a simple threshold. This leads to reducing the information about the complete scene. Only objects with particular temperatures could potentially be part of a human body.

These extracted hot spots are labeled by an index $q \in \{1, \dots, Q\}$. The resulting Q hot spots are denoted by h_q and considered potential human heads. If there are no occlusions between pedestrians, then the resulting hot spots include all human heads in the scene. Additionally the hot spots h_q include other warm objects like car parts, traffic signals, building windows, etc.

The complete hypothetical human body must be extracted from g_k for each h_q . A generic pedestrian size of $2\text{ m} \times 1\text{ m}$ is defined in real world coordinates. To translate this real world coordinates to image coordinates the corresponding distances, measured with the lidar scanner, are used. The used lidar scanner performs a one-line scan of the scene with an angular resolution of $\Delta\varphi$ and an aperture angle of 180° . The scene is completely scanned each Δt seconds. Thus, the lidar signal can also be described as a sequence in time composed of instances:

$$d_w^k := d(w\Delta\varphi, k\Delta t), \quad (10.2)$$

where $w \in \{0, 1, \dots, W = 180^\circ/\Delta\varphi\}$. The signal d_w^k gives the distances to the objects in the scene, whose positions at the point in time $k\Delta t$ coincide with the scanning angles $w\Delta\varphi$. The correspondence between distance data and hot spots is denoted by $d_w(h_q)$. Here and further on $k\Delta t$ is equal for the infrared picture and lidar data if not stated otherwise.

For each h_q a region of $M_q \times N_q$ is defined, which can enclose the entire body. The size of this region is a function on q , i.e. a function on the distance $d_w(h_q)$. This dependency must be avoided in order to suppress scale transformations. To accomplish this, the extracted regions of pixels are scaled through interpolation to a normalized size $M' \times N'$, where M' is the region width in pixels and N' is the region height in pixels. The resulting normalized ROIs are denoted by

$$\mathcal{R}_p^k = \langle r_{m'n'}, p, k\Delta t \rangle, \quad (10.3)$$

where matrix element $r_{m'n'}$ is an intensity value from (10.1), $m' \in [0, \dots, M' - 1]$, $n' \in [0, \dots, N' - 1]$, point $p = (x, y)$ defines ROI's position relative to the frame ($x \in \{0, \dots, M - 1\}$, $y \in \{0, \dots, N - 1\}$) and is a left upper corner of the ROI.

2.2 Neighbour regions definition

A rectangle \mathcal{R}_p^k has two horizontal and two vertical neighbours whose p point coordinates are given by $(x + \Delta w, y)$, $(x - \Delta w, y)$, $(x, y + \Delta h)$, $(x, y - \Delta h)$, where $\Delta w = M' \cdot \delta$, $\Delta h = N' \cdot \delta$ and $0 < \delta \leq 1$. The constant δ defines how neighbouring regions overlap \mathcal{R}_p^k . The case when $\delta = 0$ is also considered as a neighbouring region. This set of rectangles, called 5-neighbours of \mathcal{R}_p^k , is denoted by $N_5(\mathcal{R}_p^k) = \langle N_i \mid i \in \{0, \dots, 4\} \rangle$, where N_0 is always a neighbour with $\delta = 0$. Figure 10.1 illustrates $N_3(\mathcal{R}_p^k)$.

The normalized ROIs \mathcal{R}_p^k are the patterns that must be classified. This classification is based on the invariant features extracted from each \mathcal{R}_p^k . Next section presents an approach to construct these features.

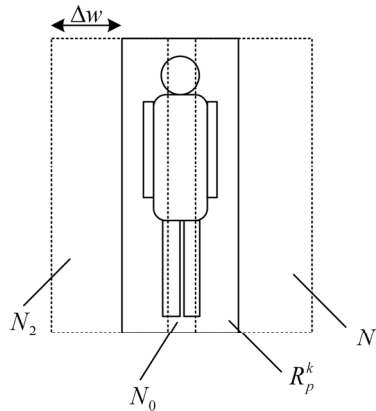


Figure 10.1: Neighbour regions example. Regions from $N_3(\mathcal{R}_p^k)$ are shown.

3 Extraction of invariants

Objects in the real world can be affected by transformations, but that should not alter their classification. These transformations in the real world induce transformations in pattern space. For a recognition task, different patterns are considered equivalent if they convey to each other through an induced transformation [25]. An induced transformation T

on a pattern \mathcal{R}_p^k is defined as a bijective map [26]:

$$\mathbb{T} : (\mathcal{R}_p^k, t) \mapsto \mathbb{T}(t)\mathcal{R}_p^k \quad \forall t \in \mathcal{T}, \quad (10.4)$$

where \mathcal{T} is the set of all transformation parameters t . The set of all transformations is denoted by $\mathbb{T}(\mathcal{T}) = \{\mathbb{T}(t) | t \in \mathcal{T}\}$. The transformation set $\mathbb{T}(\mathcal{T})$ defines an equivalence relation in pattern space, where $\mathcal{R}_p^k \equiv \mathbb{T}(t)\mathcal{R}_p^k$ for all $t \in \mathcal{T}$ [26].

A feature f^l is called invariant if, for a given transformation set $\mathbb{T}(\mathcal{T})$, it remains constant for all equivalent patterns:

$$f^l(\mathcal{R}_p^k) = f(\mathbb{T}(t)\mathcal{R}_p^k) \quad \forall t \in \mathcal{T}. \quad (10.5)$$

If the set $\mathbb{T}(\mathcal{T})$ forms a compact group, then an invariant $f^l(\mathcal{R}_p^k)$ can be constructed by integrating over this group [25–27]:

$$f^l(\mathcal{R}_p^k) = \frac{1}{|\mathbb{T}(\mathcal{T})|} \int_{\mathcal{T}} \tilde{f}^l(\mathbb{T}(t)\mathcal{R}_p^k) dt, \quad (10.6)$$

where $\tilde{f}^l(\mathbb{T}(t)\mathcal{R}_p^k) := f(\mathbb{T}(t)\mathcal{R}_p^k, \mathbf{w}_l)$ is a real function of the transformed pattern and a parameter vector \mathbf{w}_l . This function is called kernel function. The factor $|\mathbb{T}(\mathcal{T})|$ normalizes the result with respect to the group volume.

As defined in Eq. (10.3), the ROI \mathcal{R}_p^k is a discrete signal. If the transformation is discretized by defining $\mathcal{T} = \{t^0, \dots, t^{(T-1)}\}$, then the integral in Eq. (10.6) can be replaced by a summation:

$$f^l(\mathcal{R}_p^k) = \frac{1}{|\mathbb{T}(\mathcal{T})|} \sum_{\mathcal{T}} \tilde{f}^l(\mathbb{T}(t)\mathcal{R}_p^k). \quad (10.7)$$

The calculation of the transformed pattern $\mathbb{T}(t)\mathcal{R}_p^k$ for each value $t \in \mathcal{T}$ is computationally intensive. A more efficient solution is to induce the transformation $\mathbb{T}(t)$ not on the pattern but on the kernel function [25]:

$$\tilde{f}_t^l(\mathbb{T}(t)\mathcal{R}_p^k) = \mathbb{T}(t) \left\{ \tilde{f}^l(\mathcal{R}_p^k) \right\} = \tilde{f}_t^l(\mathcal{R}_p^k), \quad (10.8)$$

where \tilde{f}_t^l denotes the transformed kernel function. Eq. (10.7) can be rewritten as follows:

$$f^l(\mathcal{R}_p^k) = \frac{1}{|\mathbb{T}(\mathcal{T})|} \sum_{\mathcal{T}} \tilde{f}_t^l(\mathcal{R}_p^k). \quad (10.9)$$

3.1 Transformation group

For the detection and classification of pedestrians, the 2D translation constitutes the transformation group of interest. In this case, the transformation parameter is given by the translation vector \mathbf{t}_{ij} , where $i \in \{0, \dots, M' - 1\}$ and $j \in \{0, \dots, N' - 1\}$. The transformed normalized ROI can be defined as follows:

$$\mathbf{T}(\mathbf{t}_{ij})\mathcal{R}_p^k = \{r_{m'+i, n'+j}\}. \quad (10.10)$$

Finally, after introducing this transformation group in Eq. (10.7), the invariant feature for this group can be written as follows:

$$f(\mathcal{R}_p^k) = \frac{1}{M'N'} \sum_{i=0}^{M'-1} \sum_{j=0}^{N'-1} \tilde{f}^l(\mathbf{T}(\mathbf{t}_{ij})\mathcal{R}_p^k). \quad (10.11)$$

3.2 Kernel function

The kernel function should be constructed to extract from \mathcal{R}_p^k all relevant information for its classification. For this approach, the parameter vector of the selected kernel function is given by:

$$\mathbf{w}_l := (U_l, V_l, h(u_l, v_l)), \quad (10.12)$$

where $U_l, V_l \in \mathbb{N}$ and are interpreted as kernel size. The last element of \mathbf{w}_l is a function of the variables $u_l \in \{0, \dots, U_l - 1\}$ and $v_l \in \{0, \dots, V_l - 1\}$, where $h(u_l, v_l) \in \mathbb{N}_0$.

The selected kernel function \tilde{f}^l is a monomial defined in the following way:

$$\tilde{f}^l(\mathcal{R}_p^k) = \prod_{v_l=0}^{V_l-1} \prod_{u_l=0}^{U_l-1} [r_{u_l, v_l}]^{h(u_l, v_l)}. \quad (10.13)$$

As introduced in Eq. (10.8), the transformation $\mathbf{T}(t)$ can be induced on the kernel function. From Eq. (10.13) and considering 2D translation, the transformed kernel function can be written as follows:

$$\tilde{f}_{ij}^l(\mathcal{R}_p^k) = \prod_{u_l=0}^{U_l-1} \prod_{v_l=0}^{V_l-1} [r_{u_l+i, v_l+j}]^{h(u_l+i, v_l+j)}.$$

Rewritten Eq. (10.11) for the transformed kernel function:

$$f^l(\mathcal{R}_p^k) = \frac{1}{M'N'} \sum_{i=0}^{M'-1} \sum_{j=0}^{N'-1} \tilde{f}_{ij}^l(\mathcal{R}_p^k). \quad (10.14)$$

By defining different kernel parameters \mathbf{w}_l , a vector of invariants can be constructed for each ROI $\mathbf{f}(\mathcal{R}_p^k) = (f^1(\mathcal{R}_p^k), \dots, f^L(\mathcal{R}_p^k))$, with $L \in \mathbb{N}$.

4 Processing invariants

Two classes are defined and used in this work. They represent non-pedestrian and pedestrian objects and are denoted as $\Omega = \{0, 1\}$, where $\omega \in \Omega$. The class corresponding to a certain feature vector $\mathbf{f}(\mathcal{R}_p^k)$ is denoted by ω_p^k . The class $\omega = 0$ defines non-pedestrian objects, i.e. objects that are warm enough to be extracted from the IR video, but are not persons. The class $\omega = 1$ defines pedestrian objects.

Memory is introduced to eliminate the influence from lateral obstacles. It contains information about regions that have been classified as pedestrians. There are several assumptions introduced for the simplicity of description:

- there are two consecutive frames;
- there is only one pedestrian on both frames;
- the pedestrian is classified correctly in the first frame and misclassified in the second frame due to an obstacle.

The ROI for the correctly classified pedestrian is called “base ROI” and the following vector of invariants – “base vector”.

Given these assumptions neighbouring regions are created on the second frame and corresponding vectors of invariants are calculated. Then values of the base vector are added to the newly calculated vectors. This leads to biasing testing vectors to the pedestrian class. Results are processed with an SVM. Correctly classified region is saved as the base vector in systems memory only if it is not equal to N_0 . Algorithm 1 illustrates this method.

Use of only two frames leads to avoidance of strong influence of the correctly classified example. Such influence may result in classifying more than one neighbouring region as a pedestrian.

```

1 Start from the frame with time  $k$ ;
2  $n = 1$ ;
3 Extract ROIs. For simplicity assume, that there is only one
  pedestrian on the image with corresponding ROI  $\mathcal{R}_p^k$ ;
4  $R_{base} := \mathcal{R}_p^k$ . Variable  $R_{base}$  is used to store information about ROI
  that was correctly classified;
5 Calculate invariants vector  $\mathbf{f}_{base}(R_{base})$  according to (10.14);
6 Set  $k = k + 1$ , i.e. move to the next frame;
7 Define neighbouring regions for base ROI, calculate  $N_5(R_{base})$ ;
8 for each neighbour  $N_i$  from  $N_5$  do
9   | Calculate vector of invariants  $\mathbf{f}(N_i)$  according to (10.14);
10  | Update values of vector  $\mathbf{f}(N_i)$ ,  $f^l(N_i) = \frac{f_{base}^l(R_{base}) + f^l(N_i)}{2}$ ;
11  | Classify  $\mathbf{f}(N_i)$  and save classification result as  $\omega_i$ ;
12 end
13 Correctly classified region has index  $p$  and denoted by  $\omega_p$ ,  $\omega_p = 1$ ;
14 if  $p == 0$  then
15   | go to line 6. Do not save information if pedestrian is not moving;
16 else
17   | Save neighbour that has been classified as pedestrian, i.e.
    |  $R_{base} := N_p$ ;
18   | Save corresponding vector of invariants, i.e.  $\mathbf{f}_{base}(R_{base}) := \mathbf{f}(N_p)$ ;
19 end

```

Algorithm 1: Neighbour classification algorithm.

The algorithm could be stopped by either of two conditions: after some amount of time or by checking unbiased vector of invariants. If classification of unbiased vector of invariants results as $w_p = 1$, then algorithm should stop processing neighbouring regions until next pedestrian disappearance.

The described approach could be adopted to the real application by removing restrictions in given assumptions. For example, it is not necessary to process two consecutive frames. Two frames may be taken at time k and $k + \Delta t$ correspondingly. But in this case additional processing to find object correspondence is needed.

5 Results

In order to train and test the classifier, a database of IR images g_k and lidar measurements d_w^k has been recorded. Measurements have been done with different people and in different places to increase data variability. The set of ROIs have been automatically extracted from the database and labeled manually. Examples of the images in the database are shown in Fig. 10.2. The database contains no occluded pedestrians. All training samples consists from walking or standing pedestrians.

The algorithm has been tested on series of videos where different people cross the lateral object. Figures 10.3 and 10.4 shows classification results.



Figure 10.2: Database overview. Training set examples. Top and bottom rows show pedestrian and non-pedestrian samples, respectively.

6 Conclusion

This paper presented a new approach to classify partly occluded pedestrians. The classification is based on combining feature vectors that are known to result in correct classification with a feature vector that should

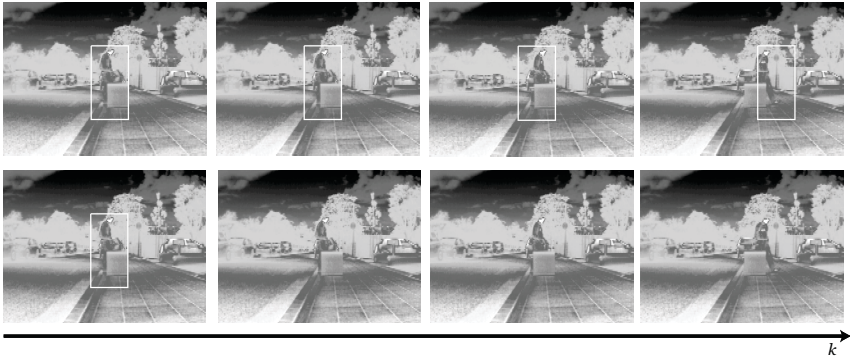


Figure 10.3: Classification results. Above sequence shows classification done with processed invariant features. Lower sequence shows classification without additional feature processing.

be tested. No tracking or movement analysis have been incorporated in the system. The classification core is extraction of invariant features. The results demonstrate the potential of the proposed method in classifying partly occluded pedestrians. Due to the fact that this method does not exploit any a priori information about the classes, it can be used to classify other traffic participants, such as cyclists or children. Computation time restrictions as well as using data from non-static, moving sensors remain an open issue.

Acknowledgment

The authors gratefully acknowledge support of this work by the Deutsche Forschungsgemeinschaft (German Research Foundation) within the Transregional Collaborative Research Centre 28 “Cognitive Automobiles.”

References

1. S. J. Krotosky and M. M. Trivedi, “On color-, infrared-, and multimodal-stereo approaches to pedestrian detection,” in *IEEE Transactions on Intel-*

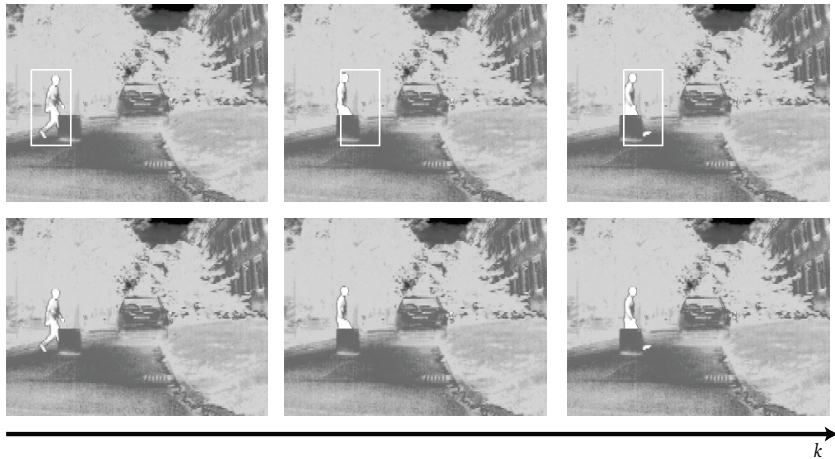


Figure 10.4: Classification results. Above sequence shows classification done with processed invariant features. Lower sequence shows classification without additional feature processing.

- ligent Transportation Systems*, vol. 8, no. 4, December 2007, pp. 619–629.
2. M. Bertozzi, A. Broggi, C. Caraffi, M. D. Rose, M. Felisa, and G. Vezzoni, “Pedestrian detection by means of far-infrared stereo vision,” *Computer Vision and Image Understanding*, vol. 106, pp. 194–204, 2007.
 3. Y. Chen and C. Han, “Night-time pedestrian detection by visual-infrared video fusion,” in *World Congress on Intelligent Control and Automation*, 2008.
 4. S. Gidel, P. Checchin, T. C. Christophe Blanc, and L. Trassoudaine, “Parzen method for fusion of laserscanner data: Application to pedestrian detection,” in *IEEE Intelligent Vehicles Symposium*, 2008.
 5. G. Gate and F. Nashashibi, “Using targets appearance to improve pedestrian classification with a laser scanner,” in *IEEE Intelligent Vehicles Symposium*, June 2008, pp. 571–576.
 6. S. Wender and K. C. J. Dietmayer, “An adaptable object classification framework,” in *IEEE Intelligent Vehicles Symposium*, 2006.
 7. M.-M. Meinecke, M. A. Obojski, M. Töns, and M. Dehesa, “Save-u: First experiences with a pre-crash system for enhancing pedestrian safety,” in

- 5th European Congress and Exhibition on Intelligent Transport Systems*, 2005.
8. B. Fardi, U. Schuenert, and G. Wanielik, "Shape and motion -based pedestrian detection in infrared images: A multi sensor approach," in *IEEE Intelligent Vehicles Symposium*, 2005, pp. 18–23.
 9. L. N. Pangop, S. Comou, F. Chausse, R. Chapuis, and S. Bonnet, "A bayesian classification of pedestrians in urban areas: The importance of the data preprocessing," in *IEEE International Conference on Multisensor Fusion and Integration for Intelligent Systems*, August 2008.
 10. C. Premebida, G. Monteiro, U. Nunes, and P. Peixoto, "A lidar and vision-based approach for pedestrian and vehicle detection and tracking," in *IEEE Intelligent Transportation Systems Conference*, 2007.
 11. P. Geismann and G. Schneider, "A two-staged approach to vision-based pedestrian recognition using haar and hog features," in *IEEE Intelligent Vehicles Symposium*, 2008.
 12. M. Enzweiler and D. M. Gavrila, "A mixed generative-discriminative framework for pedestrian classification," in *IEEE Conference on Computer Vision and Pattern Recognition*, 2008.
 13. M. Bertozzi, A. Broggi, S. Ghidoni, and M. D. Rose, "Pedestrian shape extraction by means of active contours," *Field and Service Robotics*, vol. 42, pp. 265–274, 2008.
 14. M. Thuy, A. Pérez Grassi, V. A. Frolov, and F. Puente León, "Fusion von MIR-Bildern und Lidardaten zur Klassifikation menschlicher Verkehrsteilnehmer," in *5. Workshop Fahrerassistenzsysteme*, M. Maurer and C. Stiller, Eds. Walting, Altmühltal: Freundeskreis Mess- und Regelungstechnik Karlsruhe e.V., 2-4 April 2008, pp. 168–175.
 15. D. G. Lowe, "Distinctive image features from scale-invariant keypoints," *International Journal of Computer Vision*, vol. 60, pp. 91–110, 2004.
 16. B. Leibe, E. Seemann, and B. Schiele, "Pedestrian detection in crowded scenes," in *CVPR '05: Proceedings of the 2005 IEEE Computer Society Conference on Computer Vision and Pattern Recognition (CVPR'05) - Volume 1*. Washington, DC, USA: IEEE Computer Society, 2005, pp. 878–885.
 17. F. H. C. Tivive and A. Bouzerdoun, "A biologically inspired visual pedestrian detection system," in *IEEE International Joint Conference On Neural Networks*, 2008.
 18. M. Bertozzi, A. Broggi, M. D. Rose, M. Felisa, A. Rakotomamonjy, and F. Suard, "A pedestrian detector using histograms of oriented gradients

- and a support vector machine classifier,” in *IEEE Intelligent Transportation Systems Conference*, 2007.
19. J. Dong, J. Ge, and Y. Luo, “Nighttime pedestrian detection with near infrared using cascaded classifiers,” in *IEEE International Conference on Image Processing*, 2007.
 20. E. Seemann, B. Leibe, and B. Schiele, “Multi-aspect detection of articulated objects,” in *CVPR '06: Proceedings of the 2006 IEEE Computer Society Conference on Computer Vision and Pattern Recognition*. Washington, DC, USA: IEEE Computer Society, 2006, pp. 1582–1588.
 21. Z. Li, Q. Tang, and N. Sang, “Improved mean shift algorithm for occlusion pedestrian tracking,” *Electronics Letters*, vol. 44, no. 10, pp. 622 – 623, 2008.
 22. E. Binelli, A. Broggi, A. Fascioli, S. Ghidoni, P. Grisleri, T. Graf, and M. Meinecke, “A modular tracking system for far infrared pedestrian recognition,” in *Intelligent Vehicles Symposium*. IEEE, June 2005, pp. 759–764.
 23. A. Ess, B. Leibe, K. Schindler, and L. V. Gool, “A mobile vision system for robust multi-person tracking,” in *IEEE Conference on Computer Vision and Pattern Recognition*, 2008.
 24. A. Senior, A. Hampapur, Y.-L. Tian, L. Brown, S. Pankanti, and R. Bolle, “Appearance models for occlusion handling,” *Image and Vision Computing*, vol. 24, pp. 1233–1243, 2006.
 25. H. Schulz-Mirbach, “Anwendung von invarianzprinzipien zur merkmalgewinnung in der mustererkennung,” Ph.D. dissertation, Technische Universität Hamburg-Harburg, 1995.
 26. R. Lenz, *Group Theoretical Methods in Image Processing*, Springer, Ed. Lecture Notes in Computer Science, 1990.
 27. J. Wood, “Invariant pattern recognition: a review,” *Pattern Recognition*, vol. 29, no. 1, pp. 1–17, 1996.

Cost-efficient environment perception using multiple sensors for driver assistance systems in commercial vehicles

Carola Otto,¹ Urs Wiesel,¹ Jan Wirnitzer,¹ Andreas Schwarzhaupt,¹
and Fernando Puente León²

¹ Daimler AG,
Truck Product Engineering/Advanced Engineering,
Inselstraße 140, D-70327 Stuttgart
² Karlsruhe Institute of Technology (KIT),
Institute of Industrial Information Technology (IIT),
Hertzstr. 16, D-76187 Karlsruhe

Abstract Advanced automotive safety systems require a traffic situation analysis and classification by applying the knowledge about the vehicle’s surrounding. A reaction will be carried out dependent on the knowledge and the application. Radar sensors as leading edge in vehicular remote sensing are able to precisely determine radial distances and velocities of corresponding objects/obstacles. State of the art radars cover long and short range distances by operating in multi-mode. The sensor performance is in contrast to human perception almost independent of weather and light conditions. Complementary usage of a monocular camera might enhance the perception of the environment. Its acquisition costs are significantly lower than those of a stereo camera. An advantageous overview of the road compared to a passenger car is enabled due to a higher position of the camera in the truck. Objects like passenger cars, trucks and motorcycles may be measured and classified using the rear-ends of these vehicles during day light. Back lights serve the object detection in the darkness. An algorithm for lane detection together with the fusion of radar and camera signals enables an object-to-lane allocation, which is an important contribution to the situation analysis and classification, as required in the context of adaptive cruise control or for collision avoidance by automatic steering.

1 Introduction

Each year several thousands of people die due to traffic accidents in the European Union (39,000 in 2008). The EU set the goal to reduce the number of traffic victims to 25,000 in 2010 [1]. To get at least close to this ambitious aim, it is important to invest in the development of advanced driver assistance systems that include applications for collision avoidance and pre-crash preparation and that satisfy safety-level requirements. When passenger cars crash into each other, the damage is reduced to smaller physical injuries and an economical damage in many cases. In contrast, the probability of deaths and seriously injured persons is increased dramatically in case of accidents with trucks due to the high mass of the truck. The automatic recognition of imminent collision plays an important role in making traffic more safe. The earlier a potential collision is detected, the more possibilities are available to protect car passengers and other road users. Besides driver attention and intention monitoring, it is therefore important to predict possible scenarios in advance. The vehicle environment needs to be analyzed and the situation has to be classified supporting different applications and reactions. A region of interest for relevant traffic events has to be defined to combine real-time calculations with detailed and precise information about the traffic environment in terms of object characteristics and object localization. Long-range view has to be combined with high spatial resolutions as well as a wide field of view. One approach uses a combination of radar (short and long range) and a monocular camera; see Figure 11.1.

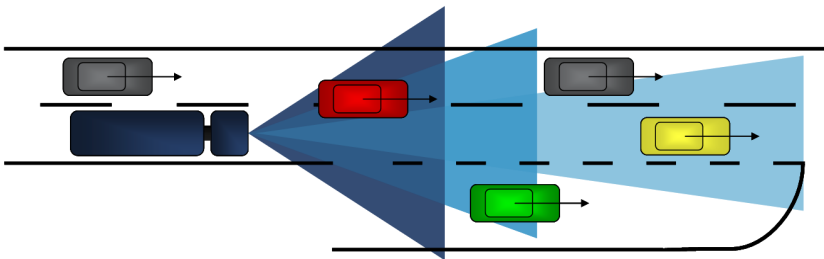


Figure 11.1: Field of view applying a short range radar (SRR), a long range radar (LRR), and a monocular camera.

The camera detects both objects and the lane markings of the road. Thereby, the road course and the traffic participants or objects of special interest for the situation analysis can be predicted. This information is particularly important on curved roads and when considering stationary objects.

2 Sensors

2.1 Radar

The radar sensor has been the state of the art for environment perception and driver assistance systems in automotive industry in the last years. Diverse weather conditions like rain or fog have almost no impact on the sensor performance, other than on human perception. Received raw data is Fourier transformed, and the peak lists are merged to targets. A measurement-to-track association is made, and a Kalman filter calculates the measurement update. The entries for the Kalman estimation process are range, bearing, and Doppler velocity [2]. The Doppler information corresponds to direct measuring of target speed and is a benefit of radar sensors. It is used to initialize the state of the tracks [3]. The radar sensor measures radial target distance and velocity very accurately. Target radius (r) and target angle (ϕ) are transformed into longitudinal and lateral distances and velocities relative to the own vehicle. While the longitudinal (x -direction) information is very accurate, the lateral resolution (y -direction) is approximate. State-of-the-art radars operate in multi-mode covering long and short range distances in one sensor. A wide area in front of the own vehicle can be monitored with sufficient aperture angles.

One challenging task remains when perceiving the environment with radar sensors: They show a small angular resolution. This makes lateral information inaccurate, especially for long distances. When radar waves are reflected from the environment, only point information is calculated. The reflection points may move on the object, so one never knows from which point of the object the reflection is received, as can be seen when a graphical fusion of data from a 3D laser scanner (Velodyne) and radar is performed. The distinction between different stationary objects (traffic signs, pedestrians) and their measuring becomes crucial.

Waves emitted by continuous wave radar sensors lead to a typical,

height-dependent interference pattern. The height-dependency may be used to distinguish relevant obstacles with lower height from higher located irrelevant objects like traffic signs [4].

If outer conditions are advantageous, road boundaries may be determined based on object lists. Imaging radar sensors provide a detailed image of the environment. Image processing algorithms may enable a road prediction based on radar information and the analysis of “free space”, even if there are only trees and bushes along the road. If noisy raw data is integrated over time, an improved signal-to-noise ratio is obtained and the robustness of following image processing steps increases. Applying edge detection shows size and positions of objects in the front more precisely. Rudimental object classification strategies may be supported by evaluating polarization differences of reflections. However, radar may benefit from vision systems and their better azimuthal resolution.

2.2 Monocular camera

A complementary vision system might be a monocular camera. Its acquisition costs are significantly lower than those of a stereo camera. An advantageous overview of the road compared to a passenger car is enabled due to a higher position of the camera in the truck. With adequate vertical and horizontal aperture angles as well as sufficient pixel/° resolution, objects may be detected and classified. Image processing techniques commonly use neural networks and pattern classification algorithms for camera object detection for daylight recordings. Considering frame sequences instead of single frames enhances the image processing output. Back and front lights of other vehicles are used for object detection during the darkness. The number of pixels that represent the object in the image frame sequences, defines the object size and distance during daylight. Assuming a flat road, the height of the back or front light representation in the image as well as the light distances from each other define the object distance and size. When the change in longitudinal and lateral object distance is evaluated, object velocities and accelerations can be determined, but the significant advantage of the camera application for object detection is the gain in lateral information quality and the object type classification. Herewith, also stationary traffic participants may be detected and classified which might be of special interest when considering rear-end collisions in traffic jams or at traffic lights.

The monocular camera provides an additional information that the radar cannot show at all. Image processing with gradient or edge detection filters supplies next information processing levels (situation analysis) with the location and course of the lane based on lane markings. Applying the a-priori knowledge that most roads follow a clothoid-shaped lane, curvatures may be determined and predicted. The visual range is longer in the truck compared to a car due to the higher position of the camera. A lane prediction based on already determined lane curvature and a polynomial of second order is used to restrict the required amount of data processing capacity and to give a higher lane confidence level. The lane information allows to narrow down the space in which relevant situations may take place. Furthermore, applications like the lane departure warning may be integrated.

Multi-purpose cameras implicate that one sensor can be used for different applications, and different illuminations are used. Beside the usage for environment perception required for active safety applications, it can be used for comfort functions such as traffic sign recognition and intelligent headlight control.

The disadvantage of the camera is its sensitiveness to pollution and bad weather conditions like rain, snow and fog. If the ego vehicle drives versus a sunset or a sunrise, the camera might be overexposed and would not be able to give any information. In this case, the system has to detect the deficit and has to account for the insufficient sensor information. This means that one has to find ways for system self-diagnosis and the handling of measurement uncertainties. One way might be the integration of additional sensors and the fusion of the sensors.

3 Fusion concept

The sensor fusion can be performed on raw data or on a higher level providing objects and boundaries. The common radar receives information about stationary and moving objects. If conditions are advantageous, the road boundary can be extracted such that e.g. road curves can be predicted and the region of interest can be restricted. The camera supplies the fusion algorithm with information about the lane markings. Thereby, one can predict whether the lane will follow a curve or go straight.

Objects can be allocated to the lane, and their position within the lane

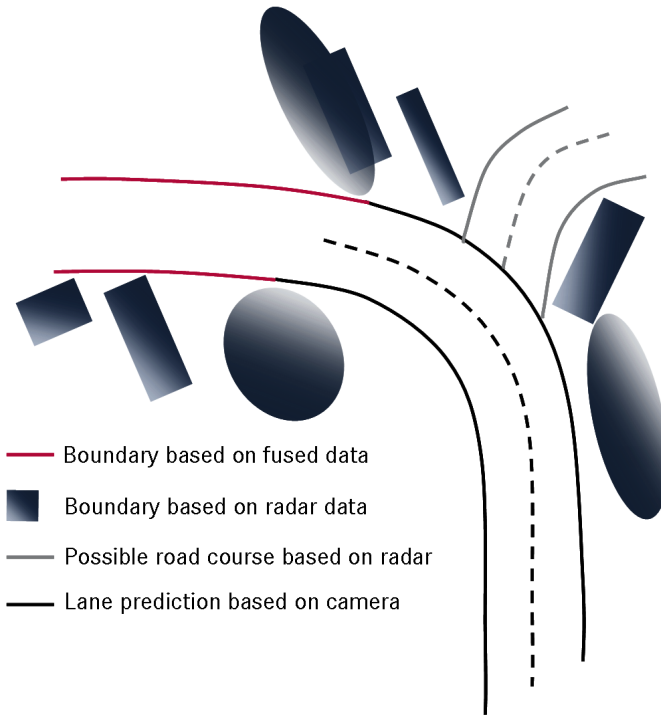


Figure 11.2: Concept for lane and road prediction.

can be given if lane and object coordinates are fused. This enables the decision if objects might become relevant for an application or a function. Oncoming traffic, e.g. in the own lane, vehicles braking, cutting in or sheering out can be identified with a certain probability.

For long distances, the lane information of the camera is not available but image radars will provide the road environment, thus showing the free space where a road might be situated. The “true” way can be predicted based on the camera lane detection (see Figure 11.2). The street takes a left turn in the figure. The radar offers the possibilities of a straight road or a road with a left turn. One obtains the information that the road has to turn left using the visual lane detection range of the camera.

Object fusion is a possibility to obtain the separation of stationary

objects, given the radar and the camera have detected the same objects. The radar detects all kinds of objects that may be relevant or not but without sufficient classification. As the camera is based on a pattern classification algorithm, it will only detect objects that look similar to those the algorithm was trained with. The camera will therefore typically detect less objects than the radar. Furthermore, the detection will not work under all weather conditions. Thus, the radar objects are used for a first level decision, especially when considering moving objects. The benefit due to the camera is the option of the object-to-lane allocation, the measured object size and lateral displacement of an detected obstacle. Thereby one may decide if e.g. a swerving maneuver is possible. Another advantage is that stationary objects may be separated from the road boundary, and traffic signs due to camera object detection and classification.

Figure 11.3 shows the general fusion concept. The course can be predicted based on road boundary detection by radar and lane prediction by camera using lane markings. Road users are detected by the radar and confirmed by the camera. If the objects are classified and allocated to a lane, decisions about their relevance can be made. In the next step, the situation analysis, ego vehicle and object trajectories can be predicted. Markov-like fusion models and Bayes networks can be used for the situation classification then, e.g. based on trajectory prediction.

One has to keep in mind that both sensors do not work perfectly. All objects detected by the sensors only exist with a certain probability. If hard threshold decisions are made on the raw data level, objects might get lost if the threshold was taken too high, and too many objects with “increased” weights would be considered if the threshold was taken too low. If the probabilities of existence are kept and multiplied with next level decision probabilities through all levels and steps of object processing, the information is given with a confidence level and applications can find decisions based on the probabilities of the object existences.

4 Discussion

The challenge of low price and high performance is known in all business areas. However, it is special in the development of driver assistance systems (DAS) for trucks compared to those of passenger cars. The

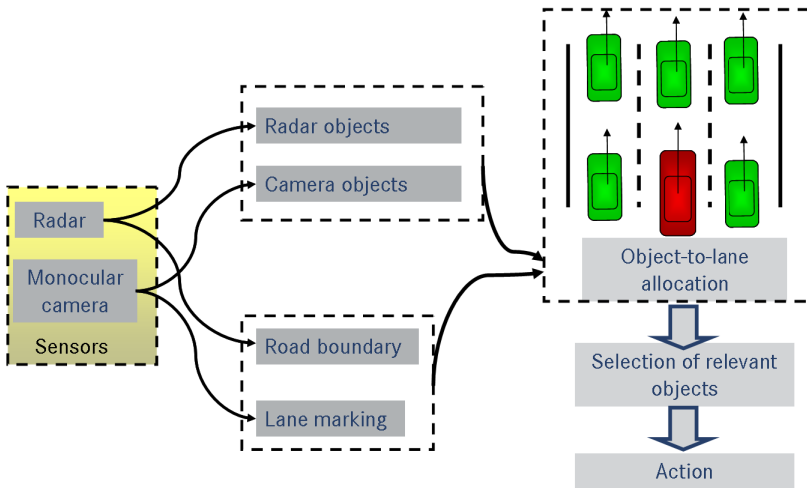


Figure 11.3: Concept for the fusion of radar and camera data.

driver is the owner of the passenger car in most cases. His own safety and comfort are important, and possessing several DASs represents a good image. Usually, the truck driver and truck owner are different persons instead. The trucks belong to the freight forwarder companies where money is the key. While the forwarder company has to pay for the DAS, the insurance company will pay in case of an accident.

3D laser scanners could be used for an almost perfect environment perception, but they are too cost intensive. The combination of sensors that are affordable and that can be used for different applications at once decreases the price per application. Therefore, the multi-purpose camera is a good compromise as it is not too expensive and can be used for other applications like intelligent headlight control, traffic sign recognition, and lane departure warning.

Sensors with a high performance often require a high amount of processing capacity to enable the real-time performance of integrated systems on board. If the requirements for control units increase significantly, they will become the expensive factor. One may hope that the increased demand of computational power due to new, additional signal processing

algorithms will be compensated by falling prices for computational power (Moore's law).

Should the required calculation power be reduced while using camera and radar for environment perception, the radar information could be used to define a region of interest for the image processing algorithm. This would enhance the spatial coverage of the camera-based object detection without increasing the demand of processor capacity. If an object is confirmed by the camera, the tracking time used by the radar for object confirmation could be shortened in some cases. Fusion at this level induces a reduced amount of transferred data on the CAN bus. On the other hand, if sensors were fused at a lower level, this would yield a high effort just when one sensor has to be replaced, e.g. due to a new software or hardware version, or when another supplier would provide a similar alternative sensor, since raw-data processing is usually accomplished by the sensor chip itself.

5 Summary and outlook

We introduced a fusion concept for environment perception of DASs that fulfills industrial requirements considering both price and performance. Based on a radar and a monocular camera, objects can be detected and they can be allocated to a lane which advances the situation analysis and its situation classification.

In this first step, the focus was set on the longitudinal traffic. Future work will consider crossing traffic as well. Monocular cameras are able to detect pedestrians, but the integration of a 2D LIDAR scanner or a stereo-camera for urban scenarios should be analyzed as well, especially when crossing traffic is considered. Fusion of GPS and map data will provide further information and can be used for situation confirmation. Moreover, the usage of data recorded in the vehicle front could be used to support blind spot applications (usage of history).

Quite often the development of new DAS applications starts on the sensor level (bottom-up). This may lead to redundant signal generation or loss of information that has to be created later with higher effort. Then, the situation analysis uses the information that is provided and builds the basis for possible applications. Top-down development (see Figure 11.4) shows the advantage of identifying which applications are

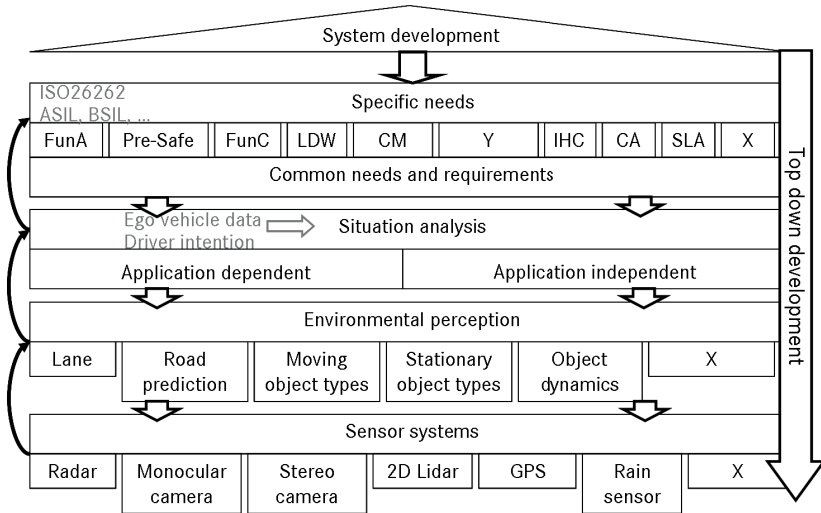


Figure 11.4: Top down system development strategy: Abbreviations denote applications like collision mitigation (CM) and Lane Departure Warning (LDW).

of special interest and which information is required for them. Synergy or cross-correlation effects between applications can be identified (e.g. front information may become information about the vehicle’s side). The decision for required sensors is done at the end. Between the single steps, feed-forward and feedback loops are integrated.

One has to remember that safety functions, especially when they actively operate a maneuver, have to fulfill high reliability and safety level requirements. All sensors show a range of uncertainties that can be identified sometimes (e.g. with additional sensors). In all cases a way has to be found to handle sensor uncertainties. One step is the introduction of a complex that handles with measurement uncertainties and system state self-diagnosis. Furthermore, a way to show the satisfaction of the safety requirements has to be defined.

Moreover, the task of lane prediction in S-curves—e.g. at road works or during a lane change—is not solved yet. It has to be evaluated when simplified clothoid models of second order are sufficient for lane predic-

tion and which other approximations can be made, e.g. polynomials of third order or splines.

References

1. European Commission, *Weniger Verkehrstote auf Europas Straßen!*, http://ec.europa.eu/news/transport/070425_1_de.htm, 2007.
2. J. Dickmann, F. Diewald, M. Maehlich, J. Klappstein, S. Zuther, S. Pietzsch, S. Hahn, and M. Munz, *Environmental perception for future integrated safety systems*, <http://www-nrd.nhtsa.dot.gov>, 2009.
3. S. Yeom, T. Kirubarajan, and Y. Bar-Shalom, "Track segment association, fine-step IMM and initialization with Doppler for improved track performance," *IEEE Transactions on Aerospace and Electronic Systems*, vol. 40, pp. 293–309, 2004.
4. R. Schneider, "Bildgebendes Radar zur Erfassung von Verkehrsszenen," *Technischer Bericht DaimlerChrysler AG*, 1998.

Highly efficient load distribution of parallel DC-DC converters

Andre Suchaneck,¹ Fernando Puente León,¹ and Andreas Jost²

¹ Karlsruhe Institute of Technology (KIT),
Institute of Industrial Information Technology (IIIT),

Hertzstr. 16, D-76187 Karlsruhe

² Daimler AG,

GR&AE Powertrain Control, Research & MBC Development,
D-70327 Untertürkheim

Abstract In modern electrical vehicles DC-DC converters are used to control the system voltage. An option to handle the power demand is to use multiple converters in parallel operation. This leads to the non-trivial problem of load distribution. In this paper, the most energy efficient method for load sharing is presented and possible control methods are proposed. To this end, the typical characteristic curves of DC-DC converters at different input and output voltages are taken into account and a setup of multiple identical converters with a common source and load is considered.

1 Introduction

In numerous applications, paralleling DC-DC converters are an option due to different reasons. Such a setup of parallel DC-DC converters offers several advantages [1–3]:

- Reduced design costs due to usage of standard converters,
- high power by using standard converters,
- higher system reliability and operational redundancy,
- modularity and scalability,
- improved thermal management,
- reduced EMI, voltage and current ripple.

Paralleling DC-DC converters requires a technique for load distribution to control the power flow through the converters in an optimal way. The criteria for optimality can be cost efficiency, packaging, weight distribution, minimization of wire/cable length, thermal stress minimization or energy efficiency. The latter is most important concerning the design of electric vehicles due to limited battery power and costs. Possible methods for different applications are proposed in [1, 2, 4, 5]. An equal load distribution among all converters to improve the life cycle of the converters is proposed in [4]. Another algorithm, presented in [1], takes into account that at low power demand some converters can be switched off to improve efficiency. In contrast to the mentioned method, in [4, 5] the load is distributed in another way. A part of the converters supply their maximum load, one converter the remaining power and the other converters are switched off. None of the techniques mentioned before takes a non-equal load distribution and the characteristic efficiency curves of converters into account.

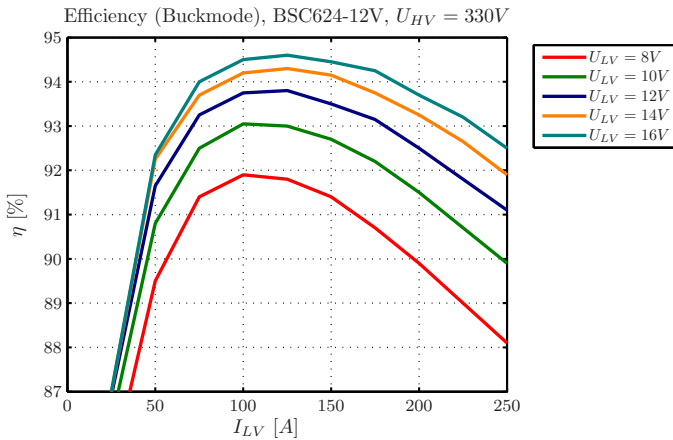


Figure 12.1: Typical efficiency characteristics of a standard DC-DC converter.

In this paper an energy optimal load distribution technique is proposed. To this end, the efficiency characteristics of a Buck-Boost converter shown in Figure 12.1, namely the Brusa BSC624, are considered. For the sake of simplicity only the Buck mode of the converter is regarded

in detail. The presented concept can easily be extended to respect the Boost mode. Throughout this paper the following setup (Figure 12.2) is considered:

- A common variable source and load is given,
- all converters have a fixed internal control algorithm,
- the converters are identical except for tolerances and
- can only be controlled by an external control unit.

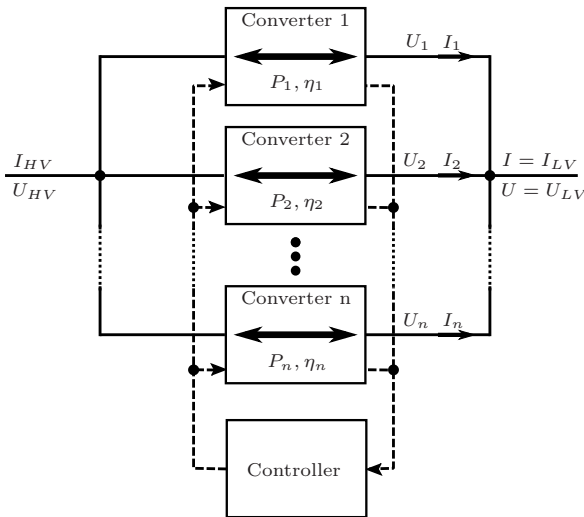


Figure 12.2: Setup with n converters with common source and load.

2 Parallel operation efficiency

The efficiency of each converter depends on the input and output voltage and the output current. To analyze energy optimality, the overall efficiency of a setup of n parallel DC-DC converters depending on the output current and the load distribution among the converters is needed.

It is given by

$$\eta = \frac{P_{\text{out}}}{P_{\text{in}}} = \frac{\sum_{i=1}^n P_{\text{out},i}}{\sum_{i=1}^n P_{\text{in},i}}, \quad (12.1)$$

where $P_{\text{in},i}$ and $P_{\text{out},i}$ are the in- and output power of each converter. In parallel setup, the output voltages U_i of all converters are the same voltage U and the sum of all output currents I_i is I :

$$U_1 = U_2 = \dots = U_n = U \quad \text{and} \quad I = \sum_{i=1}^n I_i. \quad (12.2)$$

This leads to the overall efficiency:

$$\eta = \frac{I}{\sum_{i=1}^n \frac{1}{\eta_i} \cdot I_i}. \quad (12.3)$$

3 Two converters system

The case of two converters is the most important one in automotive technology because it covers the usually needed power demands and is regarded in the following paragraph. In detail a switching strategy is presented and the influence of input and output voltages is analyzed.

3.1 Switching strategy

Assuming identical DC-DC converters with efficiency characteristics as shown in Figure 12.1, a variable load distribution between two converters defined by a quotient $\alpha = \frac{I_1}{I}$ yields to the overall efficiency given by

$$\eta = \frac{1}{\alpha \cdot \frac{1}{\eta_1} + (1 - \alpha) \cdot \frac{1}{\eta_2}}, \quad (12.4)$$

which is depicted in Figure 12.3 and differently in Figure 12.4. The dark blue colored regions A1 and A2 correspond to efficiency lower than $\eta = 0.9$. Area A1 results from the current limits of the single converters and area A2 from the small efficiency of one converter at low α factors. From Figure 12.3 and Figure 12.4 it follows that with increasing current I the highest efficiency is reached at $\alpha = 0$ upto $I = I_s$. With $I > I_s$ the

efficiency at equal distribution $\alpha = 0.5$ is the optimal choice regarding overall efficiency. The load distribution factors α between $\alpha = 0$ and $\alpha = 0.5$ are not of interest due to non energy efficiency. Therefore it can be concluded that the most efficient way of load distribution with increasing output current is using a single converter until a limit I_s is reached. Then the second converter is switched on and the control is set to equal load distribution. To avoid instabilities at currents around $I = I_s$ a hysteresis should be implemented as it is proposed in [1, 6] and shown in Figure 12.5.

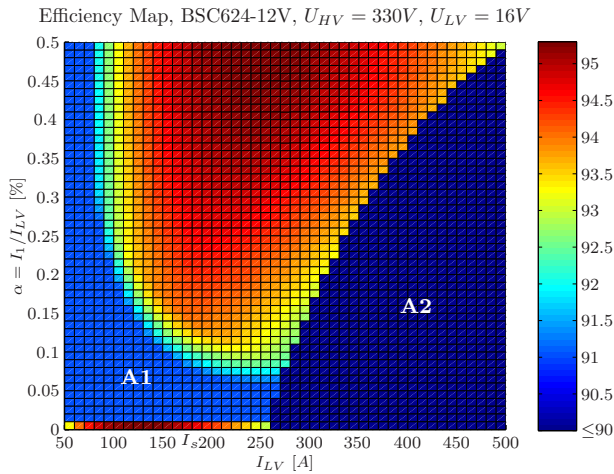


Figure 12.3: Overall efficiency map of two converters with any load distribution.

3.2 Voltage dependence

From Figure 12.1 it follows that higher voltage leads to lower losses due to lower current level [3]. Taking into account that in electric vehicles the source voltage depends on the state of charge of the battery and is therefore variable, the voltage level has to be considered. Usually the output voltage is kept constant, but to provide a general control method it is assumed also variable. Figure 12.6 shows the single converter and the equal load distribution efficiency of two identical converters at differ-

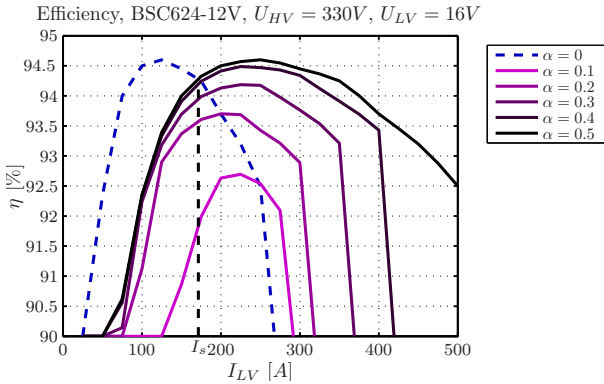


Figure 12.4: Comparison of efficiency at different load distribution factors.

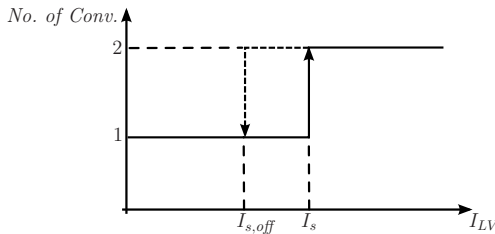


Figure 12.5: Switching hysteresis [6].

ent input and output voltages. According to Figure 12.6 the threshold current I_s at which the second converter should be switched on depends on the output voltage of the converters³.

3.3 Equal load distribution

In section 3.1 it was shown, that the most efficient way in case of $I > I_s$ is the equal load distribution. To control the converters, several methods are proposed and compared in literature [2, 4, 7]. Two methods that can be implemented by an additional control unit are:

³ The threshold current I_s also depends on the input voltage, but there are currently no measurement data for the chosen converter available to prove this.

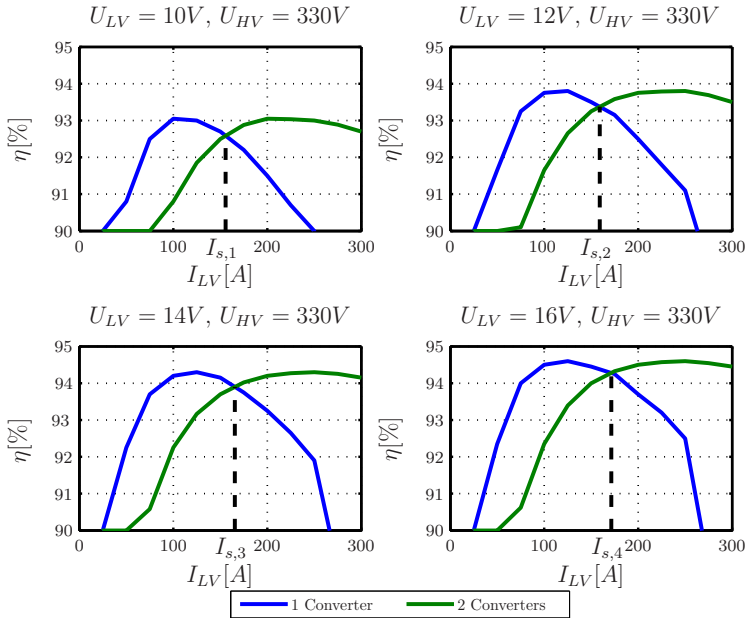


Figure 12.6: Threshold current I_s depending on output voltage.

- Master-Slave Control
- Central-Limit Control

The methods are described in detail and compared in [2, 4]. Taking into account that the internal control of each converter is fixed, the dedicated master/slave load share is a possible choice. The efficiency of the different methods is not further analyzed in this paper.

3.4 Selection of the single working converter

The usage of a single converter at currents below I_s results in higher stress of the single working converter. To share the stress over the entire life cycle, the single working converter should be alternated. In [8] the "first-on first-off" method is used to equalize the operating time. This method does not take into account that one converter might be switched

on much longer than the other. Therefore an overall stress criterion is proposed to decide which converter should be chosen next. A simple criterion is the integral over the difference between the losses $P_{l,i}$ of the converters with T meaning the overall working time:

$$c = \int_0^T (P_{l,1} - P_{l,2}) dt. \tag{12.5}$$

At the beginning and in case of $I < I_{s,off}$ the converter with the lower stress criterion value is chosen.

3.5 Complete algorithm

Summarizing the results from Sections 3.1 to 3.4, the complete algorithm for energy optimal load distribution is arranged according to Figure 12.7. Based on the input and output voltage, the threshold currents I_s and the $I_{s,off}$ are calculated first using a lookup table. In the next step, the converter states (C_1 and C_2) and the load distribution factor α are determined with the state machine shown in Figure 12.8. The load distribution among the converters is implemented in the converter control unit (CCU). To calculate the criterion c , the power losses $P_{l,i}$ of the converters are calculated within the CCU and the value is passed to the state machine block.

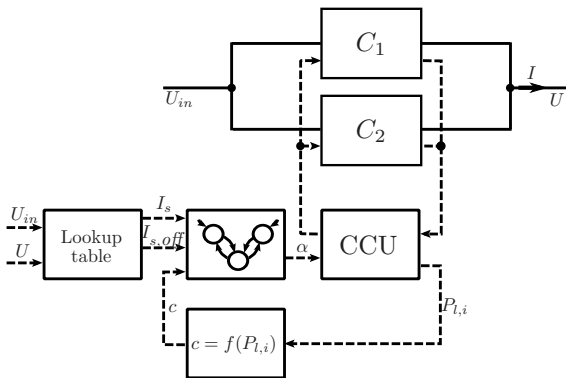


Figure 12.7: Complete algorithm.

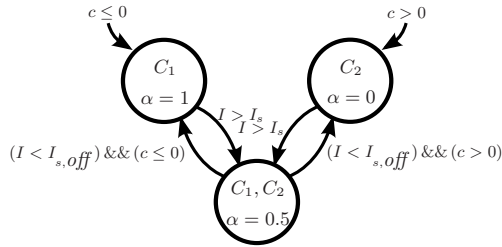


Figure 12.8: State machine for single working converter selection.

4 Conclusions and outlook

In this paper the energy optimal method for load distribution among identical DC-DC converters in parallel operation is presented. The efficiency characteristics are taken into account to get the most energy efficient algorithm. A two converters system is regarded in detail. It is shown that the most efficient way is to use a single converter up to a threshold input current and then switch on the second one with equal load distribution. The method is presented in [6, 9] without reasoning that it is the most energy efficient one. It is shown that the threshold current depends on the input and the output voltage. To share the unbalanced stress due to using a single converter at low currents, a method for choosing and alternating the single working converter is proposed taking into account the total power workload.

It is interesting to examine the extension of the results of this paper to any number of converters and the selection of the most efficient control method for equal load distribution in further work.

Acknowledgment

This work was supported by a grant from the Ministry of Science, Research and Arts of Baden-Württemberg (Az: 32-720.078-1/14).

References

1. S. Huth, "DC/DC-converters in parallel operation with digital load distribution control," *Proc. IEEE International Symposium on Industrial Electronics, ISIE '96*, vol. 2, pp. 808–813, Jun 1996.
2. L. Balogh, "Paralleling power – choosing and applying the best technique for load sharing," *Texas Instruments Incorporated*, pp. 6/1–6/30, 2003.
3. S. Luo, "A review of distributed power systems part I: DC distributed power system," *Aerospace and Electronic Systems Magazine, IEEE*, vol. 20, no. 8, pp. 5–16, Aug. 2005.
4. K. Siri and C. Lee, "Current distribution control of converters connected in parallel," in *Industry Applications Society Annual Meeting, 1990, Conference Record of the 1990 IEEE*, Oct 1990, pp. 1274–1280 vol.2.
5. Robert Bosch GmbH, "Device and method for controlled parallel operation of direct current converters," US Patent 6,314,009, 2001.
6. General Motors Corporation, "High efficiency power system with plural parallel DC/DC converters," US Patent 6,166,934, 2000.
7. S. Luo, Z. Ye, R.-L. Lin, and F. Lee, "A classification and evaluation of paralleling methods for power supply modules," in *Power Electronics Specialists Conference, 1999. PESC 99. 30th Annual IEEE*, vol. 2, 1999, pp. 901–908 vol.2.
8. C. Lee, K. Siri, and T.-F. Wu, "Dynamic current distribution controls of a parallel connected converter system," in *Power Electronics Specialists Conference, 1991. PESC '91 Record., 22nd Annual IEEE*, Jun 1991, pp. 875–881.
9. General Motors Corporation, "High efficiency power system with plural parallel DC/DC converters," US Patent 6,154,381, 2000.

Wavelet packet analysis of knock sensor signals for diagnosis of the gasoline direct injection process

Konrad Christ, Thomas Kieweler, Emre Serbetci, and Uwe Kiencke

Karlsruhe Institute of Technology (KIT),
Institute of Industrial Information Technology (IIIT),
Hertzstr. 16, D-76187 Karlsruhe

Abstract Nowadays, an important factor in the development of modern combustion engines in the automotive industry is the reduction of fuel consumption and exhaust emissions to lower travel expenses and to alleviate pollution. This report deals with the fuel injection process of a gasoline direct injection system. The accuracy of the injected fuel rate plays a key role for a proper combustion. Current control strategies for the fuel injection process are not adequate for new concepts of engine management, especially at lower injection rates, due to manufacturing dispersions of fuel injection valves. Hence, an injector calibration is needed. In this work, the possibility of using the standard knock sensor for diagnosis of the gasoline direct injection process is pointed out. The main goal is to determine if and to what extent the knock sensor signal contains information about the fuel injection process. Therefore, the knock sensor signal is analyzed in the time-frequency domain using wavelet packets.

1 Introduction

Stricter laws and provisions force the reduction of fuel consumption and exhaust emissions for modern combustion engines in the automotive industry. The improvement of efficiency is pursued by the development of gasoline direct injection (GDI) engines with common rail technology. GDI systems offer the possibility of multiple fuel injections per engine cycle over a wide range of engine speed. This results in higher engine

torques at lower fuel consumption rates compared to “old-fashioned” combustion engines with carburetors. As gasoline is sprayed directly into the cylinders, the precision of fuel metering of GDI systems is essential.

In this report, the authors investigate the possibility of a diagnosis of the GDI process via the standard knock sensors. Normally, knock sensors monitor the structure borne sound emitted by the combustion process of the engine. In all considerations of this paper, the knock sensors are used to analyze the structure borne sound emitted by the fuel injection valve during the injection process.

The fuel injection valve itself causes impacts, which excite the cylinder head. These impacts propagate through the cylinder head and the head gasket to the engine block, where the knock sensors are mounted. All measurements evaluated in this paper were taken at a four cylinder GDI engine type EA111 of Volkswagen. The fuel injection valve is presented briefly in Section 2. Unlike the considerations in [1], the measured structure borne sound signals are analyzed by the wavelet packet transform, which is introduced in Section 3. In Section 4, the results of the analysis of the knock sensor signals are presented. A conclusion will be drawn in Section 5.

2 The fuel injection valve

The considered fuel injection valve is an inward opening solenoid injector. Today, it is commonly used in modern GDI engines. The fuel injection valve mainly consists of a solenoid, which pulls up an anchor with a pintle. If the solenoid is not energized, the pintle is pressed onto the nozzle by a spring force. A more detailed description of the fuel injection valve can be found in [2].

The fuel injection valve causes impacts during the injection process. The time instants of interest are the following:

- The begin of injection (*BOI*), when the pintle starts to move up and fuel is started to be injected,
- the end of pintle lift (*EOPL*), when the anchor hits the backstop,
- the end of injection (*EOI*), when the pintle falls onto the nozzle.

In the following evaluations, the measured knock sensor signal is analyzed

within a time window of length T after the start of injection (SOI). At the SOI , the solenoid of the fuel injection valve is energized. After a certain time period, the pintle starts to move up, which corresponds to the BOI . T has to be chosen in a way, that all time instants of interest are within the time window. The following parameters mainly influence the pintle lift of the fuel injection valve:

- The injector current $I(t_i)$, which follows a given current profile and which depends on the requested injection duration t_i ,
- the fuel pressure in the common rail p_{rail} and
- the engine temperature Θ .

By applying the wavelet packet transform, the knock sensor signal shall be analyzed further in Section 4 for different requested injection durations t_i . The fuel pressure in the common rail p_{rail} and the engine temperature Θ are kept on constant values.

3 Wavelet packet analysis

Time-frequency distributions are two dimensional functions, which indicate the energy content of a time signal in the time-frequency plane. The wavelet transform is an efficient tool in time-frequency analysis. The basic idea of the wavelet transform is defining a set of orthonormal basis functions by scaling and shifting a single function called mother wavelet $\psi(t)$. This provides a good frequency resolution for low-frequency components and good time resolution for high-frequency transients of a signal. As a square integrable representation of the affine group, the scalogram can be obtained by the wavelet transform of a signal $x(t) \in L_2(\mathbb{R})$, which is defined by

$$W_x^\psi(a, b) = \int_{-\infty}^{\infty} x(t) \frac{1}{\sqrt{|a|}} \psi^*\left(\frac{t-b}{a}\right) dt.$$

$\psi(t)$ has to satisfy the admissibility condition

$$C_\Psi(a, b) = \int_{-\infty}^{\infty} \frac{|\Psi(af)|^2}{|f|} df < \infty,$$

where $\Psi(f)$ is the Fourier transform of the mother wavelet $\psi(t)$:

$$\Psi_{a,b}(f) = \sqrt{|a|} \Psi(af) e^{-j2\pi fb}.$$

In practical applications, both the signal to be analyzed and the wavelet have to be discrete in time, which means that the scaling parameter a and the shifting parameter b have to be discrete, too. It has been shown that a dyadic scale $a_k = 2^k$ and special choice of ψ constitute an orthonormal basis for $L_2(\mathbb{R})$, see [3] or [4]. Therefore, the discrete shifting parameter b_{mk} also grows dyadically:

$$b_{mk} = m 2^k T_s .$$

In this equation, T_s is the sampling period, which yields the wavelets

$$\psi_{m,k}(t) = 2^{-\frac{k}{2}} \psi(2^{-k}t - mT_s) .$$

For discrete time signals $x(t) = x(nT_s)$ of size N and wavelets $\psi(t) = \psi(nT_s)$ we obtain the discrete wavelet transform (for simplicity, we set $T_s = 1$)

$$W_x^\psi(m, k) = \sum_{n=0}^{N-1} x(n) 2^{-\frac{k}{2}} \psi^*(2^{-k}n - m) .$$

Mallat [4] recognized that the construction of different wavelet bases can be realized by the so-called multiresolution filterbanks. The fundamental principle of multiresolution analysis is the decomposition of a whole function space V_0 into individual subspaces. The approximation of a signal $x(n) \in L_2(\mathbb{R})$ in a subspace $V_k \subset V_0$ is denoted as $x_k(n)$. The space $V_0 \subset L_2(\mathbb{R})$ contains the frequency domain $\left[0, \frac{f_s}{2}\right]$, with sampling frequency f_s . The signal $x(n) \approx x_0(n) \in V_0$ is decomposed into subspaces by lowpass and bandpass filters g_{LP} and g_{BP} :

$$x_k(n) = x_{k+1}(n) + y_{k+1}(n)$$

with

$$x_{k+1}(n) = \text{Proj}_{V_{k+1}} \{x(n)\} \in V_{k+1}$$

and

$$y_{k+1}(n) = \text{Proj}_{W_{k+1}} \{x(n)\} \in W_{k+1} .$$

V_{k+1} and W_{k+1} are orthogonal subspaces of V_k : $V_{k+1} \cap W_{k+1} = \emptyset$ and $V_{k+1} \cup W_{k+1} = V_k$. The subspaces V_k are spanned by orthonormal scaling functions $\phi_{m,k}(n)$. So, the approximation of $x(n)$ in the subspace V_k is denoted as

$$x_k(n) = \sum_m c_k(m) \phi_{m,k}(n)$$

with approximation coefficients $c_k(m) = \langle x(n), \phi_{m,k}(n) \rangle$. The subspaces W_k are spanned by the orthonormal wavelet functions $\psi_{m,k}(n)$. So, the approximation of $x(n)$ in the subspace W_k is denoted as

$$y_k(n) = \sum_m d_k(m) \psi_{m,k}(n)$$

with detail coefficients $d_k(m) = \langle x(n), \psi_{m,k}(n) \rangle$. The advantage of multiresolution analysis is the efficient computation of detail and approximation coefficients in a filterbank with discrete convolutions and subsamplings. The scaling functions and wavelets are represented by a corresponding lowpass filter g_{LP} and a corresponding bandpass filter g_{BP} . Further a subsampling operator has to be introduced:

$$x_d(l) = \downarrow_2 \{x(n)\} = x(2l).$$

The approximation coefficients $c_{k+1}(l)$ are obtained by the convolution of $c_k(m)$ with the filter coefficients g_{LP} followed by a subsampling whereas the detail coefficients are computed by the convolution of $c_k(m)$ with the filter coefficients g_{BP} followed by a subsampling operation:

$$c_{k+1}(l) = \downarrow_2 \{c_k(m) * g_{LP}(m)\}$$

$$d_{k+1}(l) = \downarrow_2 \{c_k(m) * g_{BP}(m)\}.$$

In wavelet packet analysis the detail coefficients are also decomposed so that we obtain a binary tree of wavelet packets [3]. In this paper we use a complete dictionary of wavelet packets, which compose a redundant tight frame.

4 Analysis of the knock sensor signal

The fuel injection valve transmits impacts to the cylinder head during the injection process. The structure borne sound propagating through

the cylinder head and the engine block is monitored by knock sensors. The knock sensor signals $y_{t_i}(n)$ have a time varying frequency content. Hence, a time-frequency distribution is suitable for analyzing the knock sensor signals. Due to low effort in implementation and redundancy, the wavelet packet analysis is used for evaluating the signals $y_{t_i}(n)$ in the time-frequency domain. In the following, all wavelet coefficients of the binary wavelet packet tree are used to illustrate the scalogram. It shall be examined, if the time instants of interest (*BOI*, *EOPL* and *EOI*) can be localized in time and in frequency within $y_{t_i}(n)$. Therefore, $y_{t_i}(n)$ is examined for different requested injection durations t_i in Section 4.1 at constant rail pressure p_{rail} and constant engine temperature Θ . Additionally, a simple method for finding the requested injection duration $t_{i,\text{start}}$, above which the pintle is lifted, is presented in Section 4.2. In Section 4.3 a similar strategy is discussed for determining the requested injection duration $t_{i,\text{full}}$, above which the pintle hits the backstop.

The transfer function between each individual fuel injection valve and each knock sensor is engine-specific and generally unknown. The effort to determine all the transfer functions would be considerably high. Hence, the knock sensor signal is evaluated unprocessed except for a lowpass filtering with cut-off frequency f_g . GDI offers the possibility of multiple injections per engine cycle. For reasons of signal analysis, the monitored fuel injection process is performed during a period, when no disturbing influences caused by the combustion process or the engine's mechanical system occur.

4.1 Analysis of different injection durations

The injection duration is set by the injector current $I(t_i)$, which depends on the requested injection duration t_i . Figures 13.1–13.3 show the knock sensor signal and the scalogram obtained by a wavelet packet analysis with a symmlet4-wavelet in a time window of length T after the *SOI* for different t_i , whereas $t_{i,3} > t_{i,2} > t_{i,1}$. The time delay between the *SOI* and the first structure borne waves in the knock sensor signal is caused by the time of magnetization of the solenoid and the runtime of the structure borne sound.

For $t_i = t_{i,1}$ a partial pintle lift is performed, see [1]. In this case, the solenoid of the fuel injection valve is not energized long enough, so that the anchor does not hit the backstop, which means that the *EOPL* does

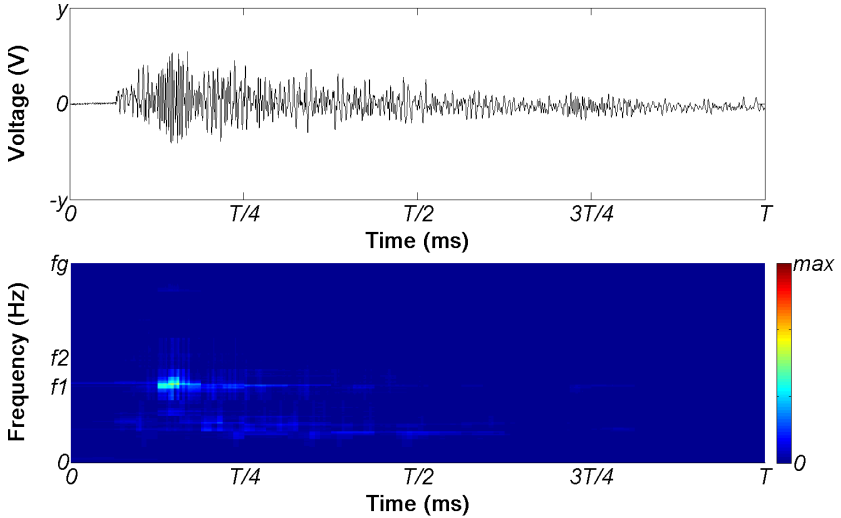


Figure 13.1: Knock sensor signal $y_{t_i}(t)$ in a time window of length T after the *SOI*: partial pintle lift for a requested injection duration of $t_i = t_{i,1}$.

not take place. High energy is located in the frequency band around $f = f_1$ to a certain moment in time, see Figure 13.1. High energy is expected at the *EOI*. Unlike the *BOI*, the *EOI* is directly related to an impact. This is the reason, why the *BOI* is not visible in the scalogram. In [1], it is shown, how the *BOI* can be detected.

For $t_i = t_{i,2}$ the fuel injection valve performs a full pintle lift. Hence, the anchor hits the backstop, which means that the *EOPL* occurs. Regarding Figure 13.2 one can clearly see that mainly two areas of high energy content are visible in the scalogram. The excited frequency bands are around $f = f_1$ and $f = f_2$. Comparing the result to the one before, the frequency band around $f = f_1$ is excited later in time. This encourages the assumption, that the *EOI* is related to frequencies around $f = f_1$. The energy content around $f = f_1$ in Figure 13.2 is higher than in Figure 13.1, because the pintle is lifted to a higher position for $t_{i,2}$ than for $t_{i,1}$. Hence, the preceding event is the *EOPL*, which excites frequencies around $f = f_2$.

Finally, a long injection duration is examined to separate the *EOPL*

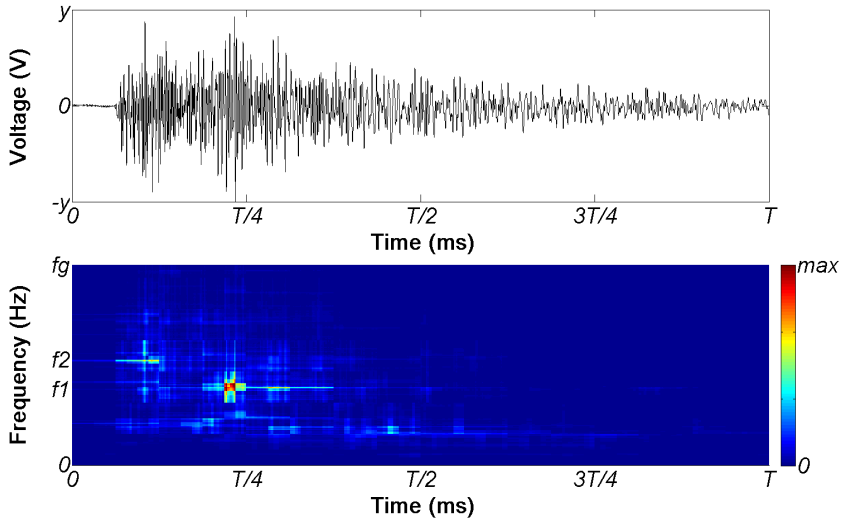


Figure 13.2: Knock sensor signal $y_{t_i}(t)$ in a time window of length T after the *SOI*: full pintle lift for a requested injection duration of $t_i = t_{i,2}$.

and the *EOI*, see Figure 13.3. It is clearly visible that *EOPL* occurs independently at the same time instant and the same frequency band around $f = f_2$ as seen before. The same holds true for the *EOI* and frequency bands around $f = f_1$ at a time instant later than before.

4.2 Detection of pintle lift

In this section, a simple method for detecting the pintle lift is presented. The goal is to find the requested injection duration $t_{i,start}$, at which the magnetic force of the solenoid is strong enough to lift the pintle. Hence, for all $t_i \geq t_{i,start}$ the pintle is lifted and fuel is injected into the cylinder. In order to decide whether an injection is proceeded or not, it is expected that the *EOI* only takes place, if and only if there has occurred a *BOI*. As can be seen in Figure 13.1, the *EOI* is related to a strong impact, which is clearly visible in the time-frequency plane. Hence, certain coefficients of the wavelet packet tree hold high energy, if an *EOI* occurs. For detection, the authors defined a region of interest in the time-frequency

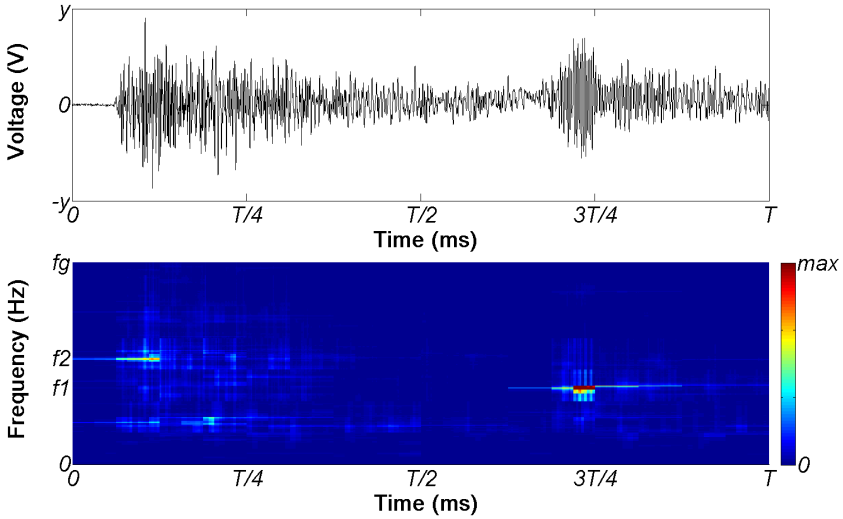
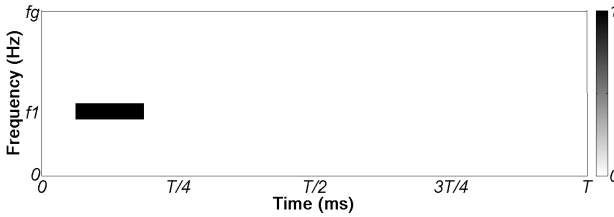


Figure 13.3: Knock sensor signal $y_{t_i}(t)$ in a time window of length T after the *SOI*: full pintle lift for a requested injection duration of $t_i = t_{i,3}$.

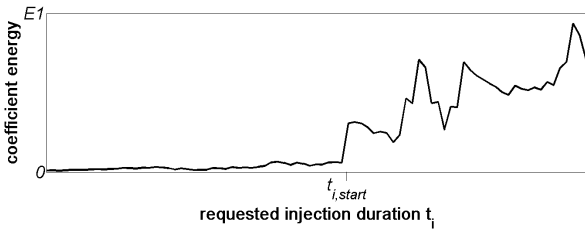
plane, where the *EOI* is expected to take place for short injection durations, see Figure 13.4(a). Adding up the energy of those wavelet packet coefficients representing this area yields to Figure 13.4(b), in which the energy content of the considered wavelet packet coefficients is plotted over the requested injection duration t_i . For $t_i = t_{i,start}$ a step in energy occurs. This is due to the pintle lift and the *EOI*, which takes place for $t_i \geq t_{i,start}$.

4.3 Detection of full pintle lift

Very similar to last section, a simple method for detecting a full pintle lift is proposed. For this, the requested injection duration $t_{i,full}$ has to be detected. For all injection durations $t_i \geq t_{i,full}$, the solenoid of the fuel injection valve is energized long enough, so that the anchor hits the backstop, which is defined as *EOPL*. As seen in Section 4.1, the *EOPL* occurs at a certain moment in time exciting frequencies around $f = f_2$. The strategy of detection is the same as presented in Section 4.2. The



(a) Region of interest in time-frequency plane where the *EOI* is expected



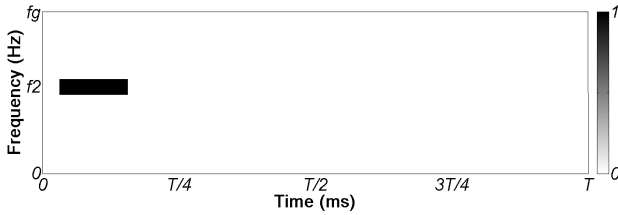
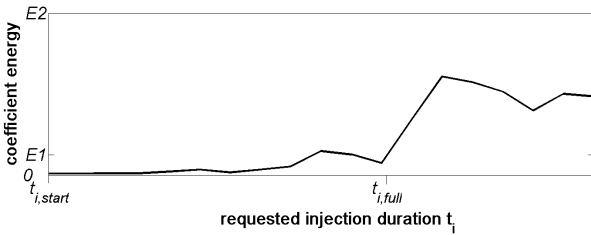
(b) Energy of coefficients within region of interest

Figure 13.4: Detection of the requested injection duration $t_{i,start}$.

wavelet coefficients, which mainly hold high energy due to the *EOPL* are shown in Figure 13.5(a). The energy content of the wavelet coefficients of interest are added up and plotted in Figure 13.5(b). The step in energy is finally assigned to $t_i = t_{i,full}$.

5 Conclusion

This report investigated the possibility using the standard knock sensor of a four cylinder gasoline direct injection engine for diagnosis of the fuel injection process. It was shown, that all time instants of interest can be identified within the structure borne sound signal monitored by the standard knock sensor during the injection process. The events of the *EOPL* and the *EOI* can be distinguished in frequency. The analysis in time-frequency domain showed adequate results for different t_i . Furthermore, the article presented two similar methods for determining the

(a) Region of interest in time-frequency plane where the *EOI* is expected

(b) Energy of coefficients within region of interest

Figure 13.5: Detection of the requested injection duration $t_{i,\text{full}}$.

requested injection durations $t_{i,\text{start}}$ and $t_{i,\text{full}}$. This information can be used for injector calibration and hence helps to improve the precision of the fuel metering of a GDI fuel injection valve.

6 Nomenclature

The following indices are used as wildcards:

t_i	Requested injection duration
y_{t_i}	Knock sensor signal during injection process
T	Length of time window
BOI	Beginning of injection
EOI	End of injection
$EOPL$	End of pintle lift
SOI	Start of injection ($I(t_i) > 0$)

References

1. K. Christ, S. Baricevic, and U. Kiencke, “Structure Borne Noise Analysis for Estimating Fuel Injection Durations,” in *2nd IFAC International Conference on Intelligent Control Systems and Signal Processing*, Istanbul (Turkey), 2009.
2. Robert Bosch GmbH, *Kraftfahrtechnisches Taschenbuch*. Vieweg, 2007.
3. U. Kiencke, M. Schwarz, and T. Weickert, *Signalverarbeitung*. Oldenbourg, 2008.
4. S. Mallat, *A Wavelet Tour of Signal Processing*, Elsevier, Ed. Academic Press, 1999.



Karlsruher Institut für Technologie



The 12th volume of Reports on Industrial Information Technology presents some selected results of research achieved at the Institute of Industrial Information Technology during the last two years.

These results have contributed to many cooperative projects with partners from academia and industry and cover current research interests including signal and image processing, pattern recognition, distributed systems, powerline communications, automotive applications, and robotics.

ISSN: 1610-9406
ISBN: 978-3-86644-490-4

